4.0 ANALYSES OF PARTICULATE SAMPLES

The samples that were analyzed under this task came from a wide variety of HGCU facilities. Many of the samples were obtained during the site visits described above, while others were shipped to SRI for analysis by other researchers involved in DOE/FETC-MGN's HGCU research program. This section presents the results of laboratory analyses of samples generated at a wide range of facilities, ranging from bench-scale units to large pilot-scale demonstration plants. Because the processes being tested were under development and optimization (as well as demonstration) when these samples were obtained, the characteristics of the samples presented in this section may not always be representative of normal, or optimized, process operation. In spite of these limitations, various discussions and comparisons are presented which promote understanding of the types of particulate materials that HGCU filters are required to collect, and how the physical and chemical characteristics of these particulate materials may affect filter performance.

4.1 LABORATORY METHODS USED TO CHARACTERIZE SAMPLES

Several techniques were repeatedly used to characterize the particulate samples from the various HGCU facilities. In addition to these methods, which are briefly described below, other techniques were occasionally applied to a limited number of samples. When necessary, these techniques are described in this report along with the associated data.

Drag-equivalent diameter - This quantity is not a measured physical diameter, but rather a fitted parameter that best expresses the fineness of the size distribution of a sample as it affects the gas-flow resistance of the sample. Smaller values of drag equivalent diameter correspond to higher gas-flow resistances at equal porosities. In general, drag-equivalent diameter decreases with decreasing physical size and with increasing specific surface area. The drag-equivalent diameter is calculated from a curve-fitting procedure performed on data obtained during measurement of the gas-flow resistance of a sample (described in this section under the heading *Specific gas-flow resistance*).

Calculations of drag-equivalent diameter values are accomplished by fitting the measured data to a permeability model of the form shown in the following two equations:

$$R = \Delta p/(UW) \quad (1)$$

$$R = 10^8 \cdot (\mu/D^2) \cdot (1/\rho) \cdot [111-211\varepsilon+100\varepsilon^2]^2 \quad (2)$$

where:
- R = specific gas-flow resistance of the porous bed, μbar·sec·cm/g
- Δp = pressure drop across the porous bed, μbar
- U = face velocity of the gas through the sample in the test cell, cm/s
- W = areal mass loading of the sample in the test cell, g/cm^2
- μ = gas viscosity, poise
- D = drag-equivalent diameter of the sample, μm
- ρ = average true density of the sample particles, g/cm^3
- ε = porosity of the sample in the test cell, dimensionless ($0 < \varepsilon < 1$).

When this equation is converted to the English units commonly used in filtration, R is expressed in units of in H_2O·min·ft/lb.

Often the actual filter cake porosity associated with a particular sample cannot be measured, although it can sometimes be estimated from other measurements. Therefore, because of the uncertainty associated with estimated values of filter cake porosity, it is often useful to compare samples according to their drag-equivalent diameters, rather than by their specific gas-flow resistances.

Specific gas-flow resistance - This value is obtained by filtering air at a known flow rate through a simulated filter cake of known porosity in a laboratory test cell while measuring the resistance to the air flow. When this measurement is made with the porosity of the simulated filter cake equal to the estimated characteristic in-situ filter cake porosity, the resistance is defined as the specific gas-flow resistance. This value is the resistance that this simulated filter cake (with an areal loading of 1.0 lb/ft^2) exhibits for an air flow of 1.0 acfm/ft^2.

The equipment used to make this measurement includes a pressure transducer, flow controller, and a cylindrical test cell with an open top and a flat, permeable bottom. A known mass of sample is loaded into the permeability cell and slightly agitated to induce a relatively uniform porosity throughout the sample bed. The top of the sample is then smoothed with a flat disc. The sample is not compacted any further at this time. After noting the height of the sample, room air is drawn through the sample at three different flowrates (highest rate first). The pressure loss through the sample (and the porous sintered metal base of the cell) is recorded for each of these flows. Air flow is discontinued and the height of the sample is once again measured to detect any compaction of the sample by the pressure that resulted from the air flow. This height is used for calculating the porosity of the sample bed during the measurement of flow resistance. The sample is then slightly compacted with a flat disc and the process is repeated. For most samples, sample permeability is measured at three or more different porosities.

These measurements yield a relationship between sample porosity and gas-flow resistance which is characteristic of the sample. (See Figure 4-1 and the discussion of *Drag-equivalent diameter* in this section.) Gas-flow resistance is simply the pressure loss across the sample bed normalized by the amount of sample in the bed (areal loading) and also by the actual flow rate of gas passing through the sample bed. Because gas-flow resistance depends strongly on the porosity of the filter bed, the relationship defined by these measurements is not sufficient to define the specific gas-flow resistance of the sample. This latter value specifies the value of gas-flow resistance that corresponds to a sample bed porosity equal to the actual porosity of a filter cake comprising the sample being evaluated.

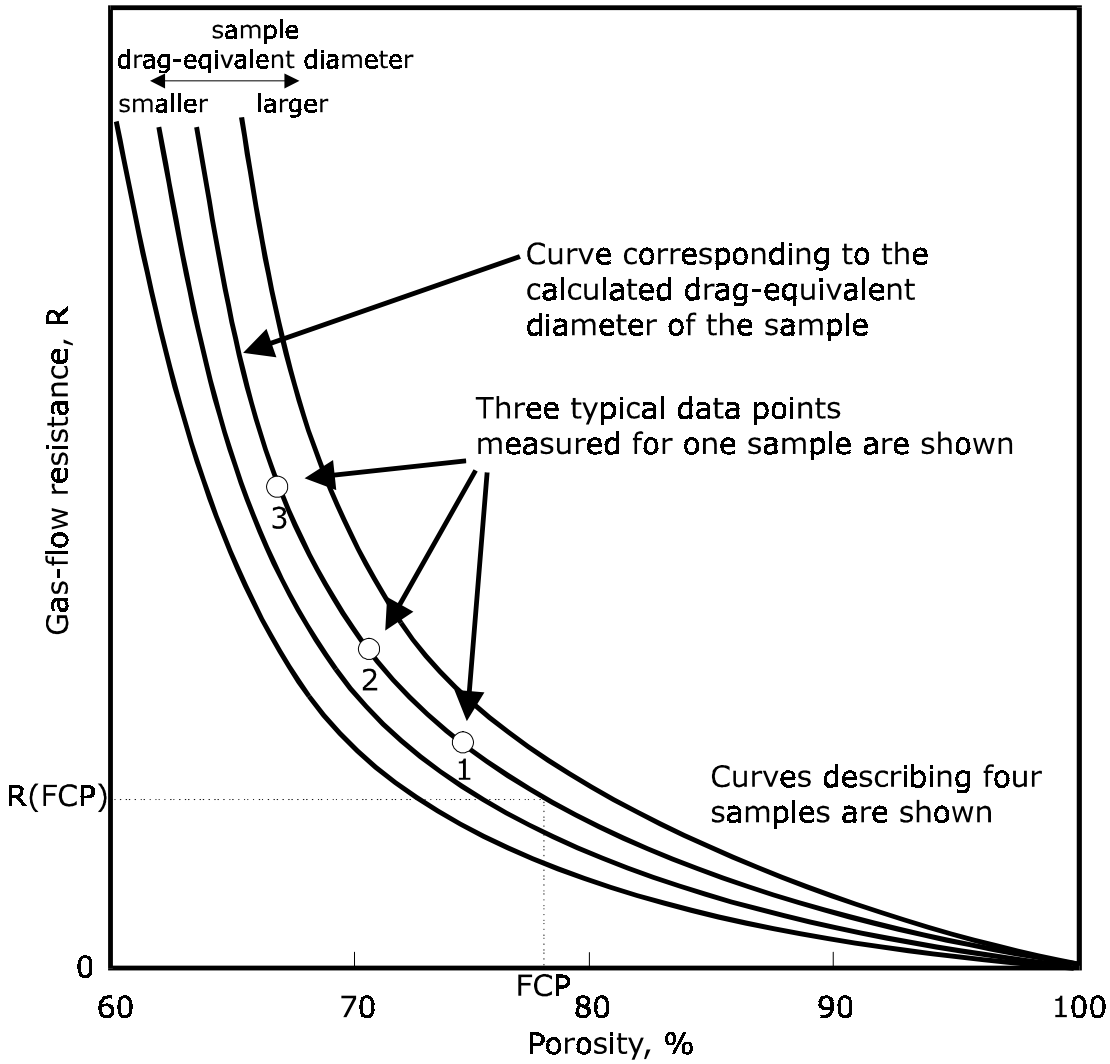

Figure 4-1. Typical curves showing the dependence of gas-flow resistance on porosity. The only difference between the curves is a scale factor ($1/D^2$), where D = the drag-equivalent diameter.

FCP = Filter Cake Porosity

Gas-flow resistance = filtering pressure drop / (face velocity • areal loading)

Uncompacted bulk porosity - This value expresses the porosity of a container of sifted sample. To determine the uncompacted bulk porosity of a sample, the sample is sifted through a 60 mesh screen (250 µm opening) into a wide, short, open-topped cylinder. The sample is sifted into the container until it is overflowing, and then the excess sample is scraped off, leaving the container completely full of sifted sample. The uncompacted bulk porosity of the sample is calculated from the weight and true density of the sample, and the internal volume of the container. Samples exhibiting a relatively high uncompacted bulk porosity value are generally highly cohesive. The uncompacted bulk porosity of a sample can be used as a direct estimate of the filter cake porosity associated with a sample, although there is evidence from field measurements that actual filter cakes may be somewhat more compact (have lower porosities) than the value returned by this test.

True density - This standard measurement is obtained with a helium pycnometer. The value obtained with this technique is the true density, or specific gravity of the sample particles in the sample tested. The true density of the sample particles is a factor in calculating the porosity of filter cakes, and the uncompacted bulk porosity, specific gas-flow resistance, and size distribution of bulk samples based on Stokes' law.

BET specific surface area - This measurement utilizes the Brunaeur-Emmett-Teller (BET) technique for determining the total surface area of a known mass of sample. Samples that exhibit relatively high specific surface areas are usually highly cohesive, and form filter cakes with relatively high porosities.

Scanning Electron Micrographs - Representative micrographs of the samples are taken at magnifications from 100 to 10,000X. The appearance of the particles often provides valuable insight into bulk sample characteristics and behavior. These micrographs also allow quick comparison of different samples and qualitative verification of particle sizing data.

Mass Median Diameter - Size distributions that return a value for mass median diameter have been measured with a variety of techniques. One technique employs a Shimadzu SA-CP4 Centrifugal Particle Size Analyzer to provide a measurement of particulate size distribution based on aerodynamic classification of the particles. The test procedure involves the suspension of a small amount of the sample in a clear fluid. The particles in the fluid gradually settle out, first due to gravitational force alone, and then due to centrifugal force introduced by increasingly rapid rotation of the sample cell. The SA-CP4 combines photometrically-obtained particle concentration data with Stokes' law describing the settling of particles in a viscous medium to calculate the particle size distribution. Another method utilizes the Leeds and Northrop X-100 Microtrac Analyzer which sizes particles suspended in a fluid based on the well-established theory of light scattering. Also, some of the HGCU samples discussed in this report have been sized with a Bahco aerodynamic classifier, which classifies particles resuspended in air according to their inertial behavior. Sieves and electroformed screens have also been used to separate particles according to their physical sizes. Generally these various methods agree well. Size distribution data can be presented as cumulative or differential distributions. The sizing data in this report are reported in terms of the physical mass median diameter (MMD) of the sample particles.

Chemical Characteristics - Standard techniques are used to determine the mineral constituents of a sample that has been ignited overnight at 750 °C. The relative proportions of these constituents (presented as oxides) are returned for Li_2O, Na_2O, K_2O, MgO, CaO, Fe_2O_3, Al_2O_3, SiO_2, TiO_2, P_2O_5, SO_3, SrO, BaO, and Mn_3O_4. Associated analyses determine the equilibrium pH and amount of soluble $SO_4^{=}$ in as-received samples. The loss on ignition (LOI) of a sample is determined gravimetrically after ignition of an as-received sample overnight at 750 °C.

Chemical analyses of ashes are often used to evaluate coals for their propensity to form fouling or slagging deposits in conventional pulverized coal-fired (PC) boilers. A variety of chemical parameters are used in these evaluations. The tables in this report presenting chemical analyses of PFBC ashes include calculated values of the silica ratio and the base-to-

acid ratio ($R_{b/a}$), that are commonly used for this purpose [12]. The definitions of these two quantities are given below:

$$\text{silica ratio} = SiO_2 \times 100 / (SiO_2 + Fe_2O_3 + CaO + MgO) \quad (3)^*$$

$$R_{b/a} = (Fe_2O_3 + CaO + MgO + K_2O + Na_2O) / (SiO_2 + Al_2O_3 + TiO_2) \quad (4)^*$$

* The silica ratio and the base-to-acid ratio are calculated from the wt %'s of the various oxides listed in equations 3 and 4.

Ashes for which the values of silica ratio fall between 50 and 65 are considered to exhibit a high probability of slagging. Values between 65 and 72 indicate some probability of slagging, and values over 72 indicate nonslagging coals. For the base-to-acid ratio defined in equation 4, a value of 0.5 is sometimes specified as the maximum tolerable value before slagging can be expected to become a problem [12].

Nodule porosity - In this test, a filter cake nodule is selected, cleaned with a gentle jet of air, and weighed. Then low-viscosity epoxy is allowed to soak slowly into the nodule until the surface of the nodule glistens evenly. The fully encapsulated nodule is baked to cure the epoxy, and its total volume is measured in a helium pycnometer. Nodule porosity is calculated from the initial dry weight, the final encapsulated volume, and the true density of the particles. Determination of the porosity of a filter cake nodule provides a direct measurement of the porosity of the filter cake. The nodule encapsulated in epoxy can be cut, machined, and prepared for further analyses, if desired. The measurement of nodule porosity can also be performed using water or alcohol to fill the pores in the nodule. When either of these fluids is used, nodule porosity is calculated from the initial dry weight, the final weight when the pores are filled with fluid, the true density of the particles, and the density of the fluid.

Tensile strength - This test measures the magnitude of the attractive forces between particles. An electrostatic tensiometer developed by Southern Research Institute is used to apply a mechanical stress on a dust layer induced by an imposed electrostatic field. This electrostatic technique allows tensile strength to be measured for uncompacted samples. A schematic diagram of the electrostatic tensiometer is shown in Figure 4-2.

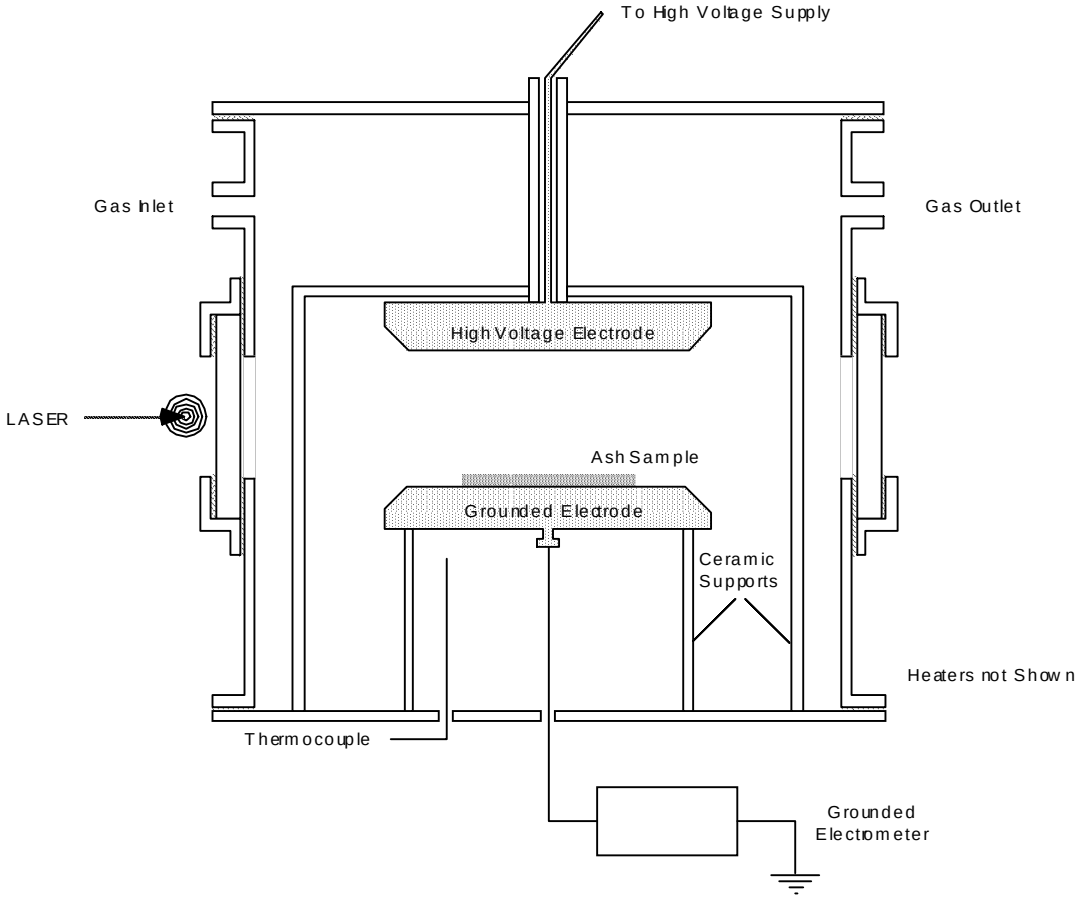

Figure 4-2. Schematic diagram of the electrostatic tensiometer.

4.2 TIDD

As discussed in section *3.0 Field Sampling and On-Site Measurements*, four visits were made to Tidd to inspect and document the condition of the APF, and to make on-site measurements and collect samples for later analysis in the laboratory. A topical report issued under this task, *Analyses of Ashes from the Tidd PFBC Advanced Particulate Filter* summarizes these on-site observations and the results of on-site and laboratory ash analyses. The laboratory analyses performed under this task are also discussed in this section. The Tidd ashes analyzed with a variety of analytical techniques and discussed in this report are identified in Table 4-1. Abbreviations used in the discussions of the sample analyses are defined in Table 4-2.

The ash samples listed in Table 4-1 include large pieces of the various types of deposits present throughout the filter vessel, as well as samples of loose ash that were found at several places in the APF. Analyses performed on ash deposits included SEM examinations of their structure and chemical composition, and direct measurements of their porosity. Measurements on loose bulk ash or deagglomerated (broken up) deposits included size distribution, chemical composition, specific surface area, uncompacted bulk porosity, and scanning electron micrographs to assess particle morphology. (Measurements of size distribution were performed on many of the samples obtained from the Tidd APF with a sedigraph. However, the relative scarcity of large particles in these samples sometimes did not allow the sedigraph to yield a reliable determination of these distributions for particles larger than about 20 to 40 µm. Therefore for some ash samples, sieve analyses were used to augment the size distribution data obtained with the sedigraph.) The results of the analyses performed on the samples from the Tidd facility are presented in Tables 4-3 through 4-8.

Table 4-1
Tidd Ash and Sorbent Samples Analyzed in the Laboratory

ID #	Date	Brief description
2791	1991	cyclone hopper
2822	1991	APF hopper
2823	1991	APF hopper
2824	1991	APF hopper
2889	1993	APF hopper
2988	1993	APF hopper
4317	1993	from ID # 2988: diameter < 45 µm
4318	1993	from ID # 2988: diameter > 45 µm
4002	7/31/93	dolomite sorbent
4003	8/5/93	dolomite sorbent
4004	8/24/93	limestone sorbent
2998	9/30/93	middle plenum ash shed
4001	9/30/93	ash from APF outlet tube
4007	9/30/93	plenum support column/conduit
4011	9/30/93	filter cake: region away from candle
4012	9/30/93	filter cake: region nearest to candle
4049	1994	APF hopper
4133	1994	APF hopper
4078	5/5/94	top plenum filter cake
4079	5/5/94	middle plenum filter cake
4084	5/5/94	top plenum ash shed
4087	5/5/94	ash deposit under middle plenum tube sheet
4088	5/5/94	ash deposit under bottom plenum tube sheet
4097	10/27/94	bottom plenum tube sheet
4103	10/27/94	filter cake from near the center of the bottom plenum
4109	10/27/94	middle plenum from inside of candle
4111	10/27/94	middle plenum filter cake
4114	10/27/94	middle plenum ash shed
4116	10/27/94	middle plenum ash bridge
4142	5/11/95	top plenum tube sheet
4143	5/11/95	top plenum filter cake
4144	5/11/95	top plenum filter cake (bottom of candles)
4320	5/11/95	from ID # 4144: diameter > 45 µm
4321	5/11/95	from ID # 4144: 15 µm < diameter < 45 µm
4151	5/11/95	middle plenum tube sheet
4322	5/11/95	from ID # 4151: diameter > 45 µm
4323	5/11/95	from ID # 4151: 15 µm < diameter < 45 µm

Table 4-2
Abbreviations for Locations from which Ash Samples were Obtained

Abbreviation	Sample location
TP	Top Plenum
MP	Middle Plenum
BP	Bottom Plenum
TS	Underside of Tube sheet
AB	Ash Bridge between Candles
AS	Ash Shedding Cone
PSC	Plenum Support Column/Conduit
FC	Filter Cake Ash from Candle Surface
IC	Inside of Candle Filter Element
OT	APF Outlet Tube
CH	Cyclone Hopper
AH	APF Hopper

Table 4-3
Chemical Analyses of Selected Tidd Ashes and Sorbents, % wt.

location/description	AH all diam	AH all diam	AH d < 45 µm	AH d > 45 µm	dolomite sorbent	dolomite sorbent	limestone sorbent
constituent ID #	2889	2988	4317	4318	4002	4003	4004
Na_2O	0.30	0.31	0.28	0.40	0.67	0.39	0.79
K_2O	1.6	1.42	1.51	1.16	0.11	0.07	0.12
MgO	9.9	9.63	9.56	9.86	40.34	41.16	10.00
CaO	15.3	15.48	15.21	16.32	53.58	53.69	78.33
Fe_2O_3	5.3	6.49	4.09	13.86	1.00	0.92	1.61
Al_2O_3	13.4	11.80	11.17	13.75	1.08	1.00	1.46
SiO_2	19.2	21.29	19.32	27.32	2.24	2.04	5.27
TiO_2	0.50	0.56	0.54	0.61	0.05	0.23	0.06
P_2O_5	0.08	0.12	0.11	0.17	0.17	0.15	0.32
SO_3	33.6	31.10	36.01	16.07	0.28	0.24	0.75
LOI	1.5	2.96	1.68	6.90	0.32	0.25	0.20
soluble $SO_4^{=}$	48.3	--	--	--	--	--	--
Equilibrium pH*	8.2	--	--	--	--	--	--
silica ratio*	39	40	40	41	2.3	2.1	5.5
$R_{b/a}$*	0.99	0.99	0.99	1.00	28.4	29.4	13.4

* dimensionless

Table 4-4
Chemical Analyses of Additional Tidd Ashes, % wt.

location	AS	PSC	FC	FC	FC	TS	FC
constituent ID #	2998	4007	4011	4012	4078	4087	4144
Li_2O	--	--	--	--	0.01	0.01	0.01
Na_2O	0.28	0.27	0.30	0.27	0.35	0.34	0.29
K_2O	1.38	1.48	1.73	1.77	1.40	1.6	1.3
MgO	9.71	9.26	8.77	7.96	9.60	8.7	8.3
CaO	15.42	14.69	14.16	13.67	14.3	13.2	14.1
Fe_2O_3	3.89	4.02	4.79	5.63	5.70	5.3	7.1
Al_2O_3	9.92	11.32	13.01	13.63	11.5	12.2	11.7
SiO_2	16.68	19.25	23.03	22.89	22.9	24.3	26.1
TiO_2	0.48	0.55	0.61	0.07	0.50	0.5	1.2
P_2O_5	0.09	0.13	0.11	0.10	0.10	0.08	0.15
SO_3	39.05	36.94	31.06	31.38	31.2	32	30.1
LOI	1.17	3.44	1.45	1.84	7.8	5.1	13.5
soluble $SO_4^=$	--	--	--	40.2	37.3	39.1	29.7
Equilibrium pH*	--	--	--	--	9.1	5.8	--
silica ratio*	36	41	45	46	44	47	47
$R_{b/a}$*	1.13	0.96	0.81	0.80	0.90	0.79	0.80

* dimensionless

Table 4-5
Physical Characteristics of Selected Tidd Ash Samples

ID #	2791	2822	2823	2824	2889	2988	2998	4001	4007
quantity location	CH	AH	AH	AH	AH	AH	AS	OT	PSC
uncompacted bulk porosity, %	93	91	89	87	92	--	--	--	92
mass median diameter, µm	1.3	2.6	2.2	2.5	3.8	4.3	5.9	5.8	4.1
specific surface area, m^2/g	4.8	4.0	3.4	3.1	3.0	--	--	--	--
true density, g/cm^3	2.78	2.85	3.01	3.04	2.90	--	--	--	2.87
drag-equivalent diameter, µm	0.654	1.694	1.146	1.744	0.852	--	--	--	--
specific gas flow resistance, in H_2O·min·ft/lb*	2.28	0.68	2.58	1.84	1.89	--	--	--	--
morphology factor	4.7	7.9	7.1	8.7	--	--	--	--	--

* calculated for an assumed filter cake porosity equal to the uncompacted bulk porosity

Table 4-6
Physical Characteristics of Selected Tidd Ash Samples

ID #	4011	4012	4049	4133	4078	4079	4084	4087
quantity location	FC	FC	AH	AH	FC	FC	AS	TS
uncompacted bulk porosity, %	92	94	88	--	88	--	91	91
mass median diameter, µm	3.8	3.0	--	7.2	4.7	2.4	3.8	4.9
true density, g/cm^3	2.83	2.82	2.90	2.90	2.72	--	--	2.72
drag-equivalent diameter, µm	1.352	1.435	1.455	--	1.513	--	--	--
specific gas flow resistance, in H_2O·min·ft/lb*	0.77	0.30	2.17	--	2.14	--	--	--

* calculated for an assumed filter cake porosity equal to the uncompacted bulk porosity

Table 4-7
Physical Characteristics of Selected Tidd Ash Samples

ID #	4097	4103	4109	4111	4114	4142
quantity location	TS	FC	IC	FC	PSC	TS
uncompacted bulk porosity, %	91	--	--	--	92	80
mass median diameter, µm	7.0	2.9	4.5	3.6	3.9	17

Table 4-8
Physical Characteristics of Selected Tidd Ash Samples

ID #	4144	4320	4321	4151	4322	4323
location	FC	FC	FC	TS	TS	TS
quantity description	all d	d > 45	15<d<45	all d	d > 45	15<d<45
uncompacted bulk porosity, %	84	--	--	81	--	--
mass median diameter, µm	11	--	--	16	--	--
specific surface area, m^2/g	--	6.9	5.1	--	1.7	1.8
true density, g/cm^3	--	--	--	2.98	--	--

One of the goals of these analyses was to assess the effect that spoiling, and eventually bypassing, the cyclone upstream of the Tidd APF had on the characteristics of the ash reaching the APF. Another goal of these analyses was to identify the mechanism(s) controlling the formation of high-strength ash deposits in the APF.

The extent to which spoiling and bypassing the cyclone upstream of the APF promoted the inclusion of relatively large particles in the ash deposits in the filter vessel can be assessed by examining the size distribution data measured with a sedigraph for various ash samples taken from the APF during the four site visits made to the facility. The mass median diameters of ashes obtained on or before September 30, 1993 ranged from 2.2 to 5.9 µm. The mass median diameters increased slightly for samples collected in 1994, when the cyclone was spoiled (values ranged from 2.4 to 7.2 µm). The major changes in the size distributions of the ashes collected in the APF did not occur until the last period of operation, during which the cyclone was completely bypassed. In this period, the mass median diameter values measured ranged from 11 to 17 µm.

Even more enlightening descriptions of the effect of cyclone operation on size distributions were obtained by combining sieve and sedigraphic analyses. To characterize the coarser portion of selected Tidd ashes, sieve analyses were performed on samples collected in October 1994, after spoiled cyclone operation, and May 1995, after operation with the cyclone completely bypassed. The sieving process used separated a portion of the original ashes into three size fractions: particle diameters > 45 µm; particle diameters > 15 µm, but smaller than 45 µm; and ash particles with diameters < 15 µm. (The sieving process caused this last, smallest fraction to be discarded along with the isopropanol used to wash the particles through the 45 µm and 15 µm sieves.) The data in Table 4-9 show that bypassing the cyclone between October 1994 and May 1995 significantly increased the size distributions of ash collected in the APF. In Figure 4-3, the size distribution data for the five samples characterized with sieve analyses have been combined with size distribution data obtained with a sedigraph. These combined data clearly show the increase in particle size induced by bypassing the cyclone.

Table 4-9
Sieve Analyses of Tidd Ashes

	% weight		
ID #, (location), date size range	diam > 45 µm	45 µm > diam > 15 µm	diam < 15µm
4097, (BP, TS), October 1994	4.03	17.3	78.6
4114, (MP, AS), October 1994	0.64	3.84	95.5
4142, (TP, TS), May 1995	28.9	50.7	20.4
4144, (TP, FC), May 1995	30.1	34.3	35.6
4151, (MP, TS), May 1995	44.8	33.3	21.9

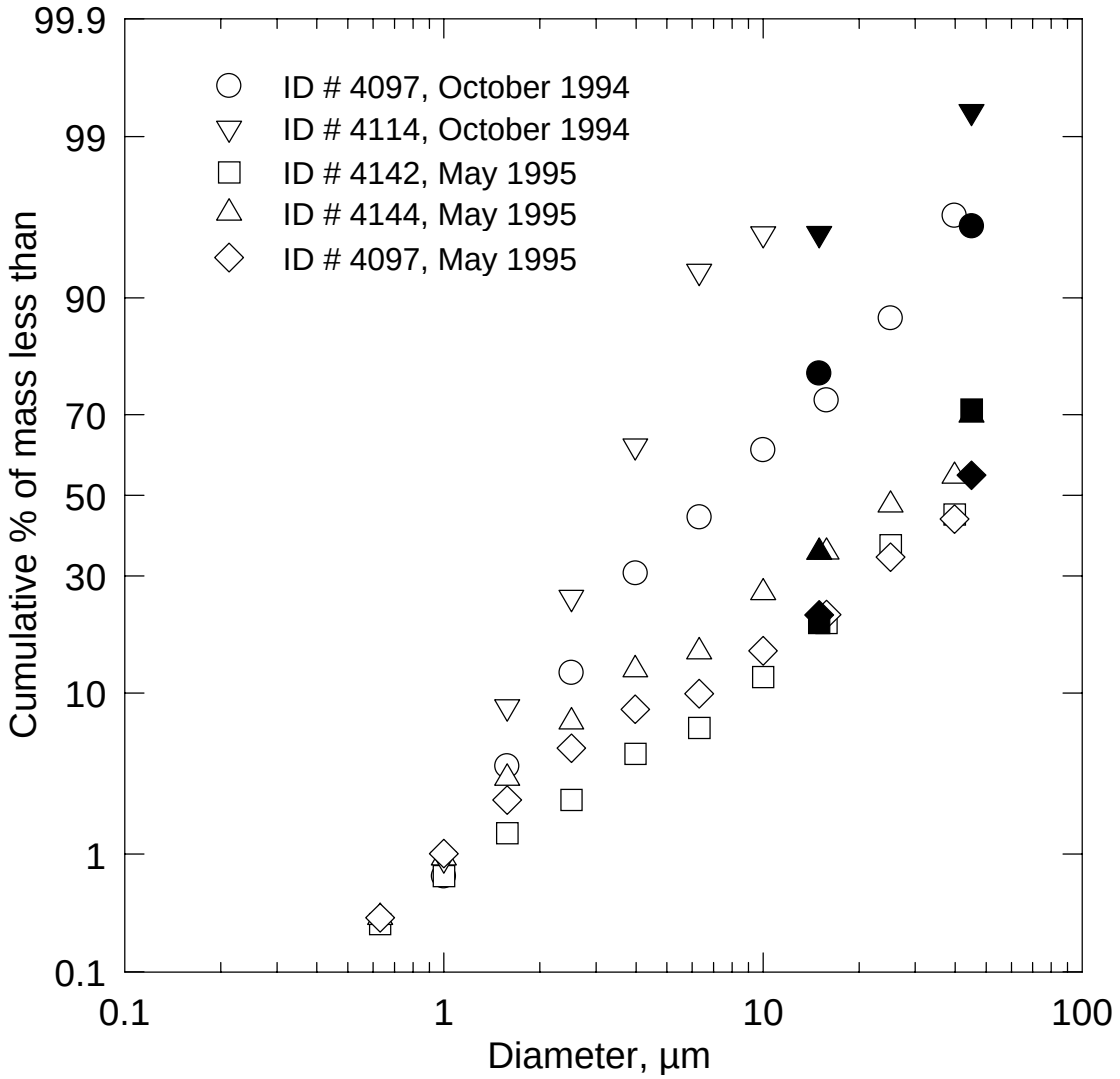

Figure 4-3. Cumulative size distribution data measured with a sedigraph and sieves for five ashes collected from the Tidd APF. The hollow data points represent sedigraphically obtained diameters. The filled data points represent data obtained in the sieve analyses.

Another purpose of performing the sieve analyses detailed in Table 4-9 was to compare the population of large particles in the ash deposits found on the top of the ash shedding cone under the middle plenum with the deposit that formed under the tube sheet at the top of the bottom plenum. These two sample locations are physically close to one another. Measurements were performed to determine if gravitational settling is the primary mechanism responsible for the presence of large particles in the ash deposits found at various locations in the filter vessel. If this were the case, the sample taken from the ash shedding cone should have a significantly greater proportion of large particles than the sample from under the tube sheet. The sieve data measured for ID # 4097 (BP, TS) and ID # 4114 (MP, AS) included in Table 4-9 do not confirm this hypothesis. Because there is no active mechanism such as gas flow through the filter cake to carry particles to the region under the tube sheet, the whole size range of particles found in the deposits from this location must have been transported to the deposit by eddy diffusion and/or Brownian movement. In fact,

the sieve data for these two samples show that particles comprising the ash deposit formed on the ash shedding cone are significantly finer than those from the deposit underneath the tube sheet. The reason for this difference is not known.

The ash sample collected from the tube sheet in the middle plenum on May 11, 1995 (ID # 4151, MP, TS) behaved much more like a free-flowing powder than the other samples collected on this site visit. Based on the sieve measurements, this free-flowing ash exhibited the largest particle size distribution of those ashes that were analyzed. When this ash was removed from the tube sheet, it was loose and fluffy, unlike the other ash samples that were consolidated into nodules and deposits. This type of difference is common with fine powders, and is almost certainly a factor in the relative cleanliness of the filter vessel when it was opened in May 1995. Powders normally become more free flowing as their particle size distribution becomes coarser. The relative coarseness of ID # 4151 (MP, TS), as indicated by the sieve analyses discussed earlier, is also evident in the values of specific surface area data measured for samples 4320 (TP, FC) and 4322 (MP, TS).

Chemical analyses of the free-flowing ash (ID # 4151, MP, TS) described above, and one of the nodular filter cake ashes (ID # 4144, TP, FC) were performed to determine if differences other than particle size might account for the tendency of the coarser ash to behave like a free-flowing powder. Chemical analyses of these two ashes and the size-separated portions generated from them during sieving (ID #'s 4320, 4321, 4322, and 4323) are summarized in Table 4-10.

Table 4-10
Chemical Analyses of Selected Tidd Ashes Collected in May, 1995, % wt.

description / size range	nodular ash (TP, FC)			free-flowing ash (MP, TS)		
	all diameters	d > 45 µm	15 µm < d, d < 45 µm	all diameters	d > 45 µm	15 µm < d, d < 45 µm
constituent ID #	4144	4320	4321	4151	4322	4323
Li_2O	0.01	0.01	0.01	0.01	0.01	0.01
Na_2O	0.29	0.16	0.23	0.27	0.13	0.20
K_2O	1.3	0.83	1.3	1.2	0.77	1.1
MgO	8.3	11.3	8.5	13.2	16.5	13.5
CaO	14.1	18.1	15.0	20.5	24.7	21.0
Fe_2O_3	7.1	4.8	7.5	8.0	6.2	9.9
Al_2O_3	11.7	7.5	10.8	10.8	7.2	9.5
SiO_2	26.1	17.6	26.0	25.1	19.6	25.6
TiO_2	1.2	0.41	0.46	1.1	0.33	0.49
P_2O_5	0.15	0.12	0.14	0.14	0.10	0.14
SO_3	30.1	38.5	28.5	19.5	22.9	17.4
LOI	13.5	19.6	15.3	1.5	2.4	1.1
soluble $SO_4^=$	29.7	36.0	29.8	22.4	26.3	20.6
silica ratio*	47	34	46	38	29	37
$R_{b/a}$*	0.80	1.38	0.87	1.17	1.78	1.28

* dimensionless

Like other Tidd ashes that were analyzed, the primary elemental constituents of these samples were calcium, magnesium, aluminum, silicon and sulfur. These analyses demonstrated that the larger ash particles in both samples (ID # 4144, TP, FC and ID # 4151, MP, TS) contain more Mg, Ca, SO_3, and have higher LOI values than the smaller particles. The smaller particles are richer in Al, Na, K, Fe, Ti, and Si. These results suggest that the larger ash particles were derived mainly from the sorbent used in the combustion process, while the smaller particles were derived mainly from the coal. This conclusion is supported by comparisons of the concentrations of calcium and magnesium in the two parent samples and their corresponding size fractions. The coarser tube sheet ash (ID # 4151, MP, TS) contains about 50 % more calcium and magnesium than the finer filter cake ash. The particles too large to pass through the 45 µm sieve also had a different appearance than the finer particles. Whereas the finer particles all had the characteristic reddish-orange color associated with PFBC ashes, most of the larger particles were brown. A few of them were black or white. All of these differences suggest that the sorbent-derived ash particles were somewhat larger than the coal-derived ash particles in these samples.

Another interesting difference in ID # 4144 (TP,FC) and ID # 4151 (MP, TS) is evident in the relative amounts of sulfur, and calcium and magnesium found in these samples. The filter cake ash (ID # 4144) contains more sulfur, and less sorbent (calcium and magnesium) than the ash collected from underneath the tube sheet (ID # 4151). The differences in these ratios is most likely a result of the exposure of the filter cake ash to much more flue gas than the ash obtained from the passive deposit under the tube sheet. As flue gas is filtered through the filter cake, additional SO_2 in the flue gas is captured by unreacted calcium and/or magnesium still remaining in the ash. Although unreacted sorbent present in the passive ash deposits can still react with SO_2 in the flue gas, the reaction is diminished because the flue gas in direct contact with the ash particles in a passive deposit is exchanged or refreshed relatively slowly. The comparisons discussed above suggest that it is possible that the apparent lower cohesivity of the tube sheet ash (ID # 4151, MP, TS) may be partially a result of chemical differences as well as differences in size distribution.

In order to assess the effects that residence time in the APF might have on ash chemistry, the chemistry of two ash samples that had been obtained from a well-consolidated one inch-thick filter cake that had resided in the APF for an extended period (ID #s 4011 and 4012) were compared with two APF hopper ashes (ID #s 2889 and 2988) from the same period of operation. (Hopper ash provides the best sample available from Tidd that had minimal exposure to the conditions in the APF.) The mineral analyses of these four samples are presented in Tables 4-3 and 4-4. These comparisons were made in order to help determine the mechanism responsible for the consolidation of the ash deposits formed in the APF. The significance of the relative amounts of sulfur measured in these two types of samples is discussed in the section entitled *5.8 Consolidation and Bridging of Ash Deposits in PFBC Filters* later in this report.

The silica ratio and $R_{b/a}$ values presented for the Tidd ashes in Tables 4-3, 4-4, and 4-10 indicate that these ashes could be interpreted as having a very high probability of slagging if present in a pulverized coal (PC) boiler.[12] (These quantities are defined in section *4.1 Laboratory Methods used to Characterize Samples*.) Although these two indicators were

developed based on experiences at PC boilers, the degree to which these quantities calculated for the Tidd ashes surpass the criteria for a high probability for slagging (silica ratio < 65; $R_{b/a}$ > 0.5) may indicate that these quantities are useful tools for predicting the probability for the development of high-strength PFBC ash deposits in HGCU filters.

Because the most freshly deposited portions of the filter cakes and passively deposited ash collected during the site visits to Tidd were too fragile to survive the journey back to the Southern Research laboratory intact, a number of these samples were encapsulated in low-viscosity epoxy at the Tidd plant. This procedure allowed more detailed measurements of the porosity of these deposits as well as preservation of the samples for further analyses. The porosity of several ash nodules from various locations in the APF collected during the site visits are given in Table 4-11. These data show that the porosity of nodules formed in the APF was lower for samples obtained after the cyclone had been completely bypassed. This trend can also be seen in the uncompacted bulk porosity data in Tables 4-7 and 4-8. Coupled with the apparent increase in the size distribution of ashes after the bypassing of the cyclone noted above, these results support the contention that the cohesivity of the ash collected in the APF was significantly reduced by the inclusion of a greater proportion of relatively large particles.

Table 4-11
Porosity of Tidd Ash Nodules

ID #, (location)	date	porosity, %
4097, (BP, TS)	October 27, 1994	84.4
4114, (MP, AS)	October 27, 1994	84.0
4116, (MP, AB)	October 27, 1994	82.3
4142, (TP, TS)	May 11, 1995	73.2
4144, (TP, FC)	May 11, 1995	69.5

The ash nodules obtained from the APF had comparatively high strength. Laboratory data showed that the mechanically-measured tensile strength of a fully-consolidated Tidd filter cake nodule could exceed 12.5 psi. When Tidd ash nodules were slowly covered with water, they rapidly disintegrated. When this same procedure was performed with ethanol or isopropanol, the nodules maintained their shape, and when they dried, they seemed to recover all of their initial strength. Apparently the hydration of various compound(s) in the ash or the dissolution of water soluble compounds into the water broke apart the interparticle bonds in the nodules.

As with other HGCU samples that were studied, examination of ash nodules and loose bulk ash samples with a scanning electron microscope (SEM) proved very useful. SEM examinations of six of the samples obtained in May 1995 supported the sieve and specific surface area data that correlated ash coarseness with the free-flowing behavior noted for sample ID # 4151 (MP, TS). These SEM micrographs, which present representative views of sample # 4151, # 4144, and the size fractions sieved from these two samples (ID #s 4320 through 4323) are presented in Figures 4-4 through 4-9.

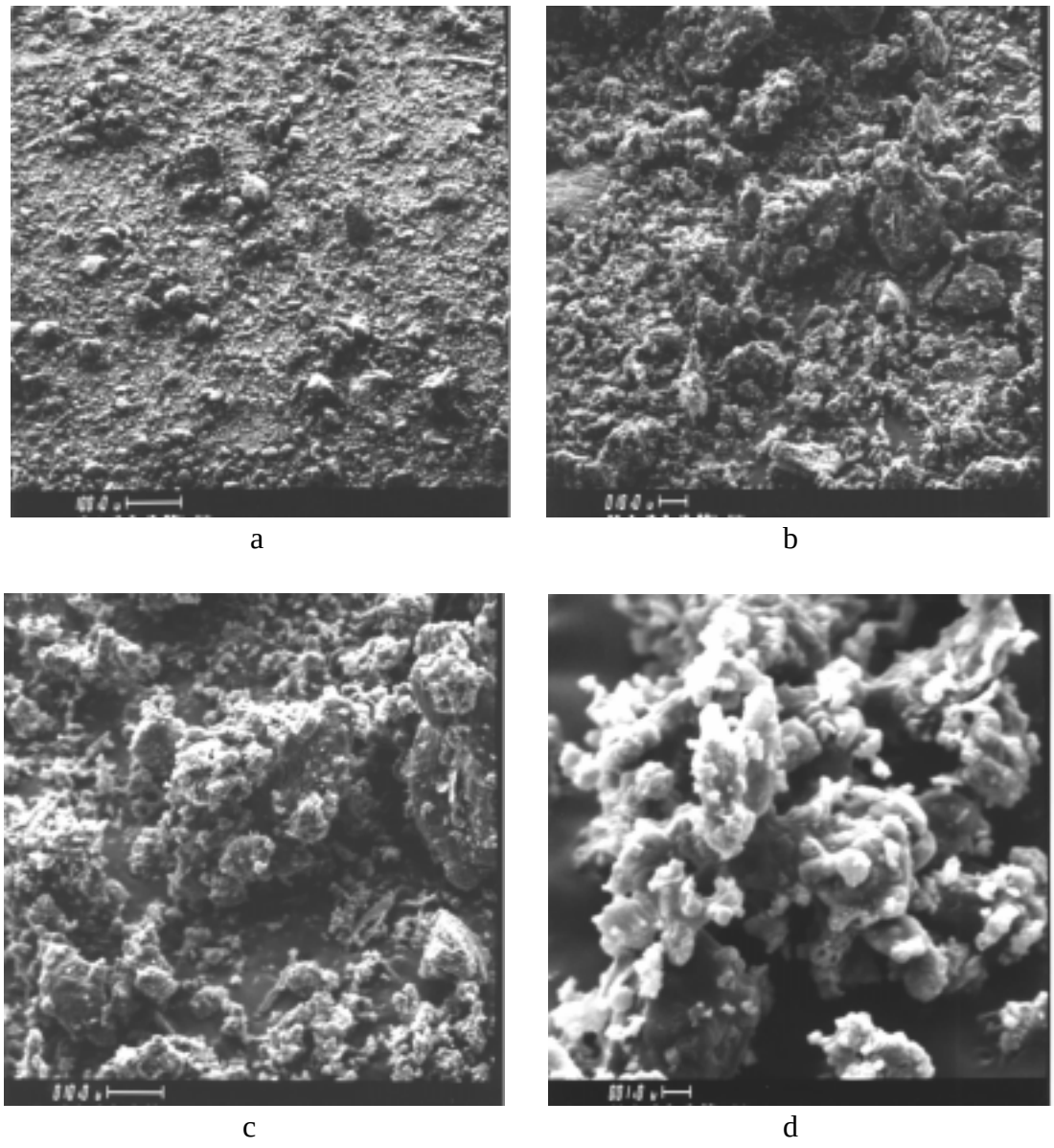

Figure 4-4. Representative SEM photographs of Tidd filter cake ash (ID # 4144) taken at a) 100X, b) 500X, c) 1000X, and d) 5000X.

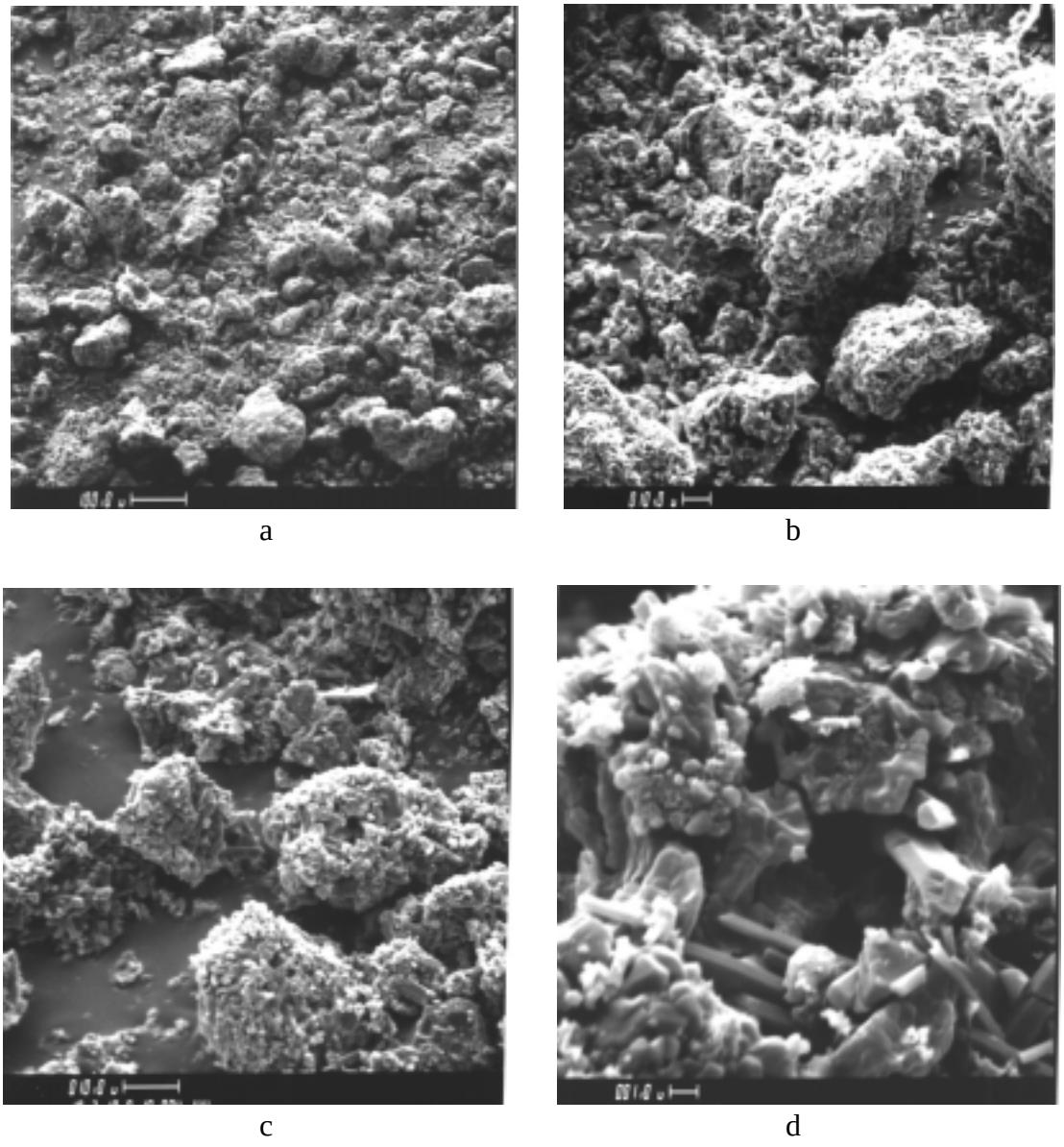

Figure 4-5. Representative SEM photographs of size fractionated Tidd filter cake ash (ID # 4320, diameter > 45 µm) taken at a) 100X, b) 500X, c) 1000X, and d) 5000X.

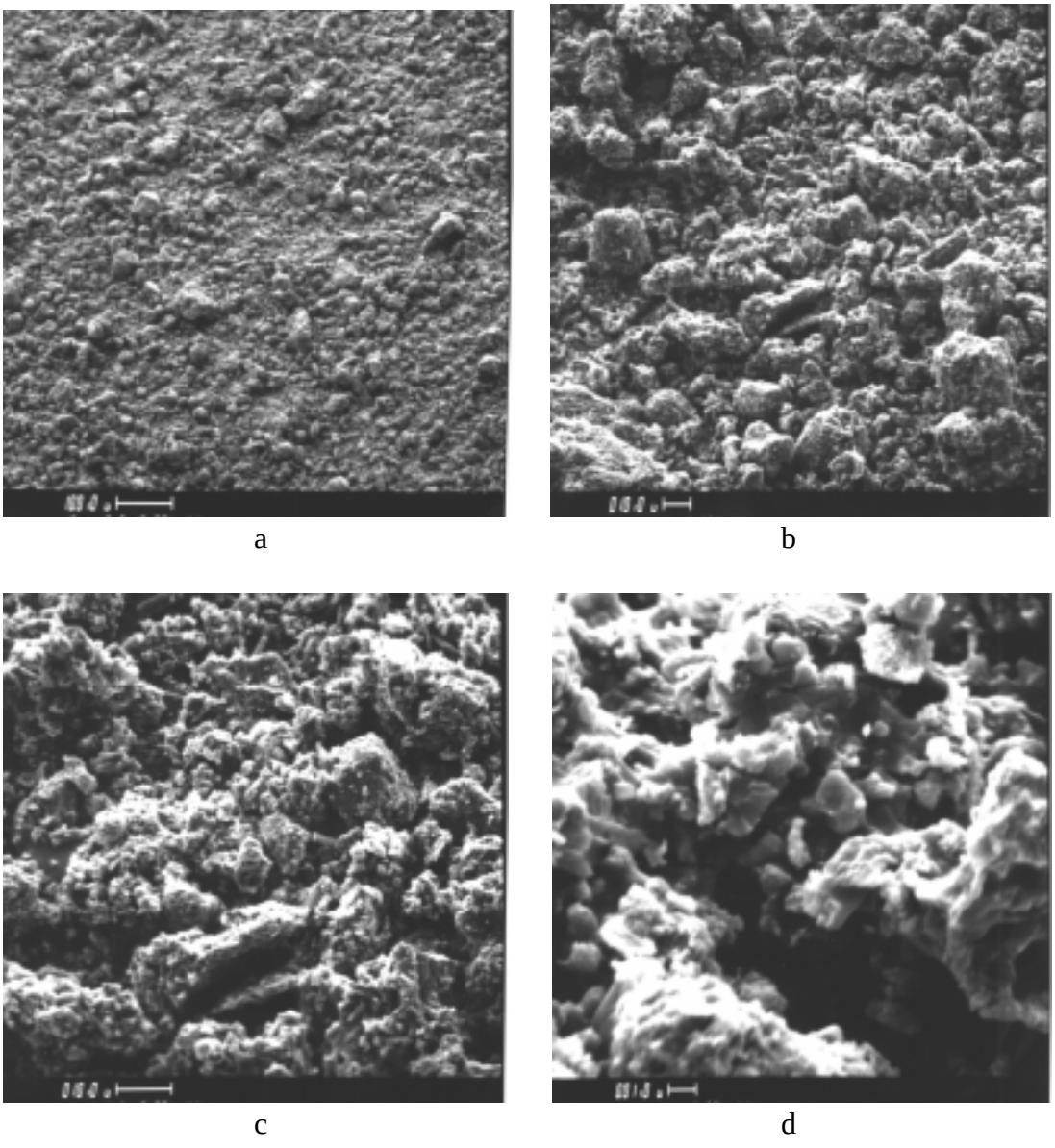

a b

c d

Figure 4-6. Representative SEM photographs of size fractionated Tidd filter cake ash (ID # 4321, 15 µm < diameter < 45 µm) taken at a) 100X, b) 500X, c) 1000X, and d) 5000X.

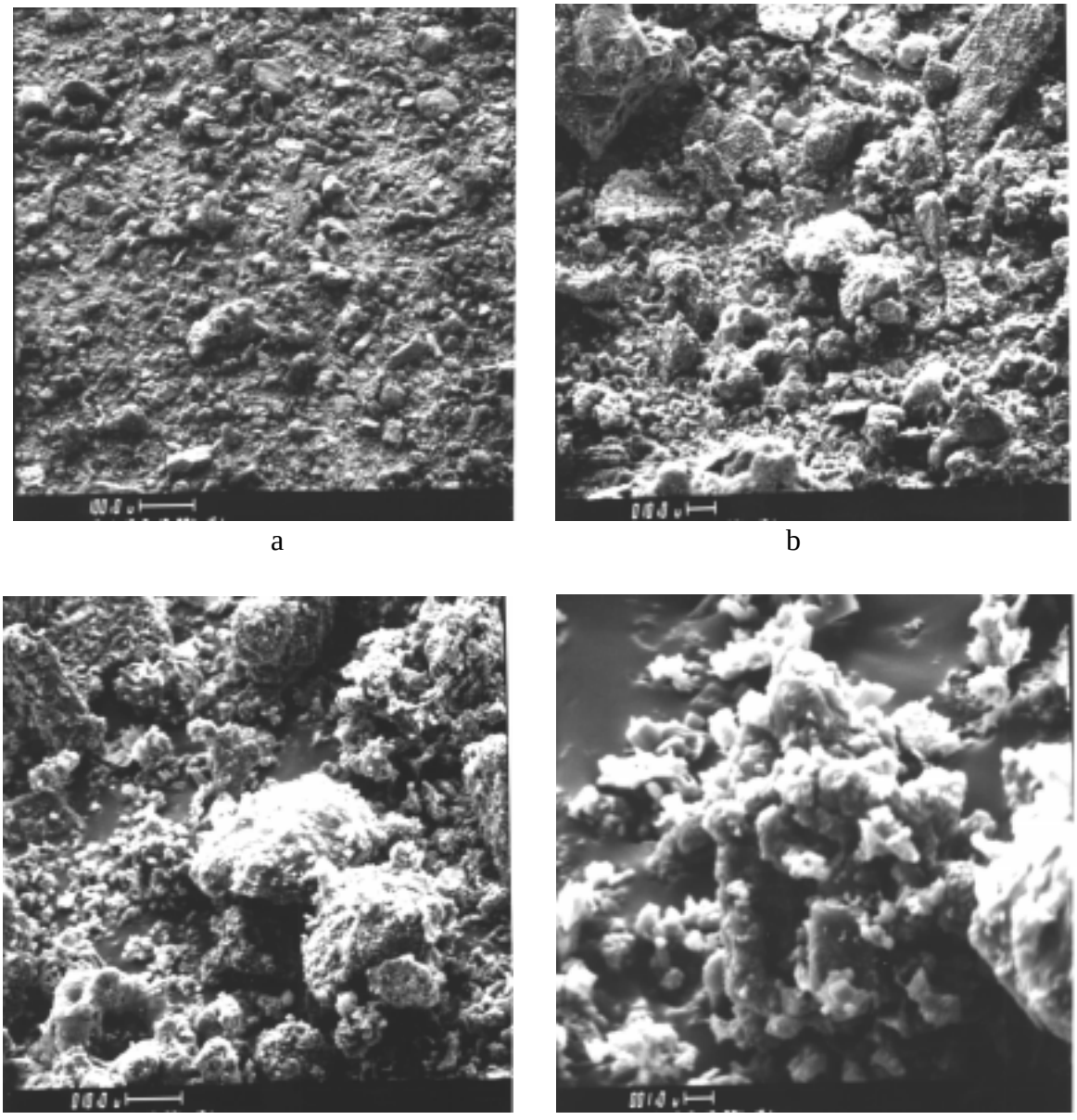

a b

c d

Figure 4-7. Representative SEM photographs of size fractionated Tidd ash taken from a tube sheet deposit (ID # 4151) taken at a) 100X, b) 500X, c) 1000X, and d) 5000X.

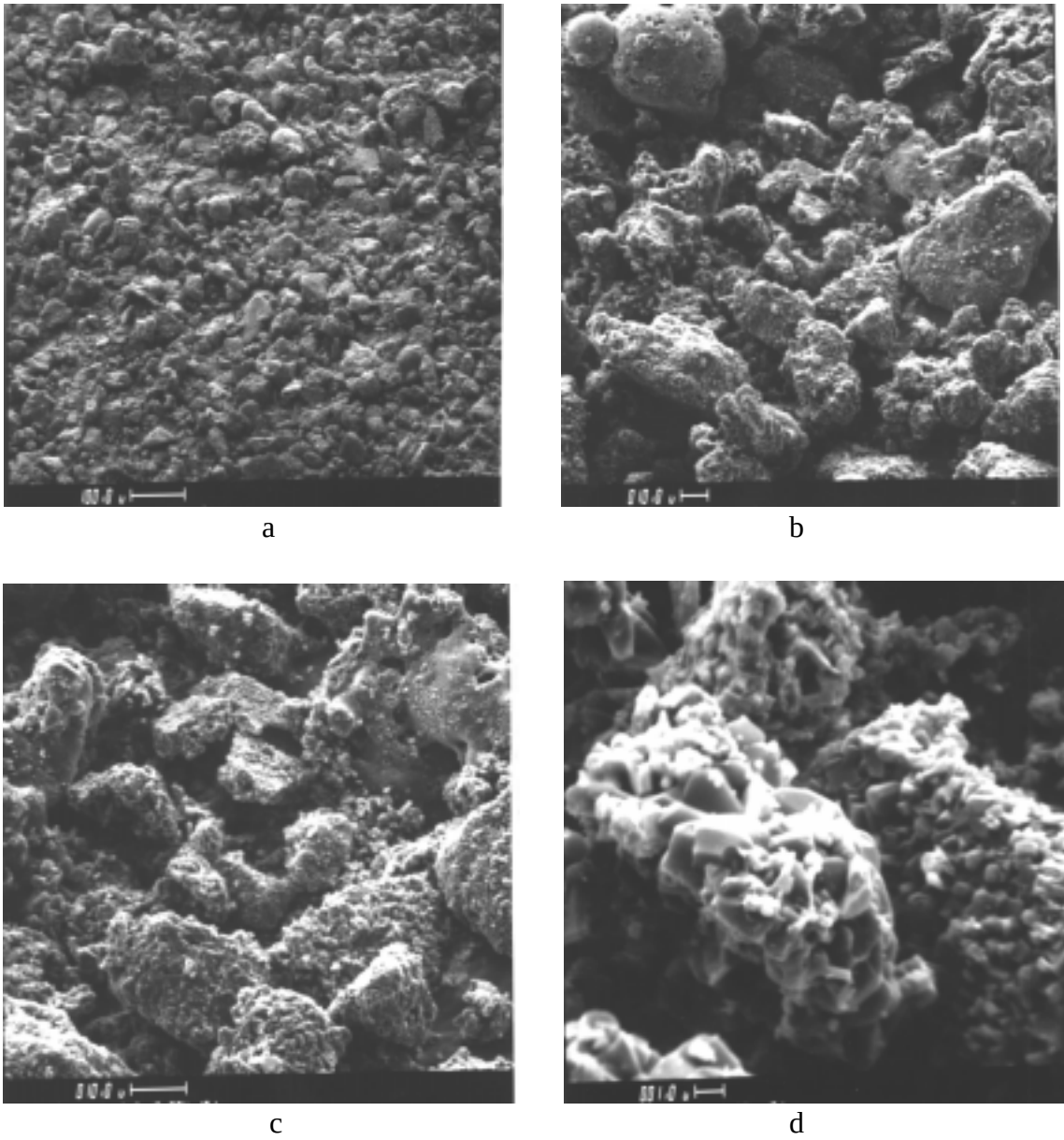

a b

c d

Figure 4-8. Representative SEM photographs of size fractionated Tidd ash taken from a tube sheet deposit (ID # 4322, diameter > 45 µm) taken at a) 100X, b) 500X, c) 1000X, and d) 5000X.

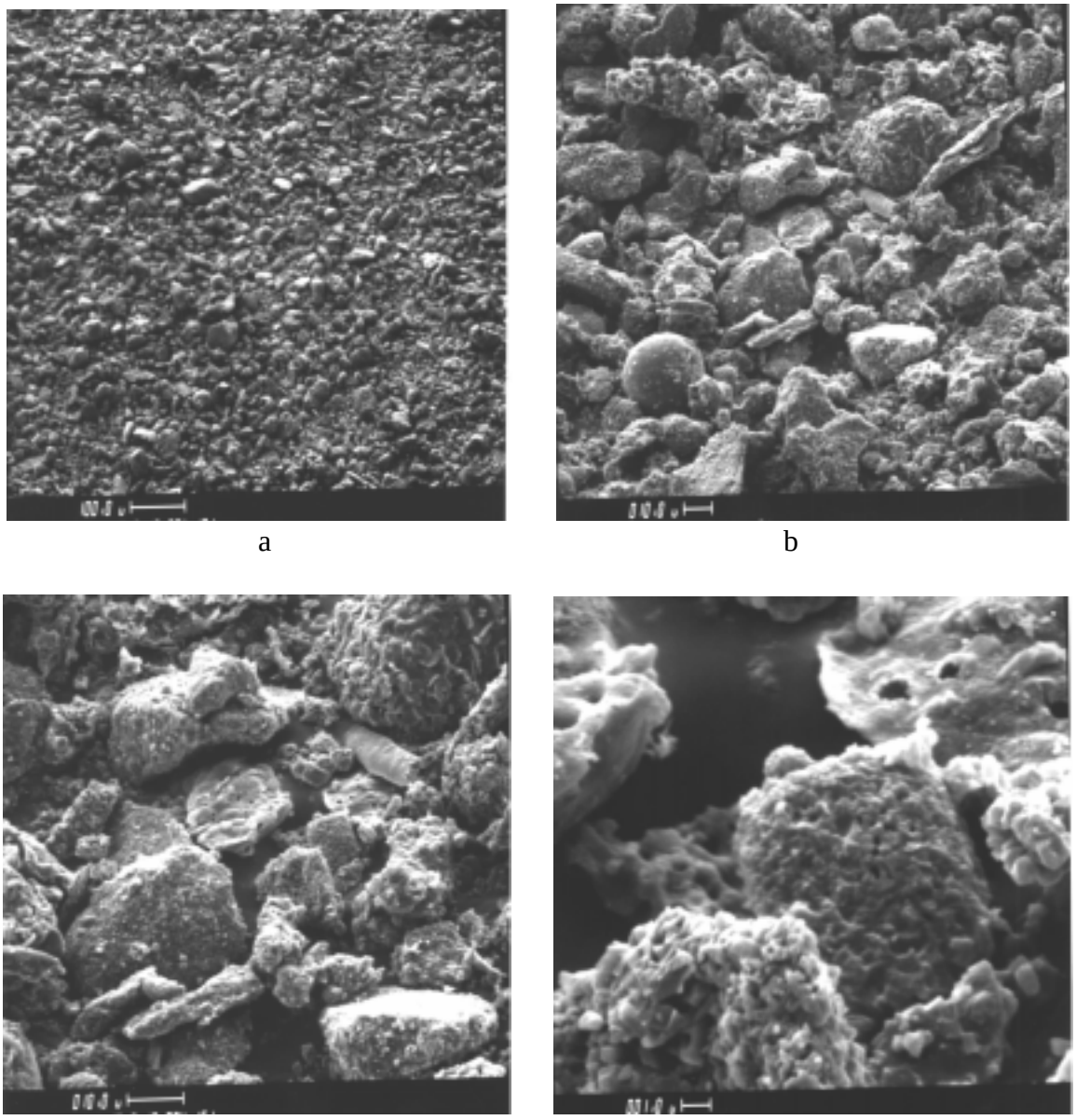

a b

c d

Figure 4-9. Representative SEM photographs of size fractionated Tidd ash taken from a tube sheet deposit (ID # 4323, 15 µm < diameter < 45 µm) taken at a) 100X, b) 500X, c) 1000X, and d) 5000X.

Figures 4-10 through 4-14 present representative views of a variety of ash samples obtained from the Tidd APF. These micrographs qualitatively illustrate the shape and size distribution of many of the Tidd ash samples discussed in this section.

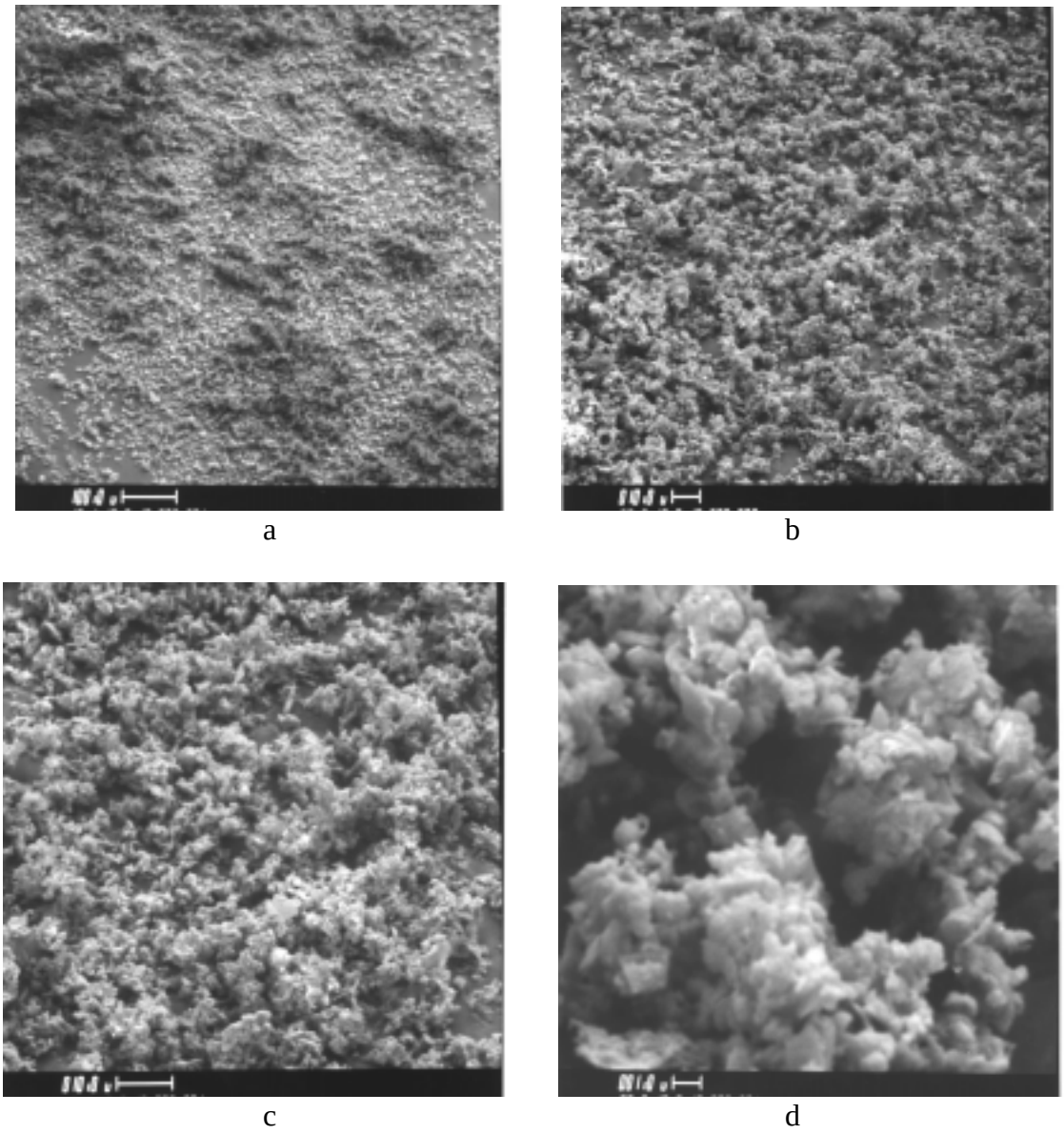

a b c d

Figure 4-10. Representative SEM photographs of Tidd ash from the hopper of the cyclone upstream of the APF (ID # 2791) taken at a) 100X, b) 500X, c) 1000X, and d) 5000X.

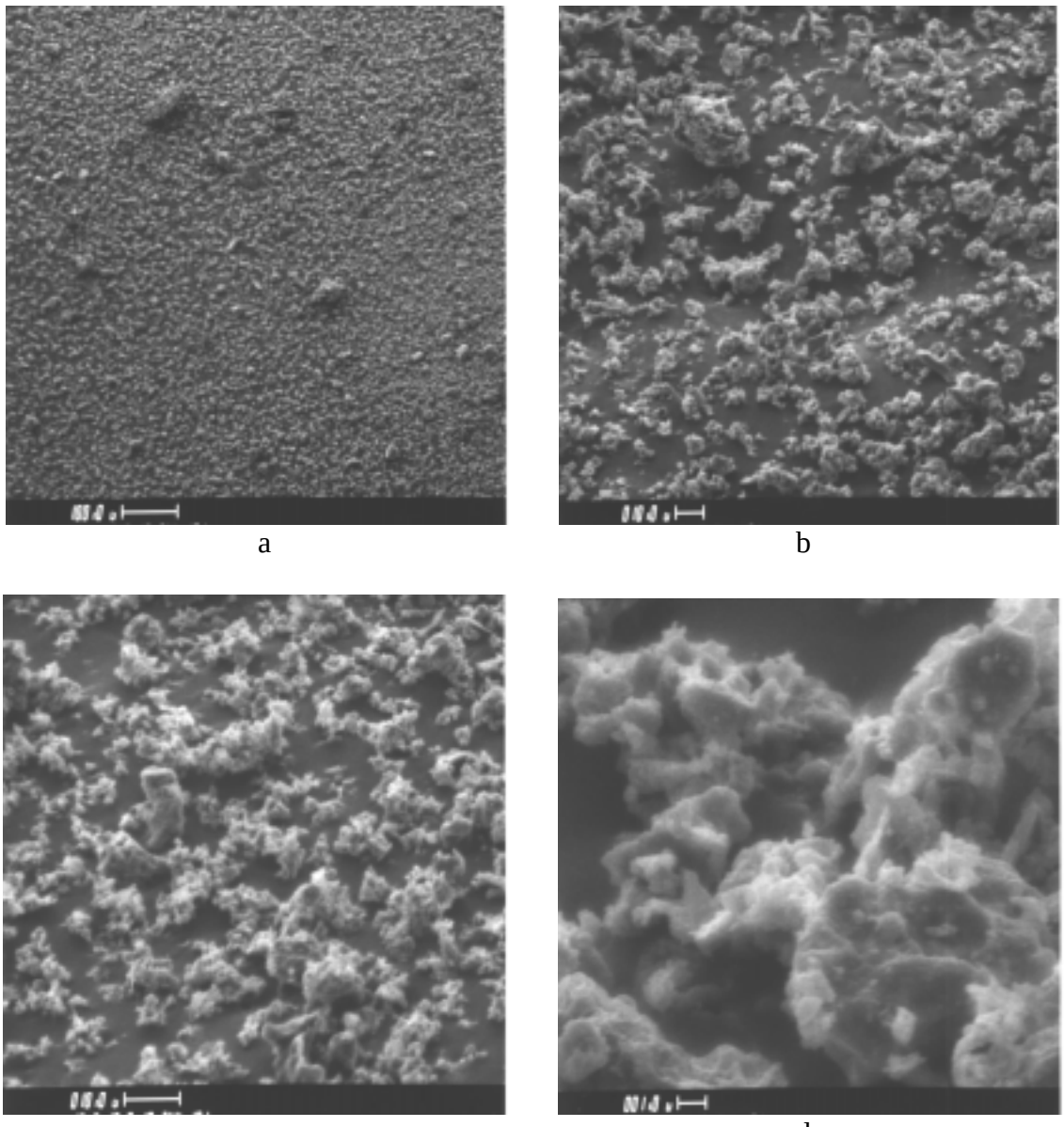

Figure 4-11. Representative SEM photographs of Tidd APF hopper ash (ID # 2822) taken at a) 100X, b) 500X, c) 1000X, and d) 5000X.

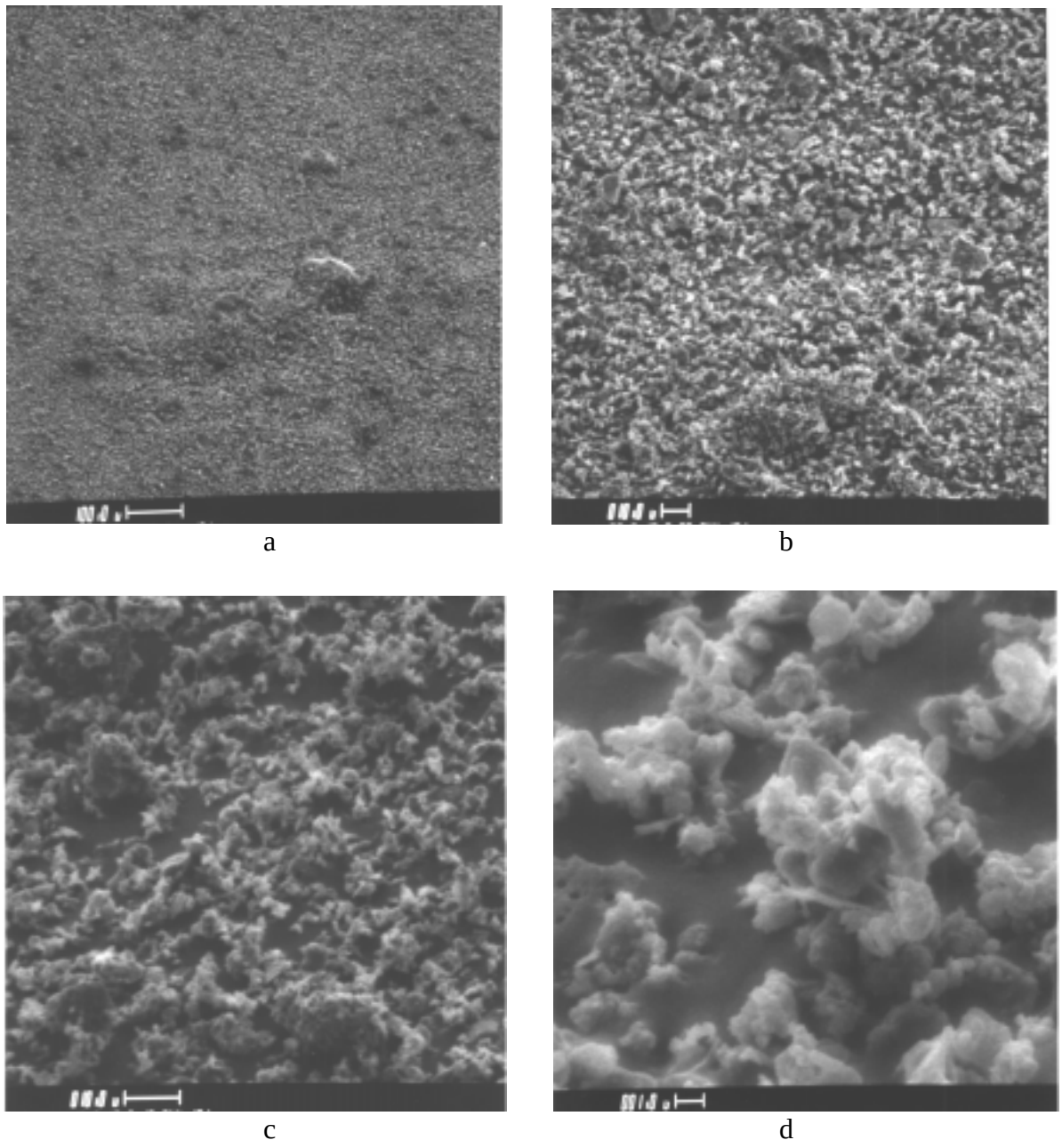

Figure 4-12. Representative SEM photographs of Tidd APF hopper ash (ID # 2823) taken at a) 100X, b) 500X, c) 1000X, and d) 5000X.

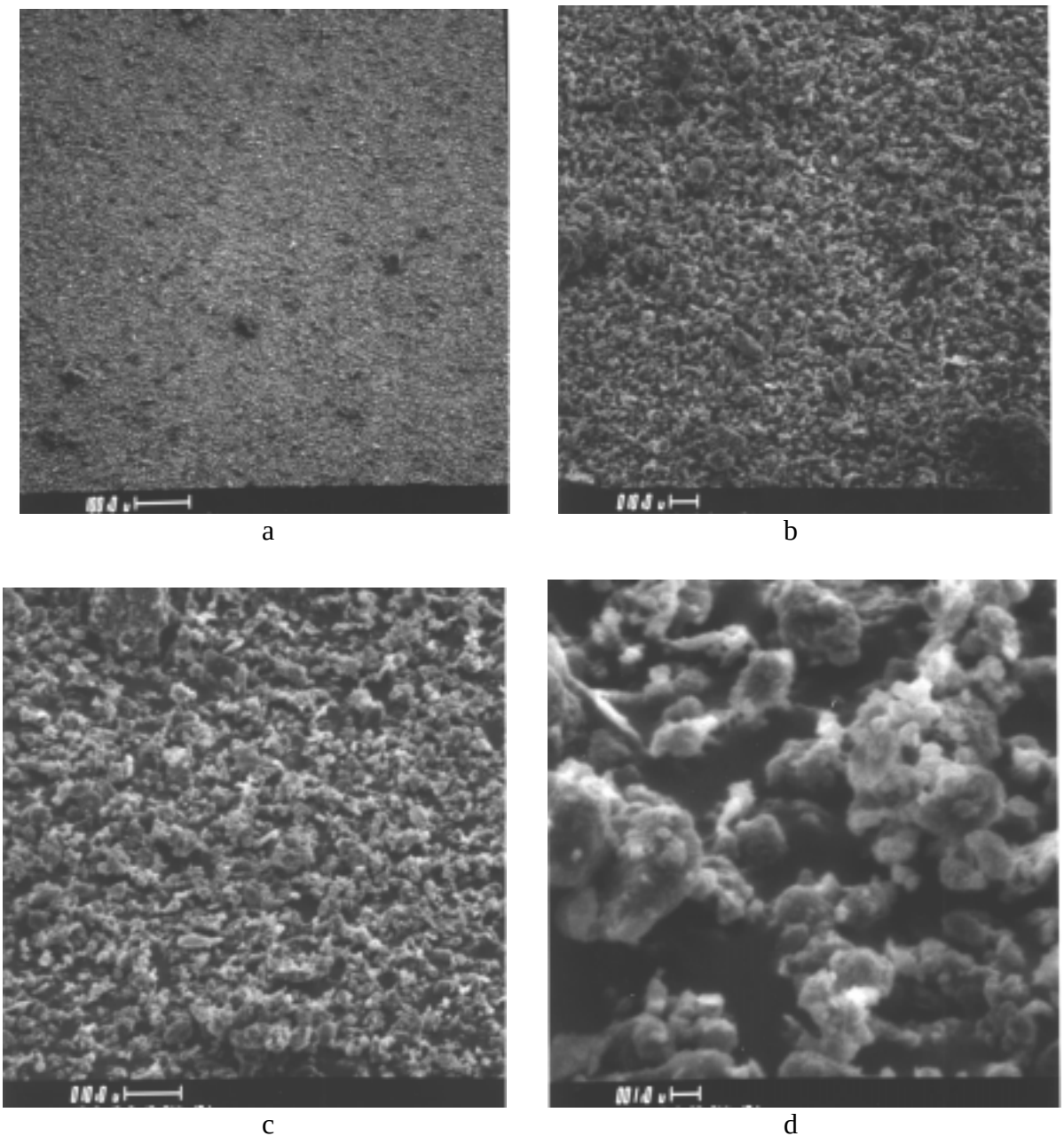

Figure 4-13. Representative SEM photographs of Tidd APF hopper ash (ID # 2824) taken at a) 100X, b) 500X, c) 1000X, and d) 5000X.

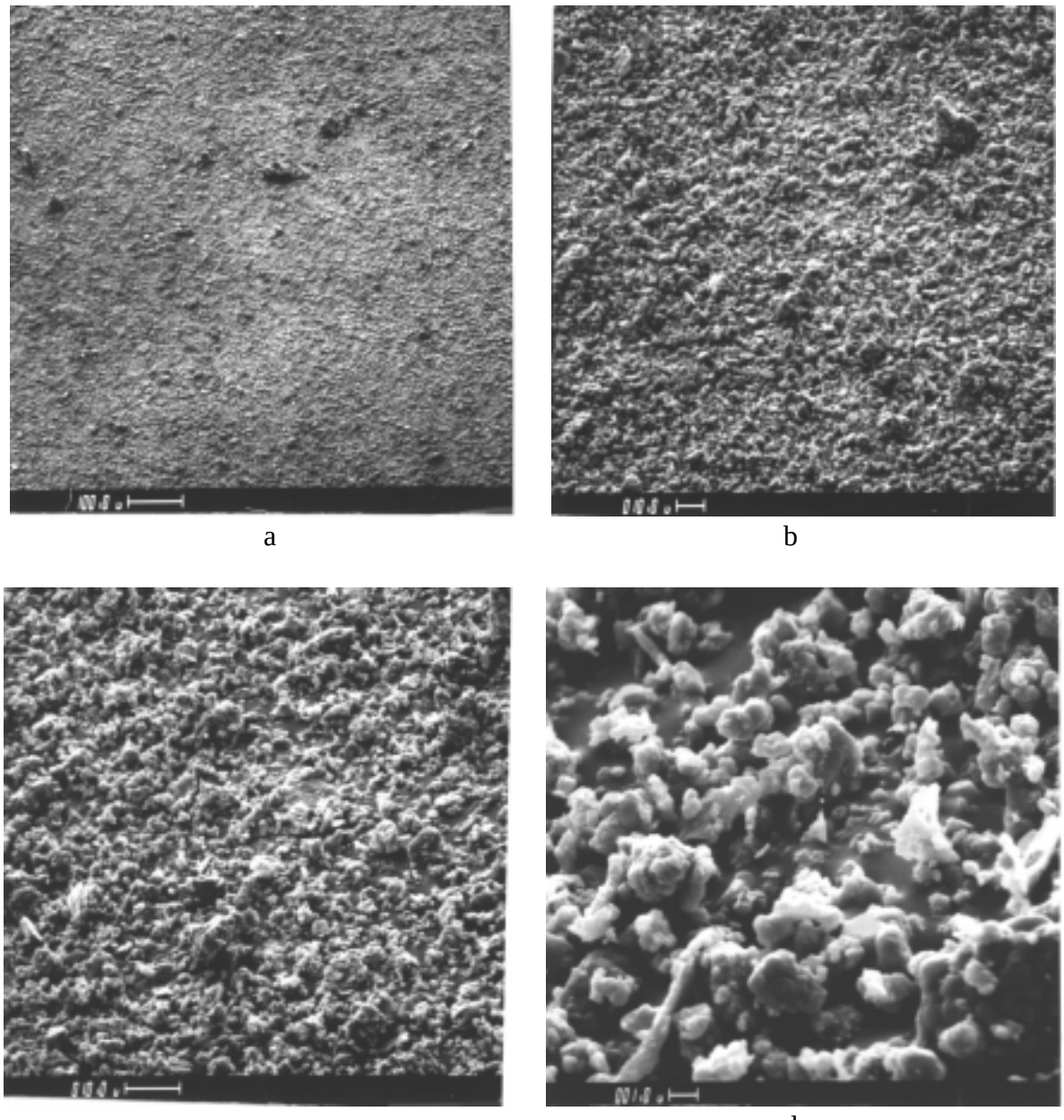

Figure 4-14. Representative SEM photographs of Tidd ash (ID # 4114; MP,AS) taken at a) 100X, b) 500X, c) 1000X, and d) 5000X.

An SEM microprobe was used to examine agglomerates of ash obtained from the filter vessel in May 1994 (ID #s 4078 and 4087). The device performs elemental analyses on selected 1 µm diameter hemispherical regions. There was little consistency from region to region in the various specimens that were examined. Each particle observed was apparently a special case. Some particles were almost completely iron, others were very high in calcium or magnesium. Aluminosilicate particles were also common. The shapes and sizes of the particles also varied considerably. Some particles showed evidence of having been melted and resolidified. Such particles, to the extent that it was possible to determine, were enriched in magnesium (presumably because of the formation of $MgSO_4$). The bonds between particles showed some enhanced levels of Mg, accompanied by such other species as Ti, Al, Ca, and S. Although conclusions are hard to verify because of the limitations of the technique and the heterogeneity of the samples, particles rich in Mg and S apparently softened during combustion and/or collection and residence in the filter vessel. The presence of significant amounts of Mg and S in the ash particles may have enhanced the chances for eutectic formation between particles.

A variety of SEM analyses were also performed on a nodule from a filter cake sample (ID # 4012) collected in September 1993. The objective of these analyses was the determination of the morphology and composition of the interparticle bonds in the ash deposits formed in the filtration assembly. Highly informative micrographs of a fresh fracture surface of this nodule are presented in Figures 4-15 and 4-16. These micrographs were generated using a nodule in the condition it was removed from the APF (i.e. not encapsulated in epoxy). (These same micrographs are also presented (without spectra locations) and discussed in section *5.8 Consolidation and Bridging of Ash Deposits in PFBC Filters*.) The appearance of the interparticle bonds and overall structure of this fracture surface strongly support a mechanism that involves some type of microscopic melting in the ash deposit after it is initially collected. To examine the chemical nature of the interparticle bonds and the particles that seem to be embedded in them, EDX spectra were obtained at the locations called out on the micrographs in Figures 4-15 and 4-16. These spectra are presented in Figures 4-17 through 4-34, and generally indicate that calcium and sulfur are always found in significant proportions in the locations thought to represent the material that seems to be bridged between particles (locations that are labeled with a B). However, these bridges or bonds also seem to include relatively high proportions of a variety of other elements (aluminum, silica, iron, and potassium). However, the resolution of the EDX technique (about 1 µm) is about the same dimension as the structures that are being examined, and also this technique samples a volume of the sample material (not just the surface of the structure seen in Figures 4-15 and 4-16). Therefore these spectra may indicate the composition of not only the apparent bond specified in the micrograph, but also any particles that may be embedded just under the surface of the bond. In fact, all the apparent bonding or bridging locations visible in these micrographs appear to have particles embedded in them. The apparent physical structure of these bonds supports the mechanism of eutectic formation described in section *5.8 Consolidation and Bridging of Ash Deposits in PFBC Filters*.

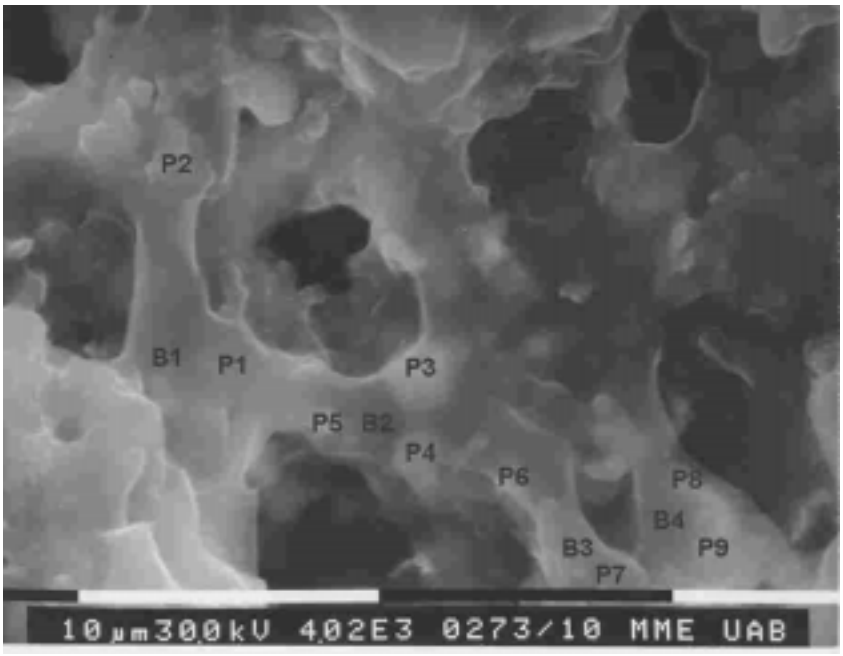

Figure 4-15. Scanning electron micrograph of a fresh internal fracture surface of a filter cake ash nodule from Tidd (ID # 4012). The white bars at the bottom of the micrograph represent lengths of 10 µm. Locations where EDX spectra were measured are identified on this figure.

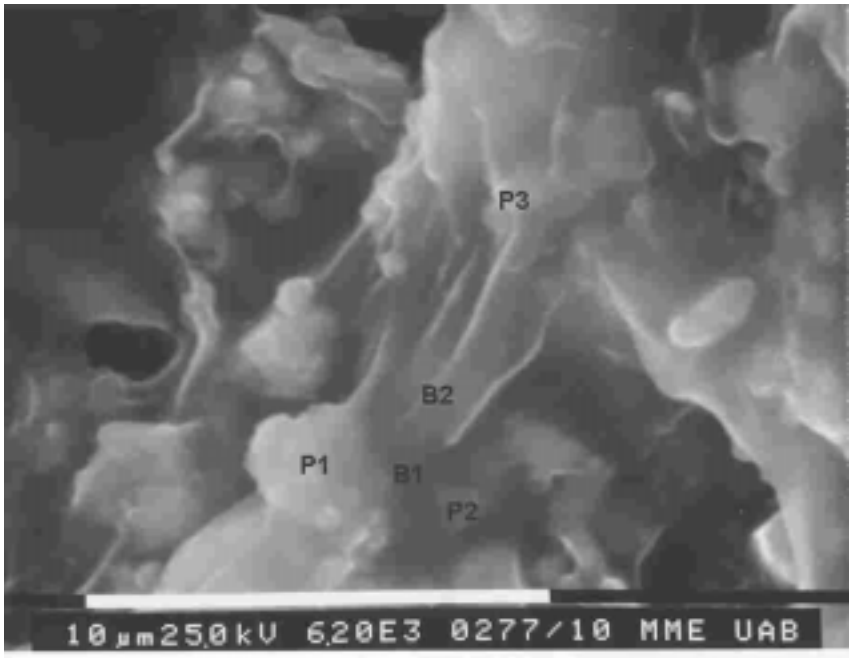

Figure 4-16. Scanning electron micrograph of a fresh internal fracture surface of a filter cake ash nodule from Tidd (ID # 4012). The white bar at the bottom of the micrographs represents a length of 10 µm. Locations where EDX spectra were measured are identified on this figure.

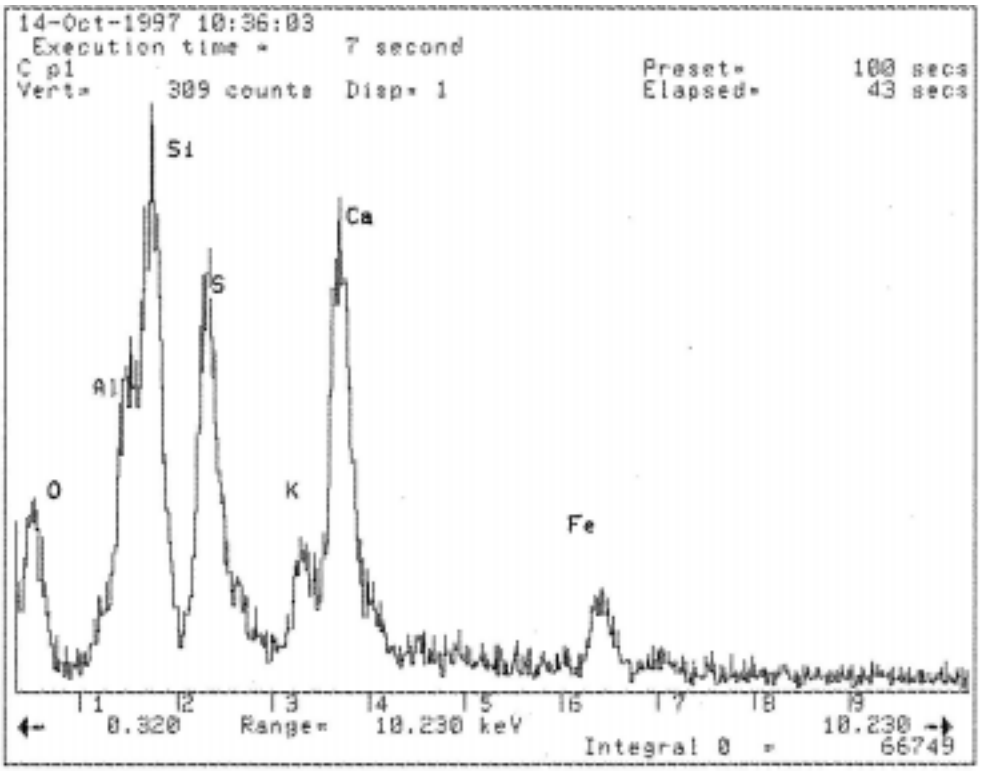

Figure 4-17. EDX spectrum taken at location P1 on the fracture surface of the Tidd filter cake nodule shown in Figure 4-15.

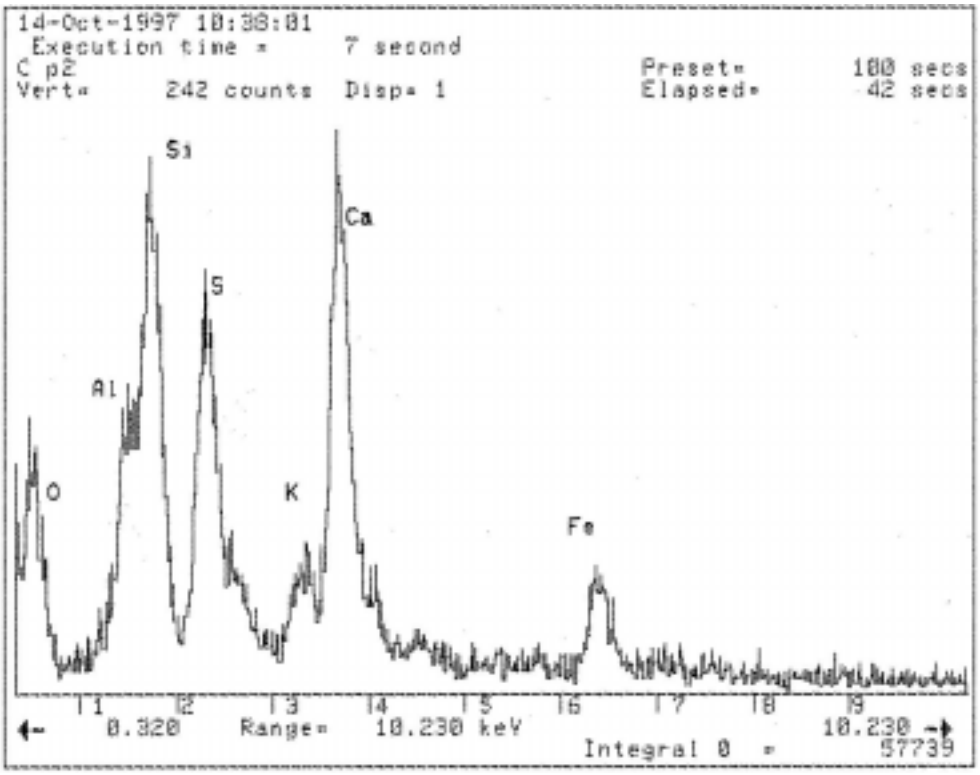

Figure 4-18. EDX spectrum taken at location P2 on the fracture surface of the Tidd filter cake nodule shown in Figure 4-15.

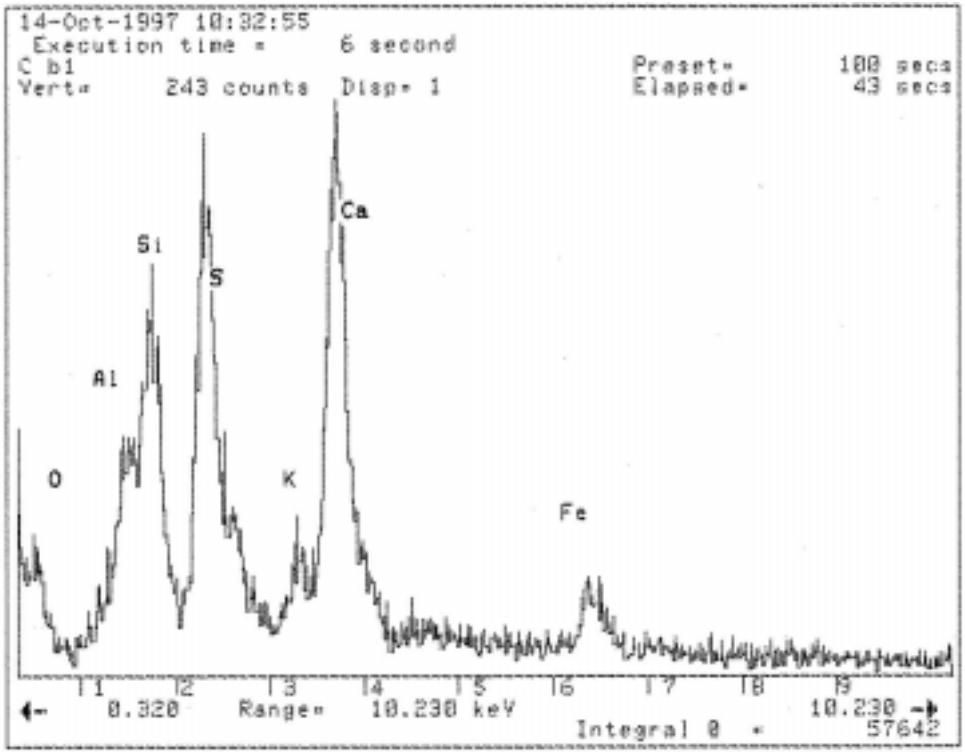

Figure 4-19. EDX spectrum taken at location B1 on the fracture surface of the Tidd filter cake nodule shown in Figure 4-15.

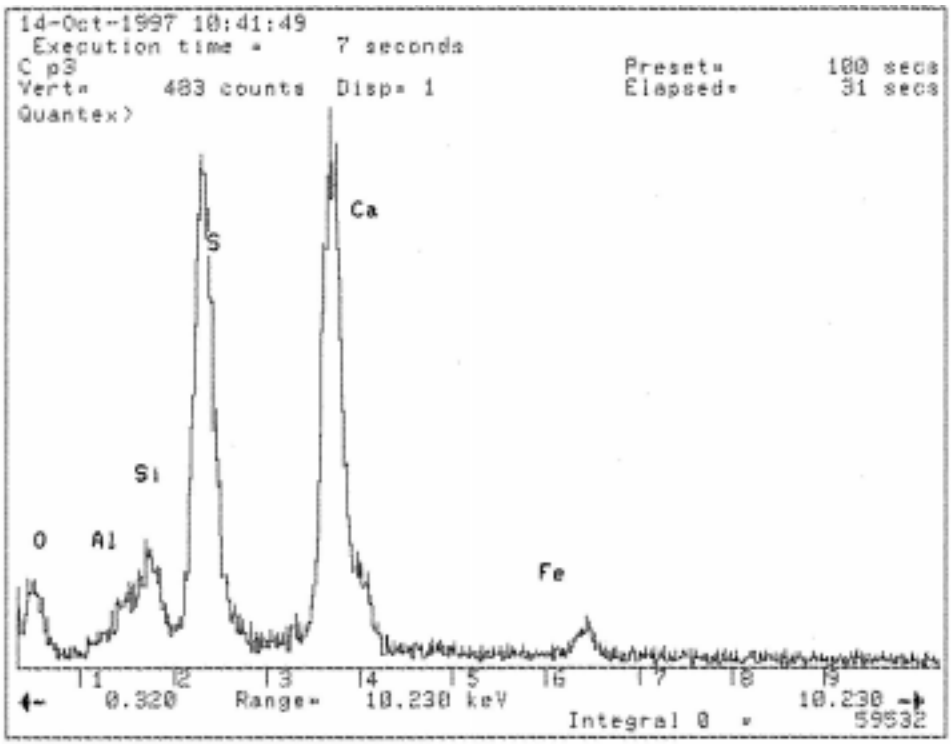

Figure 4-20. EDX spectrum taken at location P3 on the fracture surface of the Tidd filter cake nodule shown in Figure 4-15.

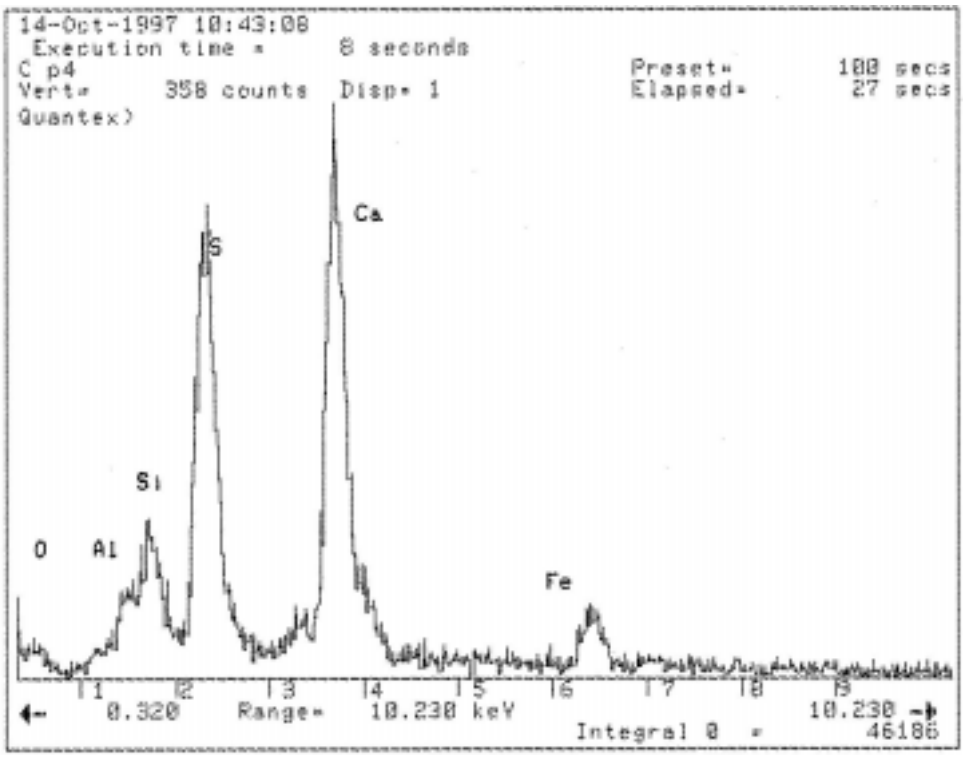

Figure 4-21. EDX spectrum taken at location P4 on the fracture surface of the Tidd filter cake nodule shown in Figure 4-15.

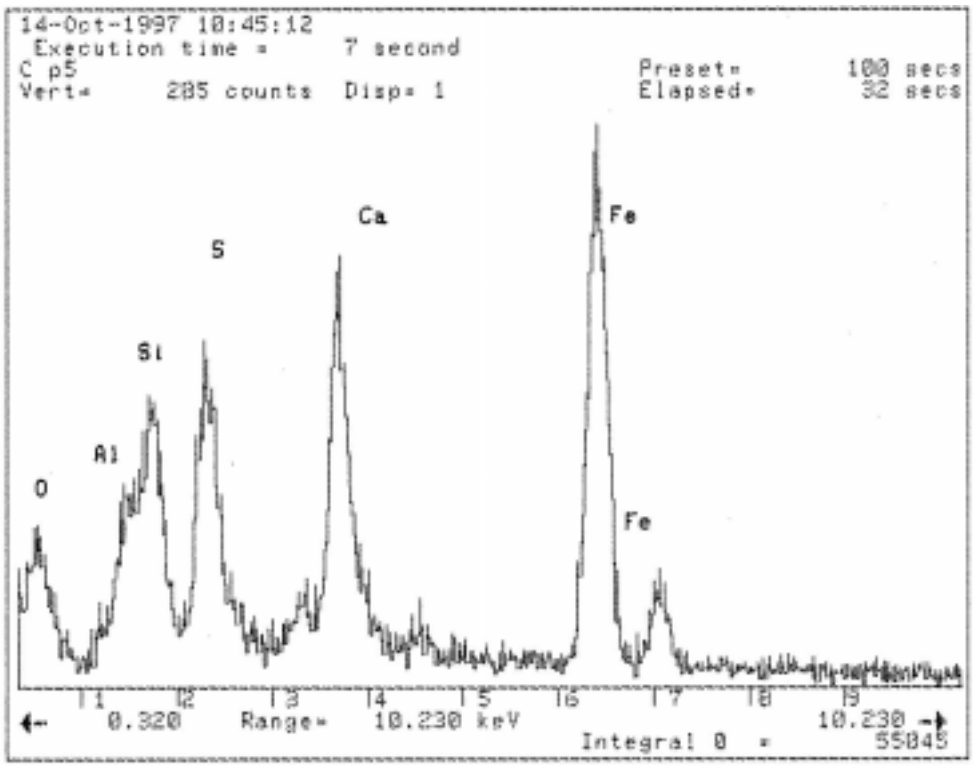

Figure 4-22. EDX spectrum taken at location P5 on the fracture surface of the Tidd filter cake nodule shown in Figure 4-15.

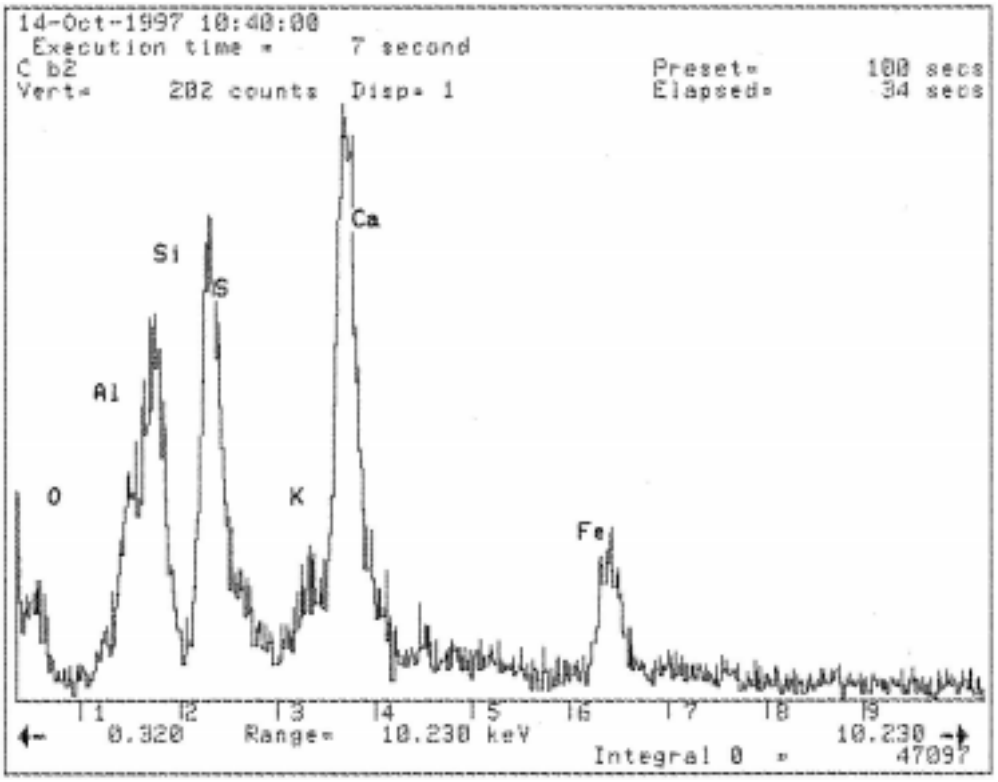

Figure 4-23. EDX spectrum taken at location B2 on the fracture surface of the Tidd filter cake nodule shown in Figure 4-15.

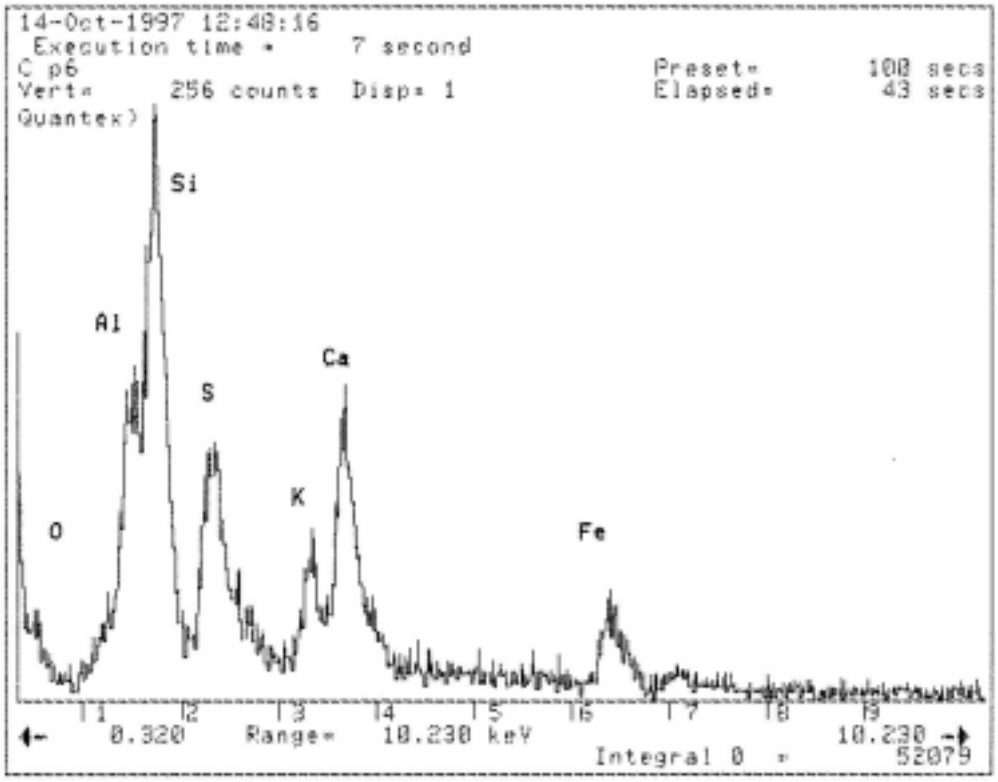

Figure 4-24. EDX spectrum taken at location P6 on the fracture surface of the Tidd filter cake nodule shown in Figure 4-15.

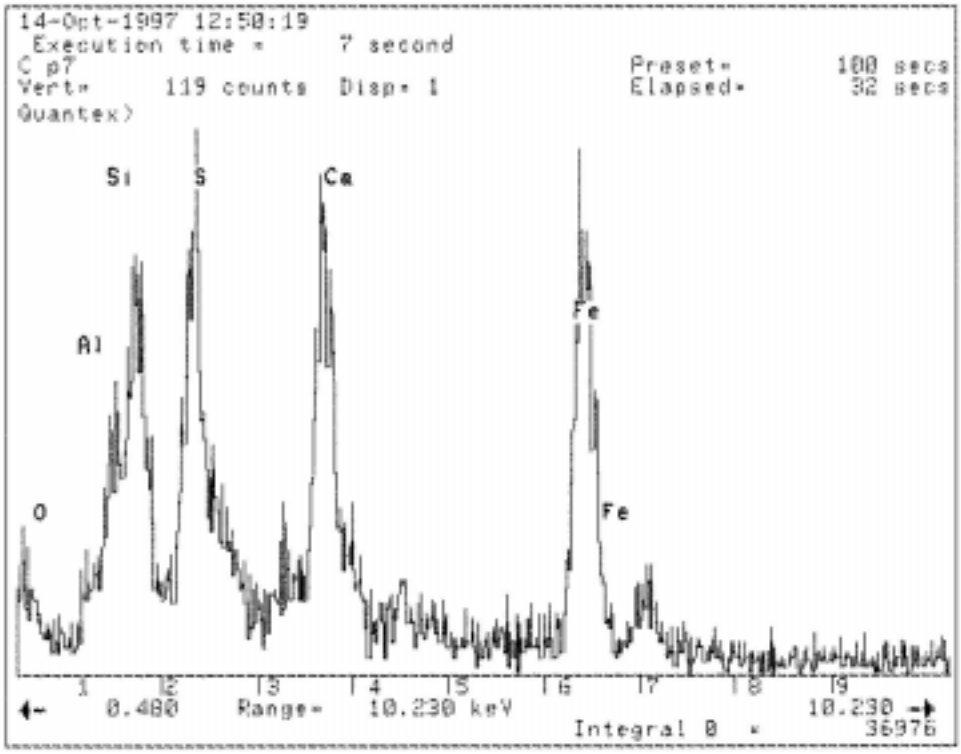

Figure 4-25. EDX spectrum taken at location P7 on the fracture surface of the Tidd filter cake nodule shown in Figure 4-15.

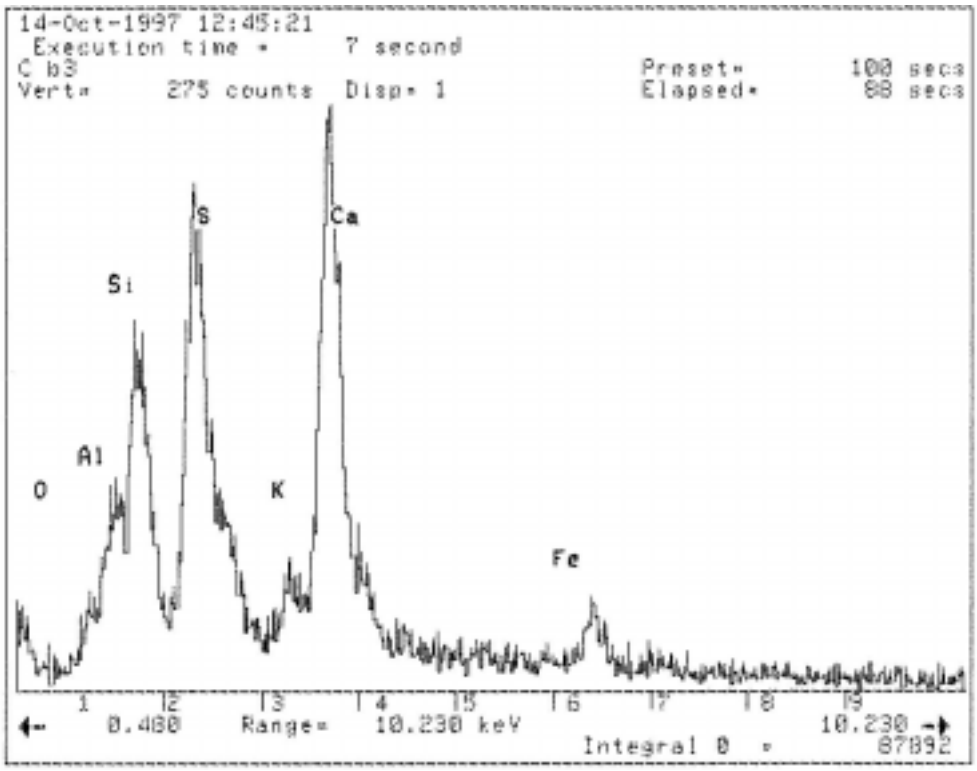

Figure 4-26. EDX spectrum taken at location B3 on the fracture surface of the Tidd filter cake nodule shown in Figure 4-15.

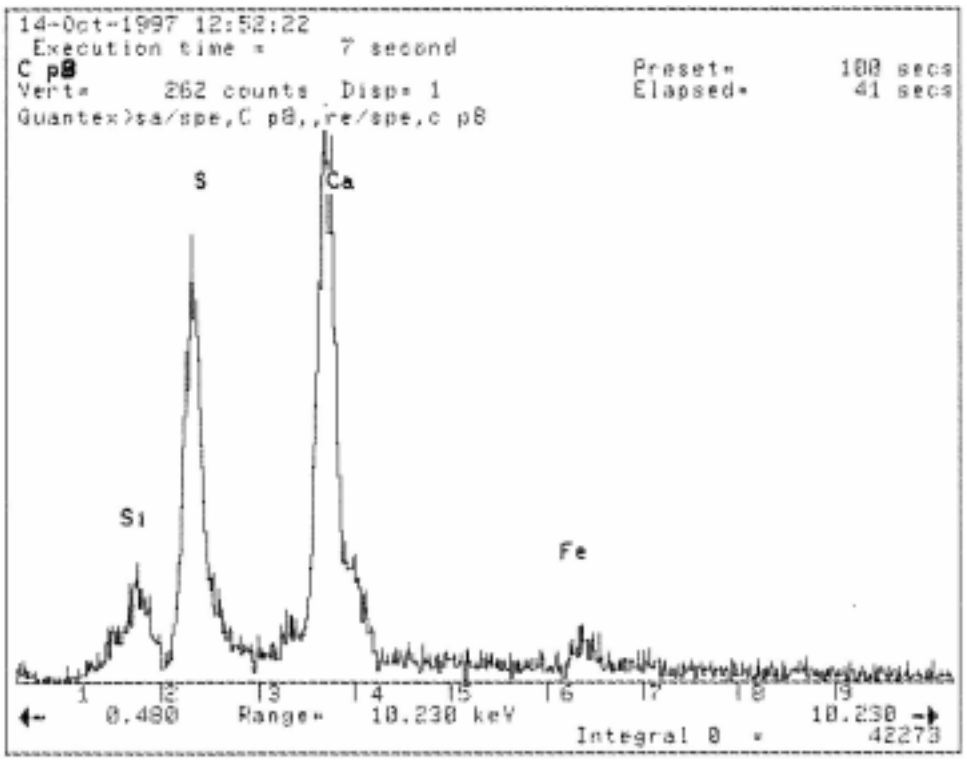

Figure 4-27. EDX spectrum taken at location P8 on the fracture surface of the Tidd filter cake nodule shown in Figure 4-15.

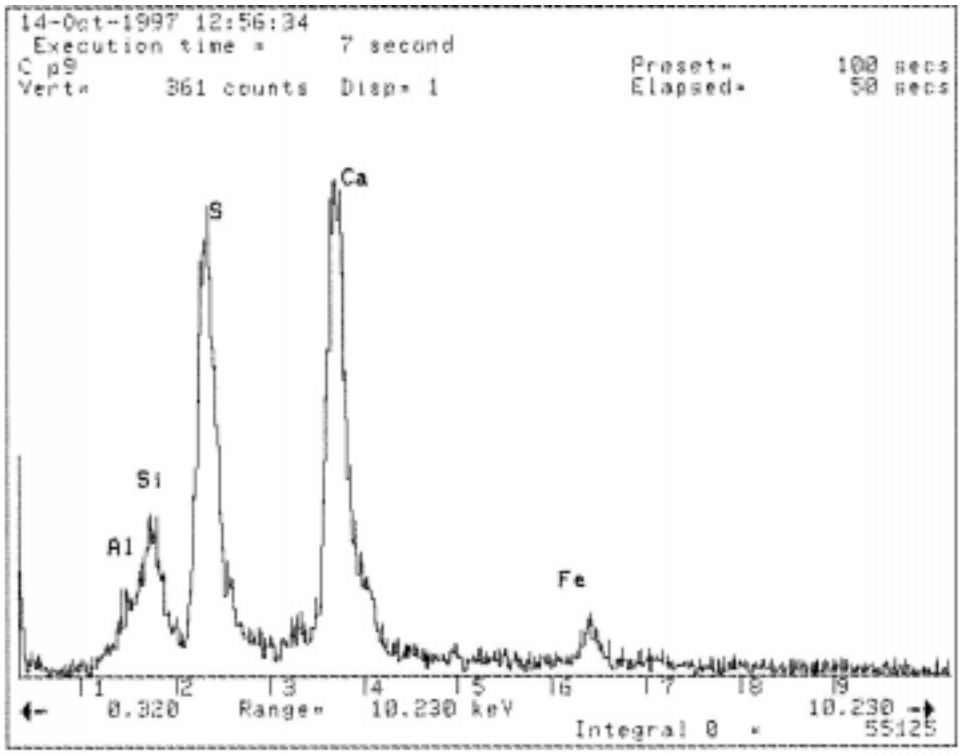

Figure 4-28. EDX spectrum taken at location P9 on the fracture surface of the Tidd filter cake nodule shown in Figure 4-15.

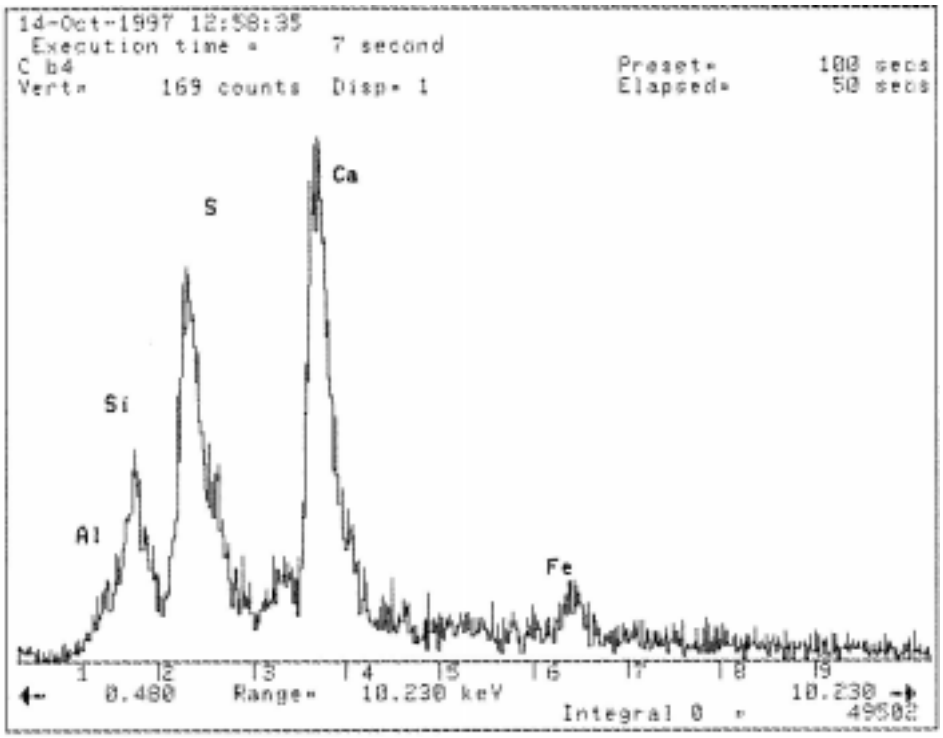

Figure 4-29. EDX spectrum taken at location B4 on the fracture surface of the Tidd filter cake nodule shown in Figure 4-15.

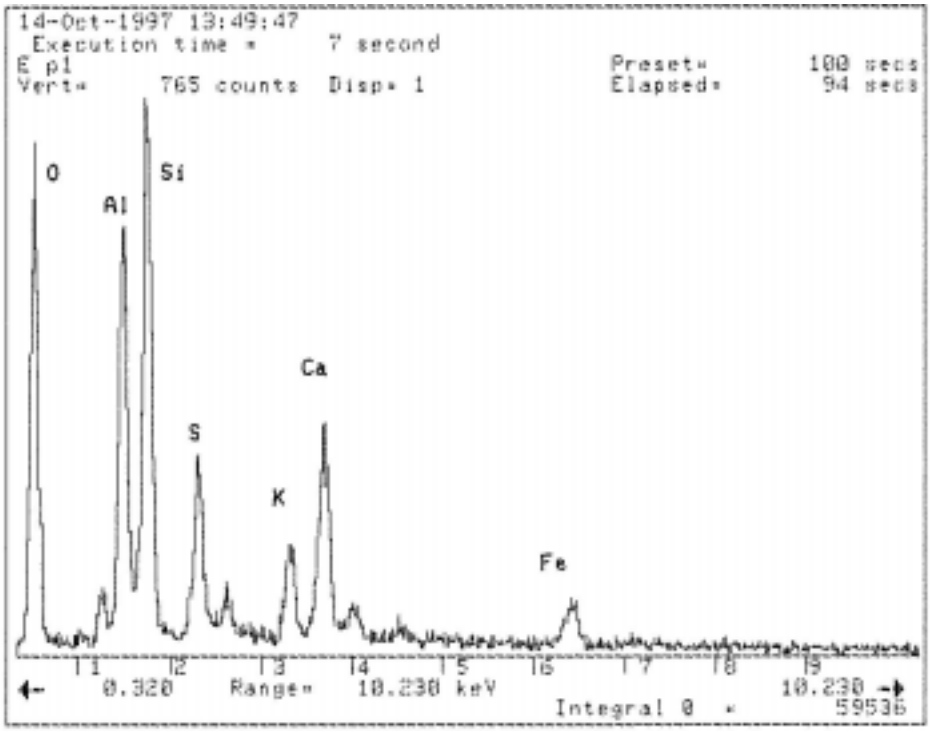

Figure 4-30. EDX spectrum taken at location P1 on the fracture surface of the Tidd filter cake nodule shown in Figure 4-16.

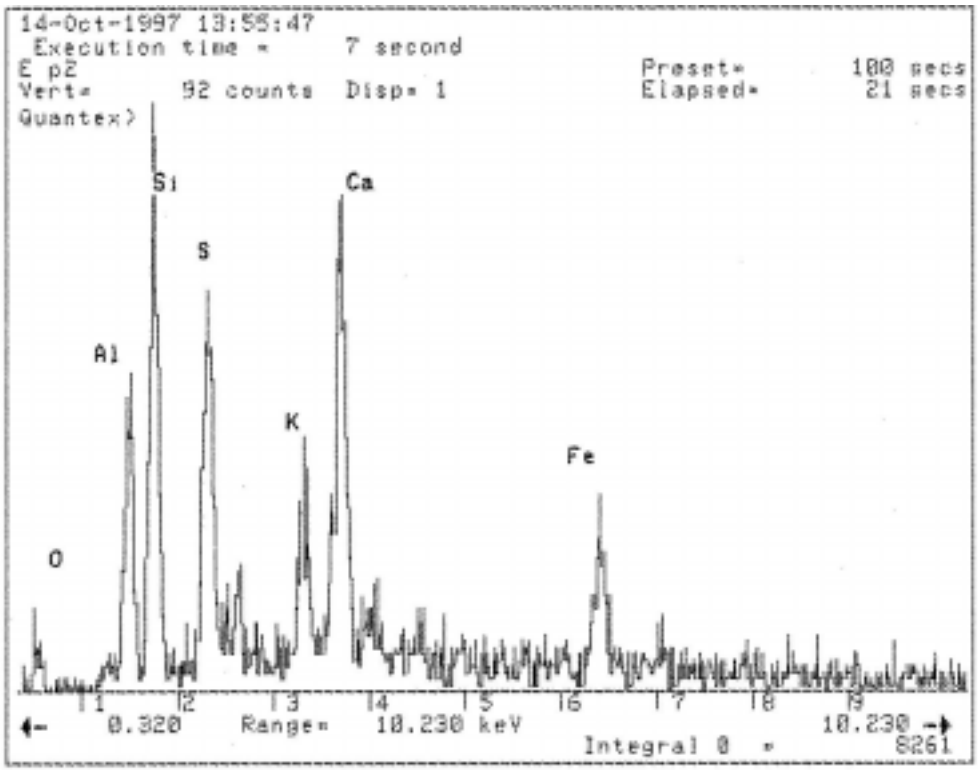

Figure 4-31. EDX spectrum taken at location P2 on the fracture surface of the Tidd filter cake nodule shown in Figure 4-16.

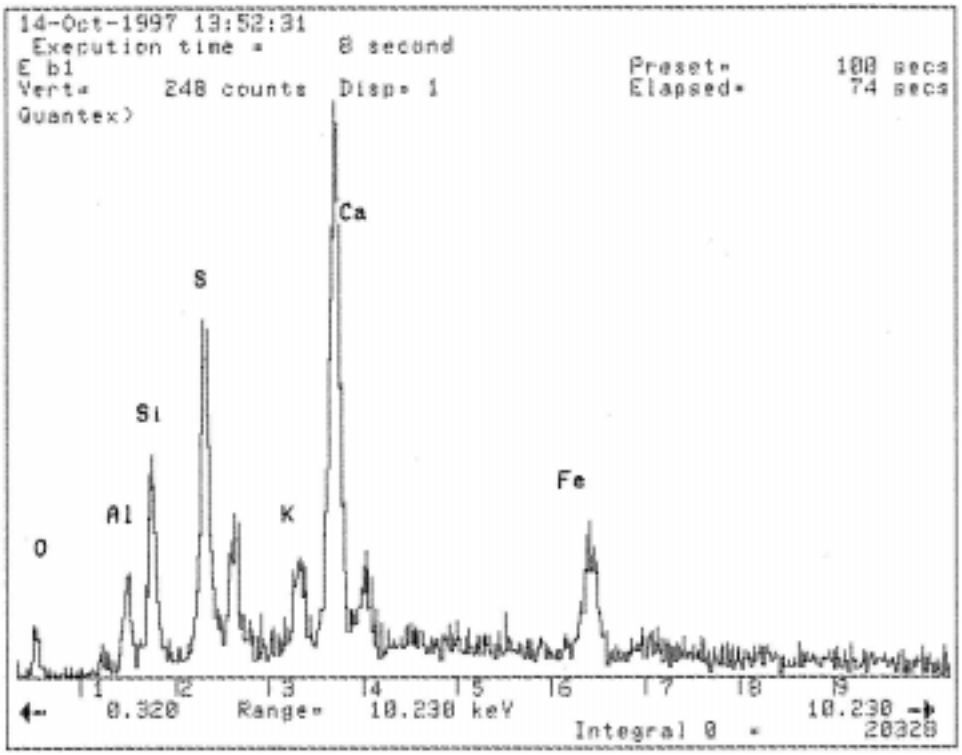

Figure 4-32. EDX spectrum taken at location B1 on the fracture surface of the Tidd filter cake nodule shown in Figure 4-16.

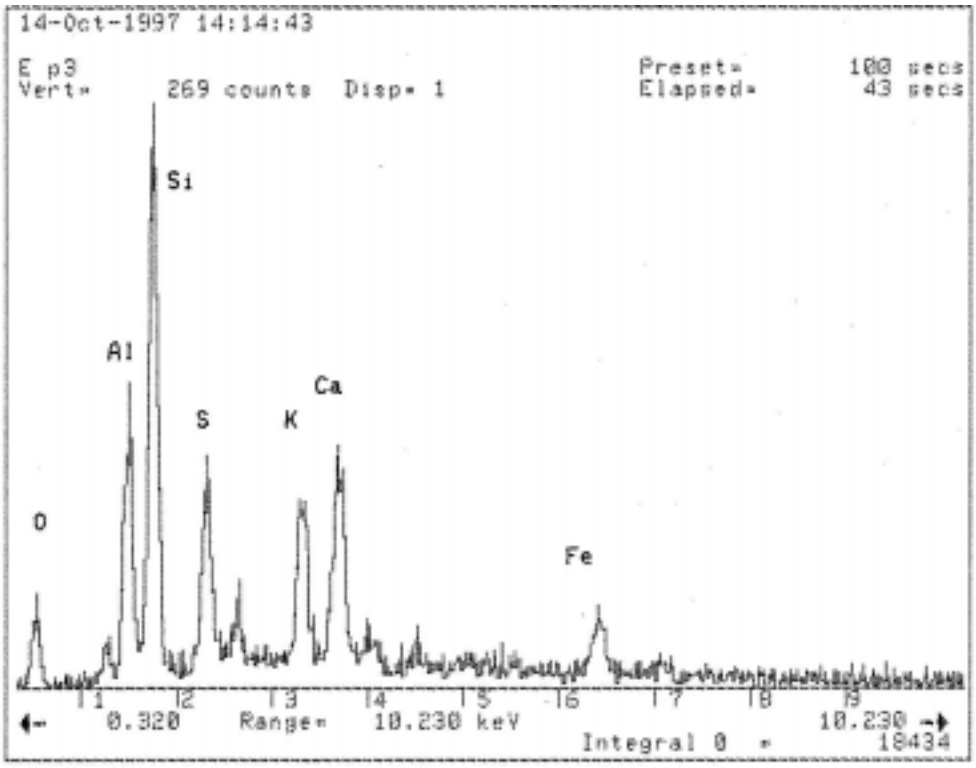

Figure 4-33. EDX spectrum taken at location P3 on the fracture surface of the Tidd filter cake nodule shown in Figure 4-16.

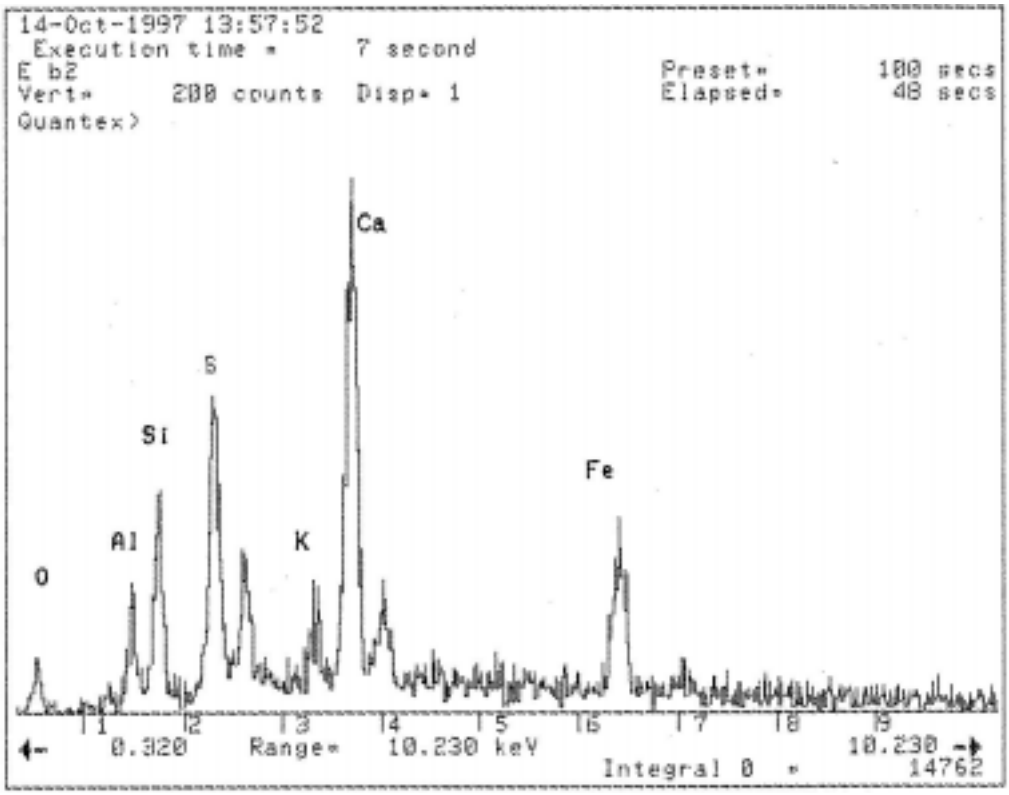

Figure 4-34. EDX spectrum taken at location B2 on the fracture surface of the Tidd filter cake nodule shown in Figure 4-16.

Additional micrographs illustrating the morphology of the interparticle bonds observed in sample # 4114 (MP, AS) obtained in October 1994 are shown in Figure 4-35. The appearance of these particles also suggests a melting, or welding, of adjacent particles occurred in the Tidd ash deposits. The implications of this type of morphology are discussed under section *5.8 Consolidation and Bridging of Ash Deposits in PFBC Filters*.

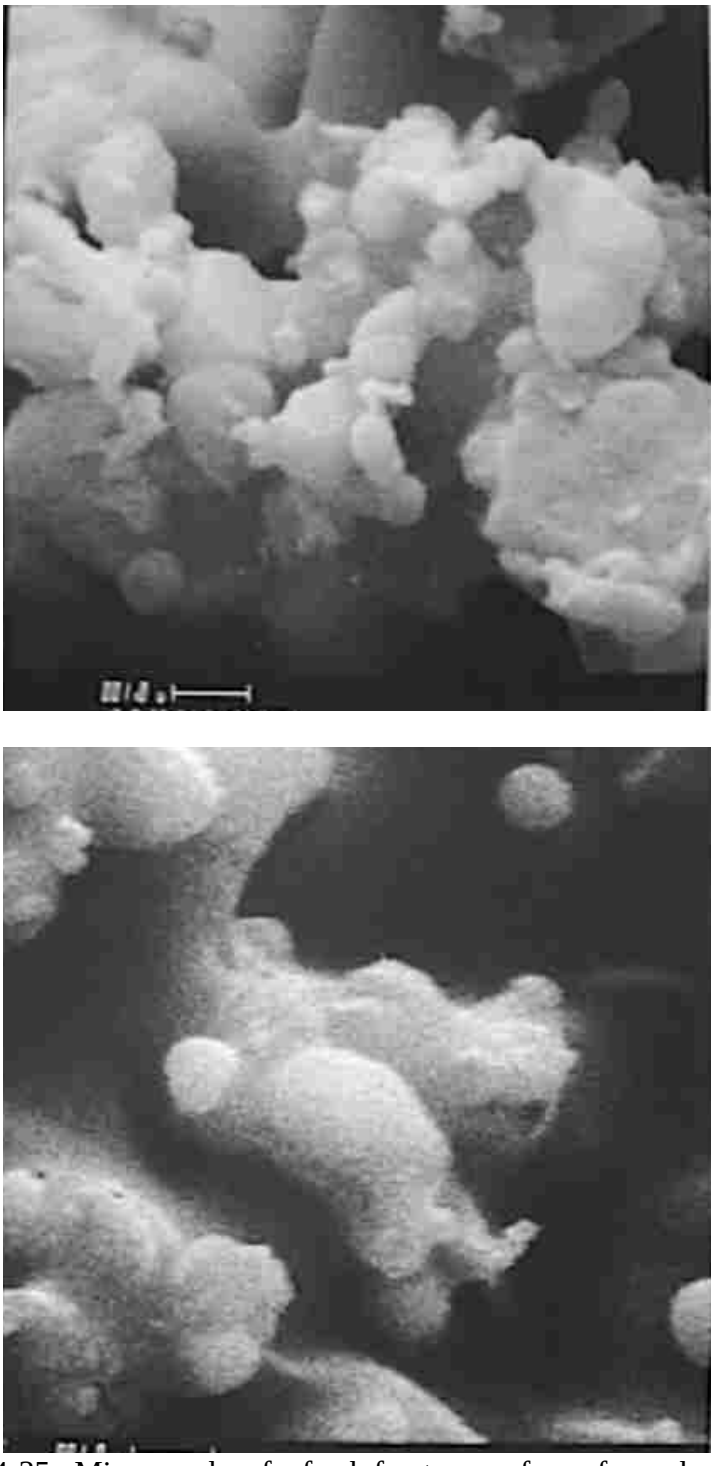

Figure 4-35. Micrographs of a fresh fracture surface of an ash agglomerate (ID # 4114) taken from an ash shed in the Tidd APF in October 1994.

4.3 KARHULA PRESSURIZED CIRCULATING FLUID BED FACILITY

The Foster Wheeler Pressurized-Circulating Fluid Bed (PCFB) test facility in Karhula, Finland was constructed and originally operated by Ahlstrom Boilers.[13] The 10 MWt (34.1 MMBtu/hr) facility has a fuel feeding capacity of 15,900 lb/hr, an operating temperature of 1615 °F, and an operating pressure of 16 bar. The barrier filter, which was designed by Siemens Westinghouse, operates without an upstream cyclone.[8] The filter vessel is closely coupled to the reactor vessel with the flue gas entering the filter vessel normal to the vessel wall (in contrast with the tangential inlet of the FL0301 filter vessel at the PSDF). This arrangement causes the flue gas to impinge directly on the shroud installed around the filter assembly. The filter consists of a single, three array cluster that holds up to 128 cylindrical filter elements. Inlet dust loadings have been as high as 13,000 ppm. Filter operation has been reliable, with only isolated episodes of ash bridging.[8] A number of coal and sorbent combinations have been evaluated at the facility. Some of the tests performed at Karhula have been to evaluate the coal and sorbent planned for the Lakeland PFBC.

Foster Wheeler Energia OY provided two batches of samples from the Siemens Westinghouse filter assembly for analyses under this task. (Analyses of additional samples received prior to this project are included in the interactive data bank.) The samples that were selected and analyzed, and are discussed in this section, are described in Table 4-12. Most of the results of the analyses of these four samples are presented in Tables 4-13 and 4-14. Sample # 4276 and sample # 4277 were collected from the filter vessel following tests conducted with eastern Kentucky coal and Gregg limestone during the last quarter of 1997. (Chemical analyses were also performed on size-segregated fractions derived from samples 4276 and 4277. The results of these analyses are included in Table 4-14.) Cumulative and differential size distribution data measured for samples 4182, 4276, and 4277 using various techniques are presented in Figures 4-36 through 4-39. Micrographs of ID # 4182 are presented in Figure 4-40. Micrographs of sample # 4277 are presented in Figure 4-41.

Table 4-12
Identification of Karhula Ash Samples Analyzed under this Task

ID #	Brief description
4182	filter cake ash with nodules from middle plenum (1996)
4184	hopper ash collected after test run (1996)
4276	hopper ash from silo after test run (1997)
4277	filter cake ash: top array (1997)

Table 4-13
Physical Characteristics of Karhula Ash Samples

quantity ID #	4182	4276	4277
specific surface area, m^2/g	1.2	1.6	2.2
D_{50}, µm (Microtrac Particle Size Analyzer)	--	31	12
D_{50}, µm (Shimadzu Sedigraph)	9.9	--	--
D_{50}, µm (Bahco Classifier)**	--	15	7.8
uncompacted bulk porosity, %	81	75	82
drag-equivalent diameter, µm	2.22	5.01	2.72
specific gas-flow resistance, in H_2O·min·ft/lb*	4.3	2.2	2.4
tensile strength, N/m^2	3.8	7.8	19
true particle density, g/cm^3	2.83	2.73	2.76
filter cake nodule porosity, %	75	--	--

* calculated for an assumed filter cake porosity equal to the uncompacted bulk porosity
** excludes particles > 25 µm from the analysis

Table 4-14
Chemical Composition of Karhula Ashes, % wt.

ID #	4182	4276	4276	4276	4277	4277
location	filter cake	hopper	hopper	hopper	filter cake	filter cake
particle size range	all	< 45 µm	> 45 µm	all	all	< 45 µm
Li_2O	0.01	0.02	0.02	0.02	0.02	0.02
Na_2O	0.87	0.70	0.52	0.64	0.61	0.78
K_2O	1.6	1.4	1.5	1.4	1.6	1.6
MgO	0.72	0.87	0.87	0.87	0.88	0.87
CaO	17.4	23.9	24.3	24.0	21.3	21.0
Fe_2O_3	11	8.1	6.2	7.5	8.1	8.4
Al_2O_3	12.6	16.8	16.0	16.5	16.9	17.1
SiO_2	34.4	32.0	35.4	33.1	31.5	31.7
TiO_2	0.6	1.3	0.83	1.1	1.2	1.2
P_2O_5	0.1	0.18	0.15	0.17	0.18	0.19
SO_3	19.8	13.1	14.2	13.5	15.7	15.9
LOI	0.22	0.74	0.70	0.73	0.62	0.62
soluble $SO_4^=$	23.8	16.7	16.0	16.5	19.6	19.4
Equilibrium pH*	7.4	--	--	--	10.18	--
silica ratio*	54	49	53	51	51	51
$R_{b/a}$*	0.66	0.70	0.64	0.68	0.66	0.65

* dimensionless

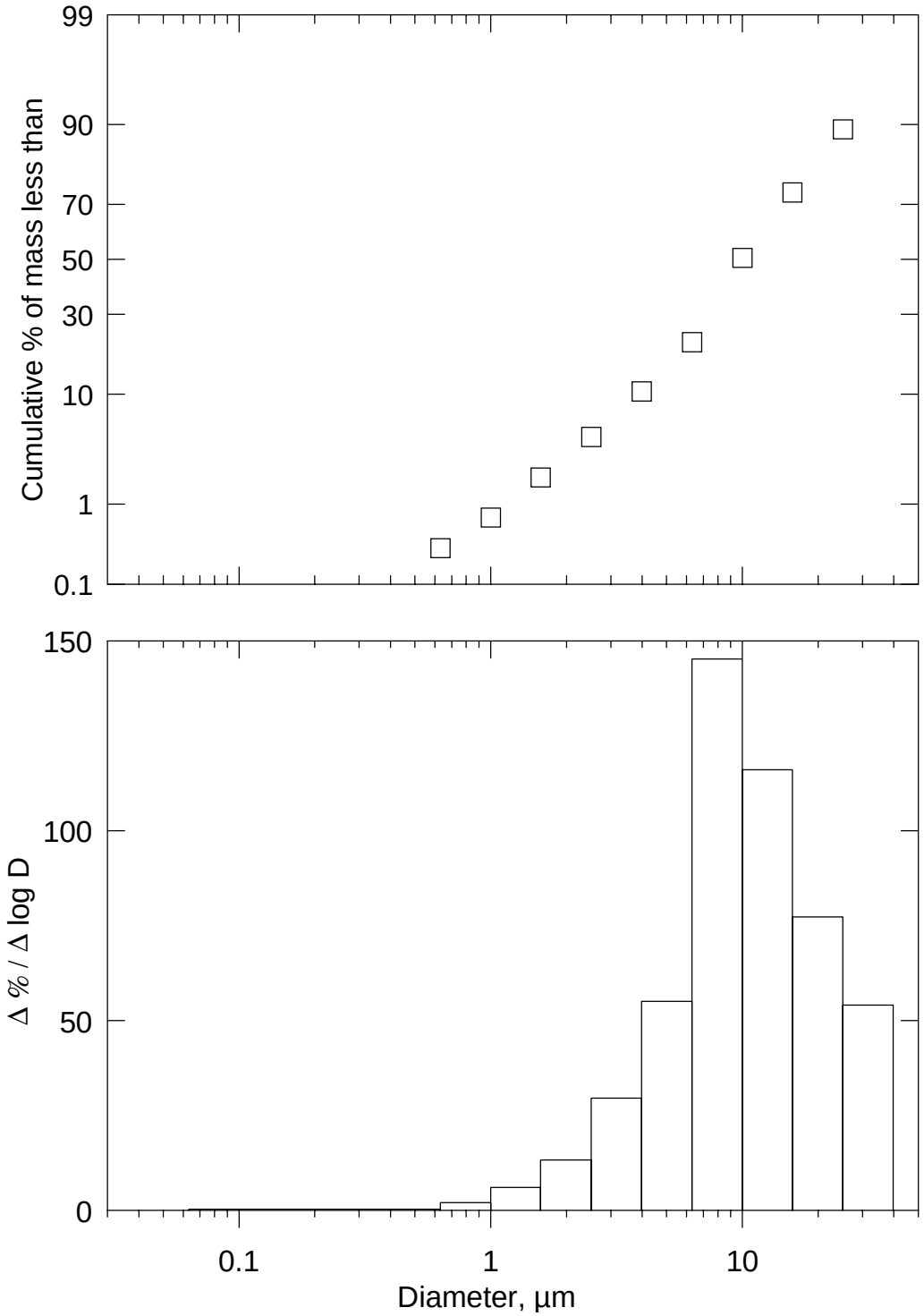

Figure 4-36. Cumulative and differential size distribution of Karhula filter cake ash (ID # 4182) measured with a sedigraph.

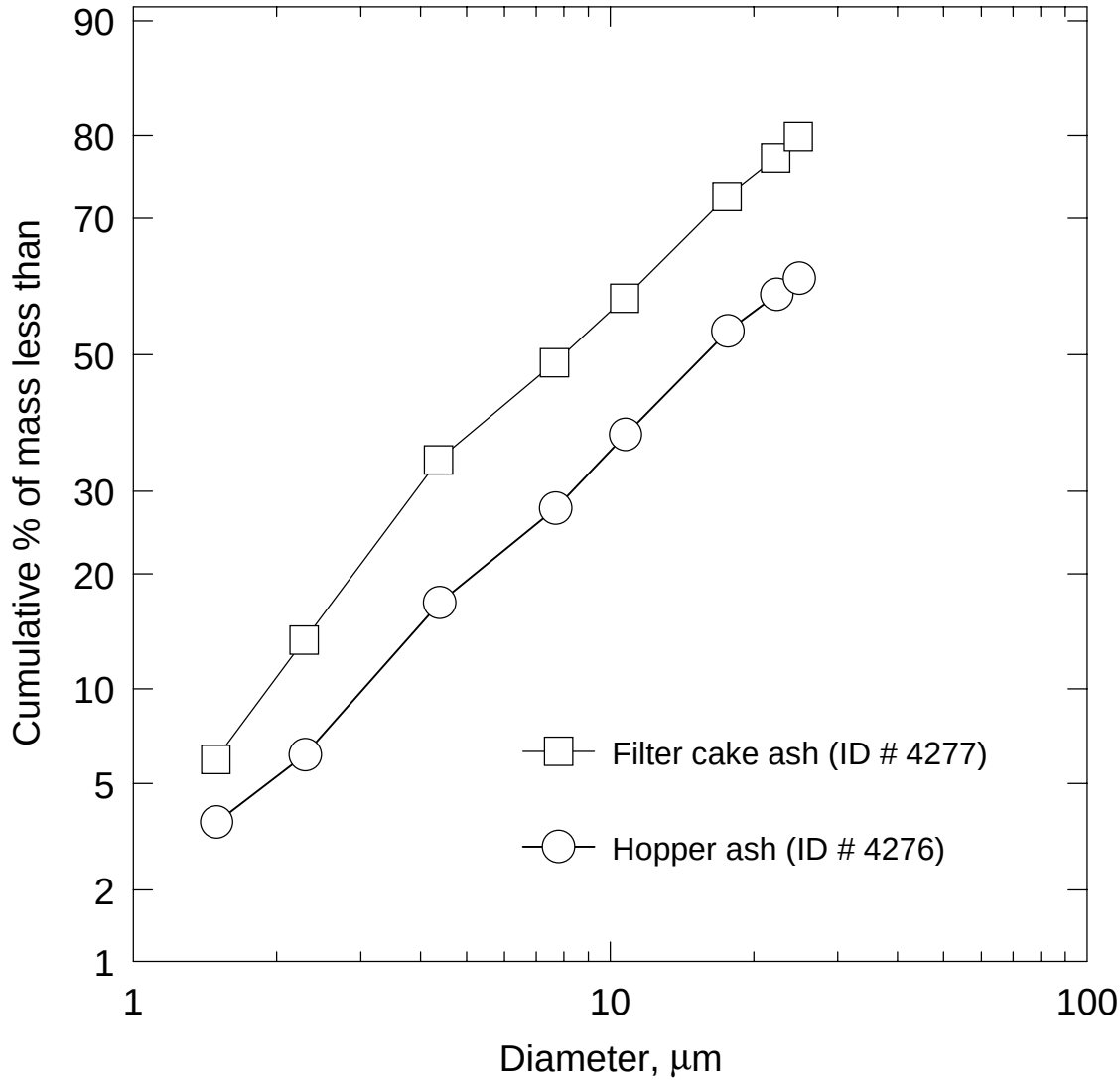

Figure 4-37. Cumulative size distributions of Karhula filter cake ash (ID # 4277) and hoppper ash (ID # 4276) measured with a Bahco aerodynamic classifier.

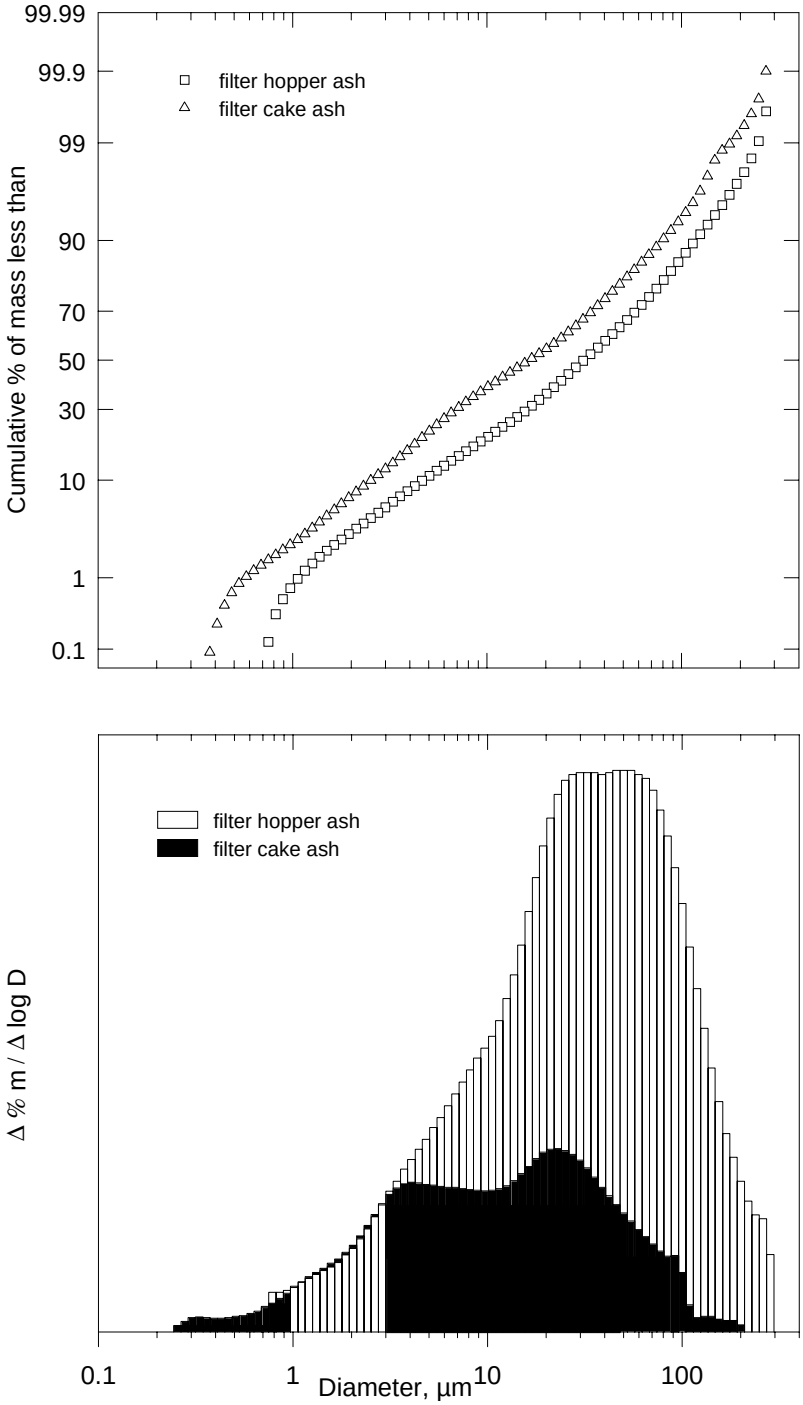

Figure 4-38. Cumulative and differential size distribution data measured for Karhula hopper ash (ID # 4276) and filter cake ash (ID # 4277) measured with a Leeds and Northrup Microtrac Particle Size Analyzer. The size distribution of the filter cake ash has been linearly scaled down by a factor of 0.36 to cause the shape of the finer portions of these two distributions to coincide as much as possible.

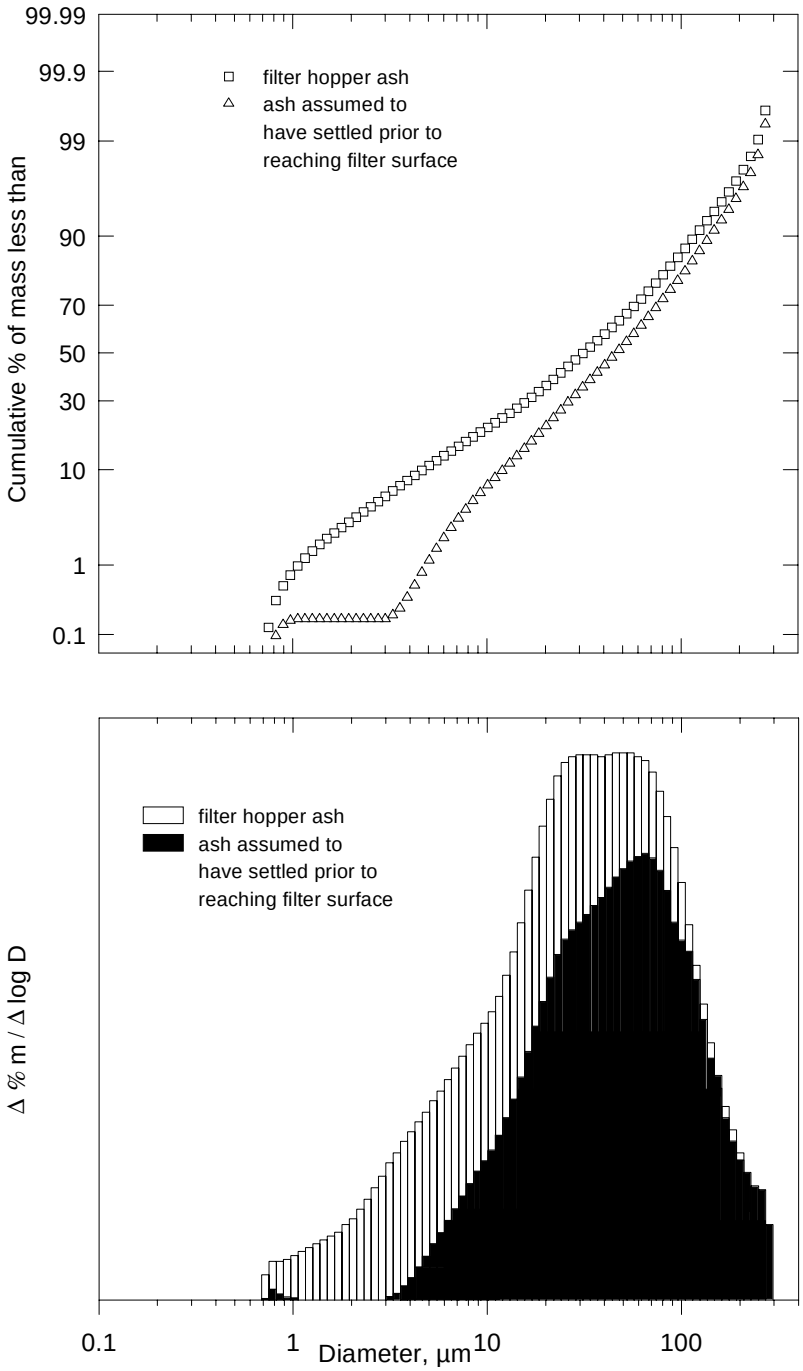

Figure 4-39. Cumulative and differential size distribution data measured for Karhula hopper ash (ID # 4276) measured with a Leeds and Northrop Microtrac Analyzer. The difference of the size distribution of the filter cake ash (ID # 4277) presented in Figure 4-38 has been subtracted from the size distribution of the hopper ash to display the size distribution of the particles assumed to have settled out in the hopper without having ever reached the filter cake surface.

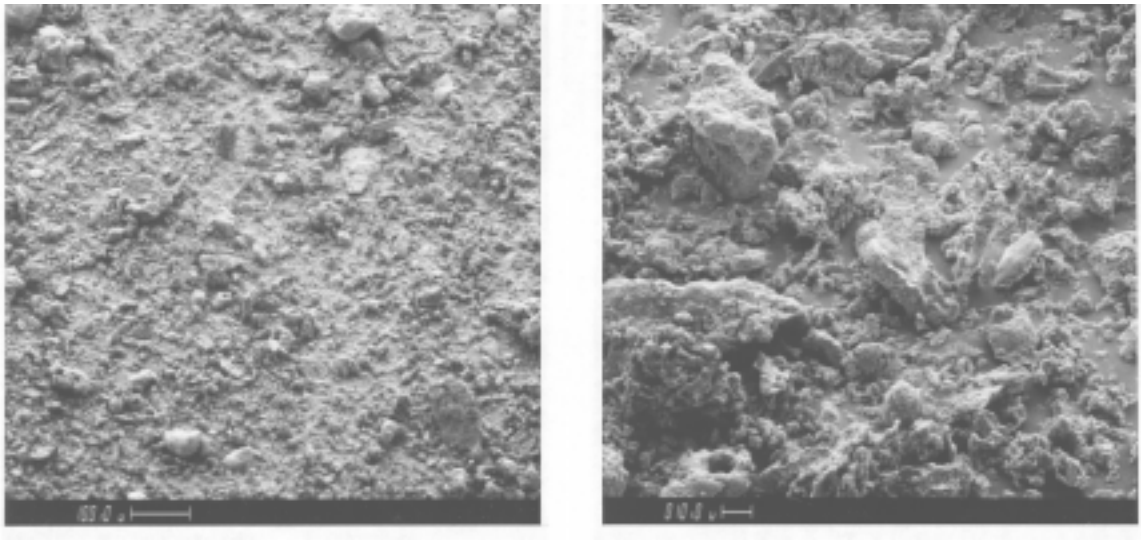

a b

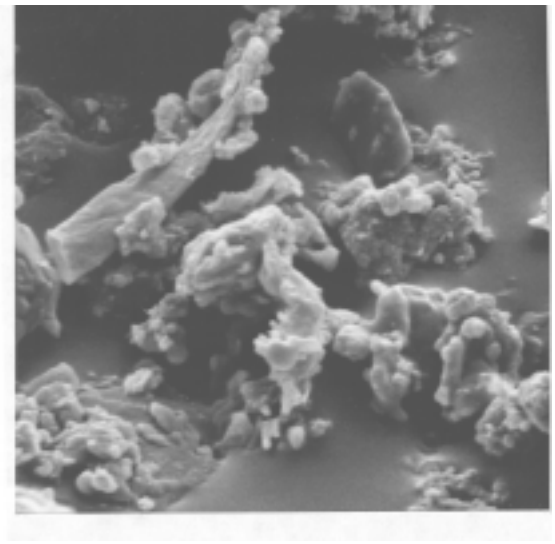

c

Figure 4-40. Micrographs of filter cake ash from the Karhula PCFB (ID # 4182) taken at a) 100X, b) 500X, and c) 5000X.

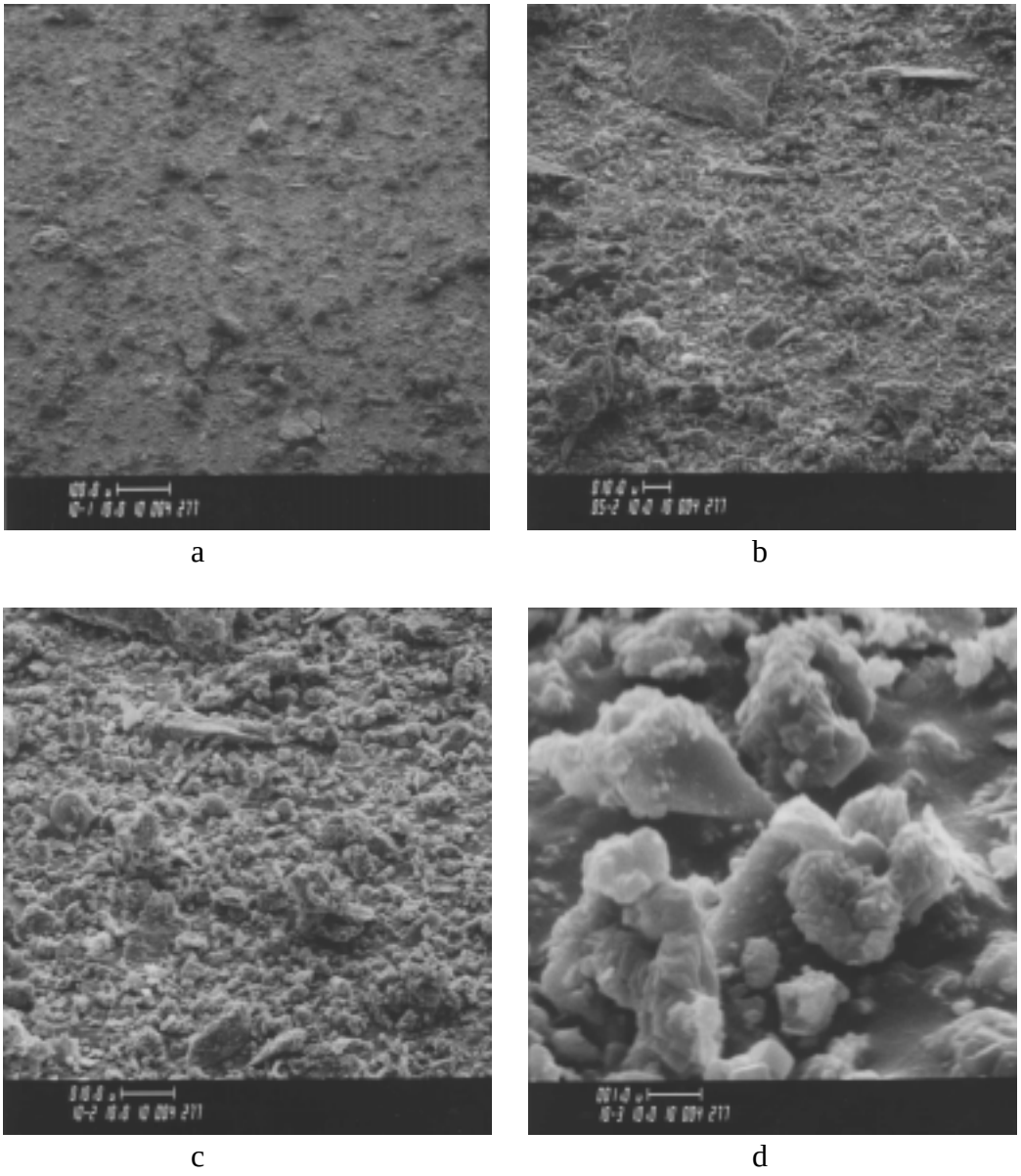

a b

c d

Figure 4-41. Micrographs of filter cake ash from the Karhula PCFB (ID # 4277) taken at a) 100X, b) 500X, c) 1000X, and d) 10,000X.

Because the Karhula samples that were provided included filter cake ashes and a corresponding hopper ash, analyses were performed to determine specific physical and chemical differences between samples obtained from these two locations. Measurements of size distribution, specific surface area, uncompacted bulk porosity, drag-equivalent diameter, and tensile strength (see Table 4-13) all indicate that these two ashes have significantly different physical characteristics. The hopper ash (ID # 4276) and the filter cake ash (ID # 4277) exhibited similar values of specific gas-flow resistance, despite their other physical differences. The reason for this similarity is the offsetting effect that filter cake porosity and specific surface area have on each other. Coarser particles, like those in the Karhula hopper sample, exhibit lower bulk cohesivity and would form filter cakes with lower porosities. In general, however, coarser particles also exhibit lower specific surface areas (as can be seen in Table 4-13). Pressure loss across a filter cake is incurred as the flue gas follows a tortuous path through the cake and past the surfaces of the particles. Because Karhula filter cake ash (ID # 4277) has more specific surface area than the corresponding hopper ash (ID # 4276), the beneficial effect of the greater porosity of the filter cake is offset by the higher specific surface area of the filter cake ash particles.

Two different techniques were used to measure the size distributions of these two ashes. The median diameters obtained with the Bahco Aerodynamic Classifier (Figure 4-37, Table 4-13) are significantly lower than the values measured with the Leeds and Northrup Microtrac Particle Size Analyzer (Table 4-13). These differences were caused by the sieving out of the coarser particles from the samples prior to classification with the Bahco device. (The Bahco device cannot accurately size particles larger than around 25 µm.) Although the Bahco data reflect the relative coarseness of these two samples, the data obtained with the Microtrac Analyzer (Figures 4-38 and 4-39) most accurately represent the size distribution of these samples because the Microtrac analyses were based on the entire spectrum of particle sizes in the samples.

As discussed under section *5.7 Estimating Filter Vessel Inertial Collection from Size Distribution Data*, measurements of particle size distribution can be used to estimate the extent to which the entrained ash particles entering the filter vessel at Karhula may have settled in to the hopper prior to ever reaching the filter cake surface. The degree to which the Karhula hopper ash contains large particles not found in the Karhula filter cake ash can be observed in the data presented in Figures 4-38 and 4-39. These data indicate that around 64 % of the material entering the filter vessel at Karhula settled into the hopper without reaching the surface of the filter cake.

One of the methods developed for measuring the overall pore volume of a nodule was used to characterize the nodule fragments in sample # 4182. On-site experience at the Tidd PFBC has shown that the porosity of the most recently deposited portions of filter cake maybe significantly greater than the porosity of older portions of the cake. It is very likely that during the shipment of the filter cake ash and nodule samples from Karhula, the fluffiest, most recently deposited parts of the cake were shaken or rubbed off of the cake nodules. Therefore, the reported filter cake porosity value of 75 % included in Table 4-13 should represent a lower bound for the actual overall filter cake porosity in late 1996.

Analyses were also performed to determine the extent to which the physical segregation of particles discussed above affected the chemical composition of the hopper and filter cake ashes (Table 4-14). In general, the chemical composition of the hopper and filter cake ashes are basically independent of particle size. The chemical species in the hopper ash that most deviate from this trend are Na, Fe, Ti, and P, which are enriched in the finer ash particles, and Si, which is enriched in the coarser ash particles. For the filter cake ash, the only chemical species found to be size dependent was Na, which, like the hopper ash, was enriched in the finer particles. In a comparison of the chemistry of the hopper and filter cake ashes, the main difference was in their sulfur contents. Sulfur was slightly enriched in the filter cake ash relative to the hopper ash, most likely by the additional scrubbing of SO_2 from the flue gas by unreacted sorbent in the filter cake.

By comparing the relative concentrations of sulfate ions in hopper ashes (# 4184 and # 4276) and in filter cake ashes (# 4182 and # 4277), the Karhula ash samples generated in 1996 and 1997 allow evaluation of the relative degrees to which these two types of ash samples become sulfated. (The measurement of sulfate ions for sample # 4182 was performed on ash obtained from consolidated nodules contained in the sample. Nodules from the filter cake sample were chosen for this analysis to accentuate any differences between the degree of sulfation of hopper and filter cake ashes.) The concentration of soluble sulfate in the hopper ash from 1996 (ID # 4184) was measured to be 25.6 % by weight, which is somewhat greater than the soluble sulfate concentration (21.6 % by wt.) in a filter cake nodule from ID # 4182. (These results are not listed in Table 4-14.) For the samples from 1997, the soluble sulfate content of the filter cake ash (19.6 % wt.) was somewhat greater than that of the hopper ash (16.5 % wt.). The significance of these results is discussed in section *5.8 Consolidation and Bridging of PFBC Ash Deposits in HGCU Filters*, found later in this report.

The silica ratio and $R_{b/a}$ values presented for the Karhula ashes in Table 4-14 indicate that these ashes could be interpreted as having a high probability of slagging (silica ratio < 65; $R_{b/a} > 0.5$) if present in a PC boiler.[12] (These quantities are defined in section *4.1 Laboratory Methods used to Characterize Samples*.) However, the slagging propensity indicated by these quantities for these Karhula ashes is less than that of the Tidd ashes. The fact that ash bridging and the formation of strong ash deposits were not nearly as severe at Karhula as at Tidd tends to support the use of these quantities as a means of predicting the development of high-strength PFBC ash deposits in HGCU filters.

4.4 DOE/FETC MODULAR GAS CLEANUP RIG

The three gasification particulate samples from the DOE/FETC-MGN MGCR identified in Table 4-15 were characterized in the laboratory. Sample # 4198 was collected from the MGCR hopper by DOE/FETC-MGN personnel following the run of the Fluidized Bed Gasifier that ended in October, 1996. This sample was taken to correspond to the filter cakes that were observed on the site visit conducted on October 29, 1996. The physical and chemical characteristics measured for these samples are presented in Tables 4-16 and 4-17. Micrographs of samples 4170 and 4198 are presented in Figures 4-42 and 4-43. All three samples have very fine size distributions (Figures 4-44 through 4-46), high specific surface areas and uncompacted bulk porosities, and very low values of drag-equivalent diameter.

Table 4-15
Identification of DOE/FETC-MGN MGCR Gasification Particulate Samples

ID #	Brief description
4170	air blown FBG hopper run 95-MGC-12 (9/95)
4198	air blown FBG hopper run 96/14 (10/96)
4259	air blown FBG hopper run 94-MGC-10 (1994)

Table 4-16
Physical Characteristics of DOE/FETC MGCR Gasification Particulate Samples

quantity ID #	4170	4198	4259
specific surface area, m^2/g	140	615	195
Stokes' MMD, μm	0.74	0.76	0.29
uncompacted bulk porosity, %	97	97	98
drag-equivalent diameter, μm	0.08	0.12	0.08
specific gas-flow resistance, in $H_2O \cdot min \cdot ft/lb$*	18	9.0	9.0
true particle density, g/cm^3	2.87	2.66	2.66

* calculated for filter cake porosities equal to the uncompacted bulk porosity of the sample

Table 4-17
Chemical Characteristics of DOE/FETC MGCR Gasification Particulate Samples, % wt.

Constituent ID #	4170	4198
Li_2O	0.02	0.02
Na_2O	0.59	0.62
K_2O	0.07	0.15
MgO	10.9	8.7
CaO	33.3	24.8
Fe_2O_3	1.17	2.5
Al_2O_3	17.4	18.4
SiO_2	31.8	39.3
TiO_2	1.49	1.7
P_2O_5	0.53	0.59
SO_3	0.32	0.58
LOI	35.9	32.0
soluble $SO_4^{=}$	< 0.2	< 0.37
Equilibrium pH*	10.2	9.3

* dimensionless

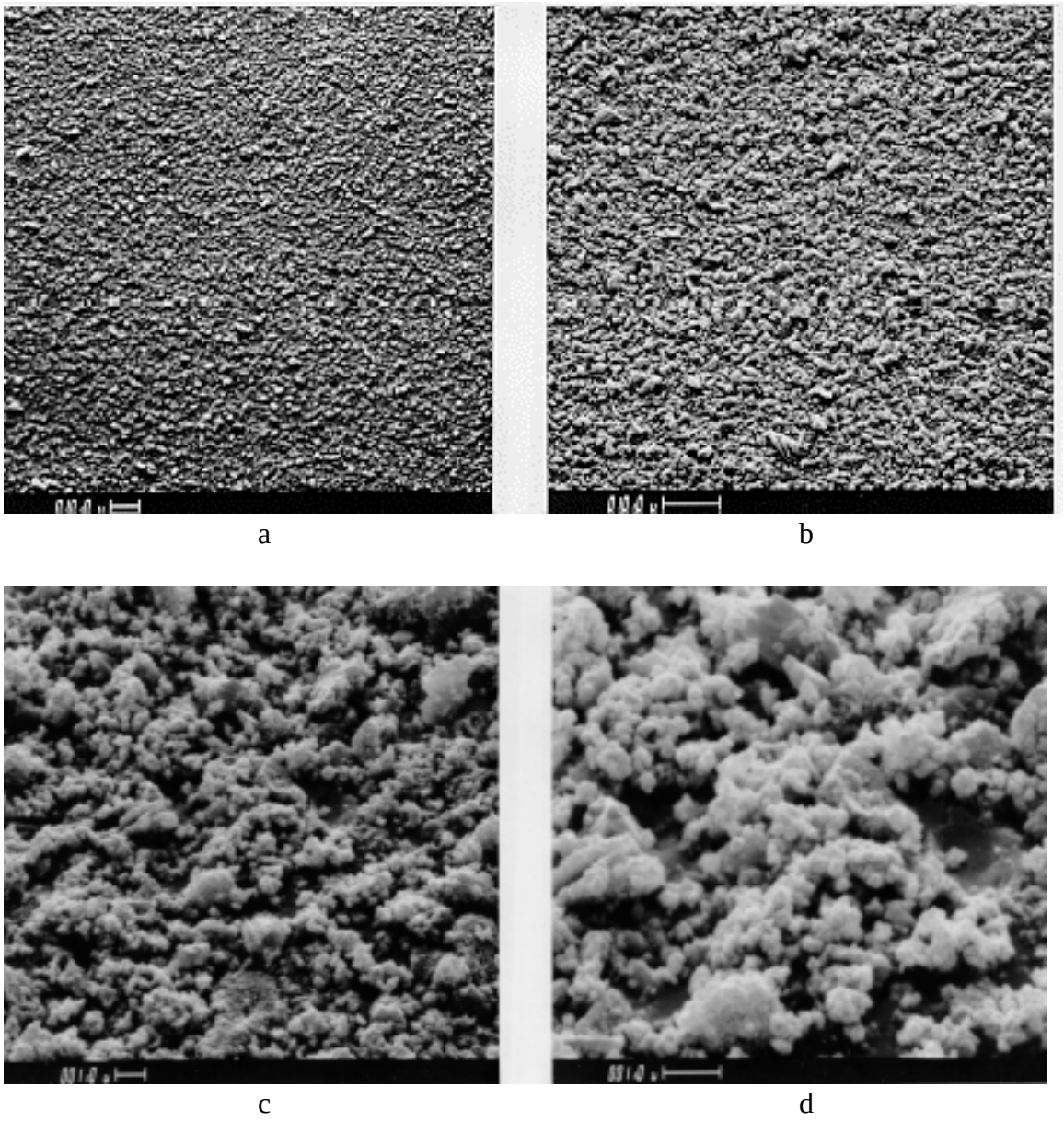

a b

c d

Figure 4-42. Representative micrographs of DOE/FETC MGCR gasifier char (ID # 4170) taken at a) 500X, b) 1000X, c) 5000X, and d) 10,000X.

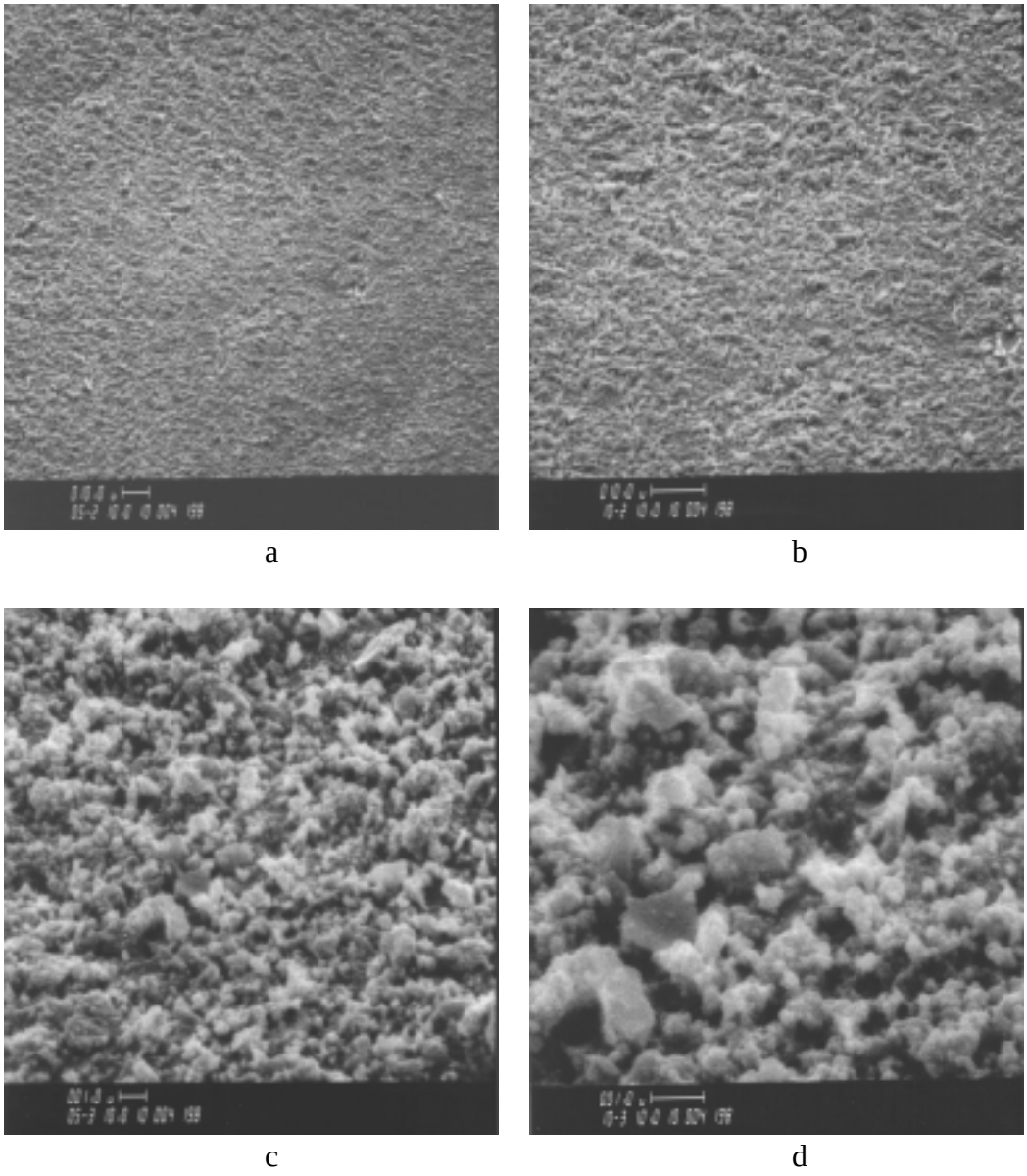

Figure 4-43. Representative micrographs of DOE/FETC MGCR gasification char (ID # 4198) taken at a) 500X, a) 1000X, c) 5000X and d) 10,000X.

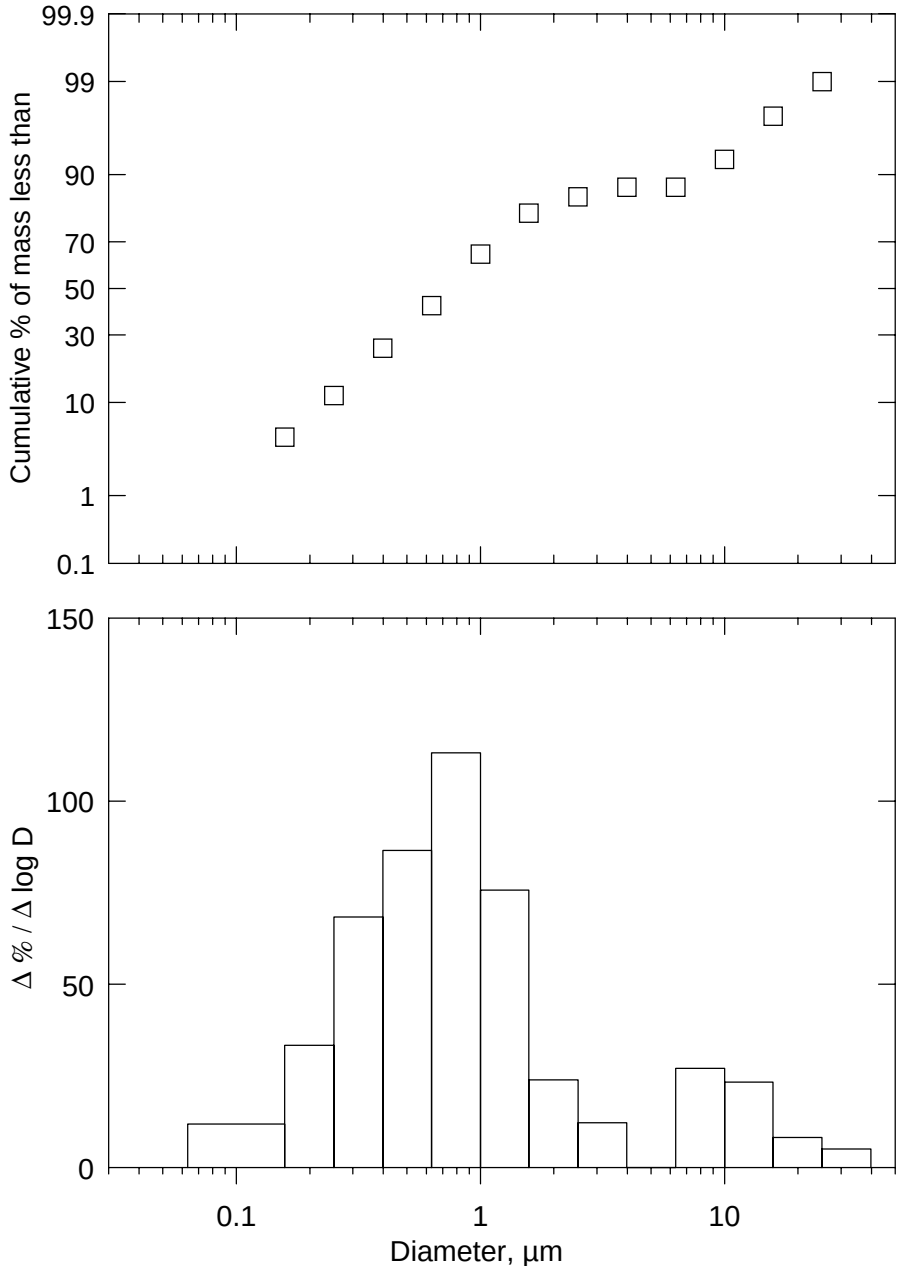

Figure 4-44. Cumulative and differential size distribution data measured for ash from the DOE/FETC gasifier (ID # 4170) measured with a Shimadzu SA-CP4 Centrifugal Particle Size Analyzer. The MMD of this distribution is 0.74 µm, and its geometric standard deviation is 2.8 µm. (This size distribution data includes the assumption that the ash contains no particles smaller than 0.063 µm.)

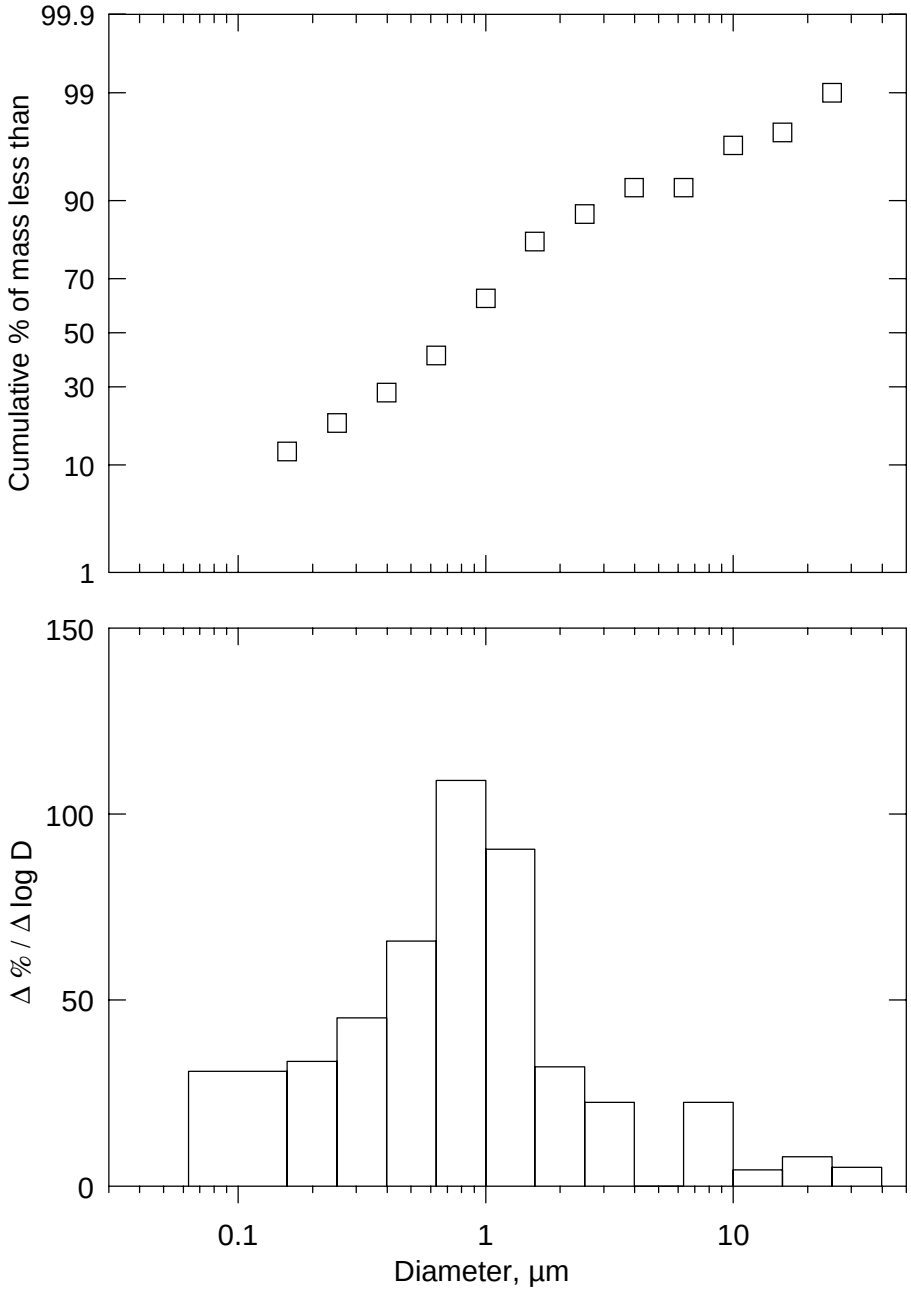

Figure 4-45. Cumulative and differential size distribution data measured for DOE/FETC-MGN MGCR gasification particulate (ID # 4198) measured with a Shimadzu SA-CP4 Centrifugal Particle Size Analyzer. The MMD of this distribution, which appears to be bimodal, is 0.76 µm, and its geometric standard deviation is 3.1. (This size distribution data includes the assumption that the sample contains no particles smaller than 0.063 µm.)

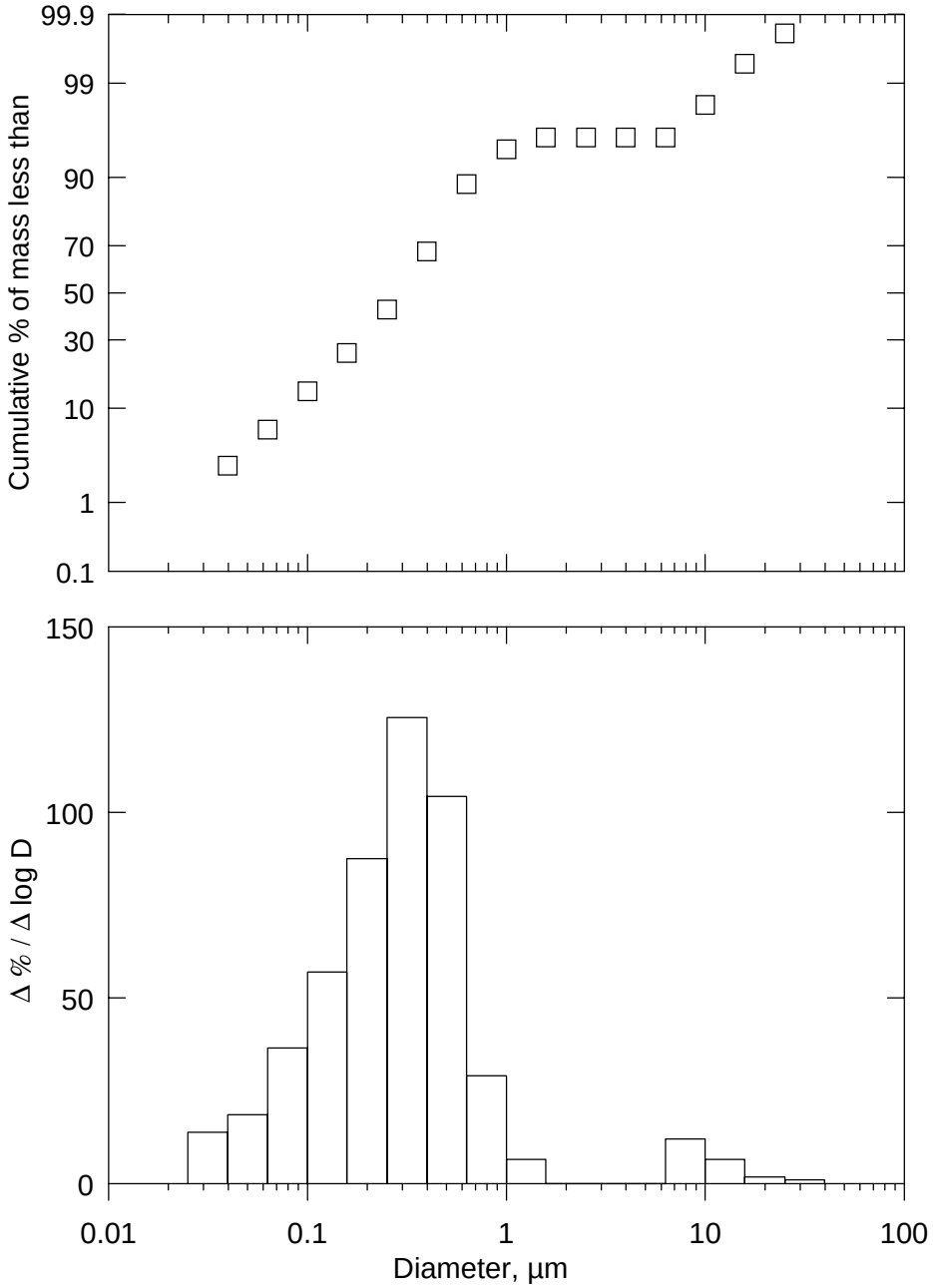

Figure 4-46. Cumulative and differential size distribution data measured for DOE/FETC-MGN MGCR gasification particulate (ID # 4259) measured with a Shimadzu SA-CP4 Centrifugal Particle Size Analyzer. The MMD of this distribution, which appears to be bimodal, is 0.29 µm, and its geometric standard deviation is 2.3. (This size distribution data includes the assumption that the sample contains no particles smaller than 0.063 µm.)

When the DOE/FETC MGCR samples were examined with a scanning electron microscope (Figures 4-42 and 4-43), the fineness of their particle size distributions was readily apparent. Like other gasification char samples characterized under this task, samples # 4170 and # 4198 have high values of loss-on-ignition (LOI).

Several differences were identified between sample # 4198 and the other two samples listed in Table 4-15. The most striking difference was in the value of specific surface area. ID # 4198 has several times the surface area as either of the other two MGCR samples. This difference was observed although the MMD of sample # 4198 is essentially equivalent to that of sample # 4170, and coarser than the MMD of sample # 4259. Because the drag-equivalent diameter of sample # 4198 is somewhat greater than that of the other two samples, the increased surface area of sample # 4198 is probably attributable to ultrafine pores that are too small to affect flow resistance.

In general, the physical characteristics of sample # 4259 are similar to those of sample # 4170 and # 4198. The most significant difference is that the median particle size of the sample from 1994 (ID # 4259) is 0.29 µm, even smaller than the extremely fine values measured for the other two MGCR samples. However, sample # 4259 has a measured specific surface area value between the values measured for sample # 4170 and sample # 4198, and a drag-equivalent diameter that is no finer than either sample # 4170 or sample # 4198. The absence of positive correlations between additional specific surface area or drag-equivalent diameter and decreased median diameter is attributable to the irregular particle shapes and the ultrafine size distributions of all three of these samples. When particles have extremely irregular shapes, the predominant factor controlling the relationship between particle size distribution and specific surface area is the degree of irregularity in the shape of the particles, rather than their size. The extremely high surface areas of these samples, even when their size distribution is taken into account, indicate that the MGCR char particles have very irregular, rough surfaces.

Although the values of specific gas-flow resistance shown in Table 4-16 are not extremely high, they are calculated for filter cake porosities equal to the uncompacted bulk porosities of the samples. As demonstrated below, and mentioned elsewhere in this report, any reductions in these filter cake porosities will substantially increase these values of specific gas-flow resistance. In Figure 4-47 the permeability model has been used to plot the characteristic permeability of sample # 4170 as a function of filter cake porosity. These data indicate that the degree of filter cake consolidation that may be induced by normal filtering pressure drops of around 3 to 4 psi may increase filtering pressure losses by a factor of twenty or more. (If a filter cake composed of these fine particles is allowed to compact to around 90 % porosity, specific gas flow resistances around 400 in $H_2O \cdot min \cdot ft/lb$ could be expected.) This is especially detrimental since the specific gas-flow resistance of this sample (and also the other two samples listed in Table 4-15) is relatively high even when the filter cake is uncompacted. These characteristics can ultimately lead to high pressure losses and/or very frequent cleaning.

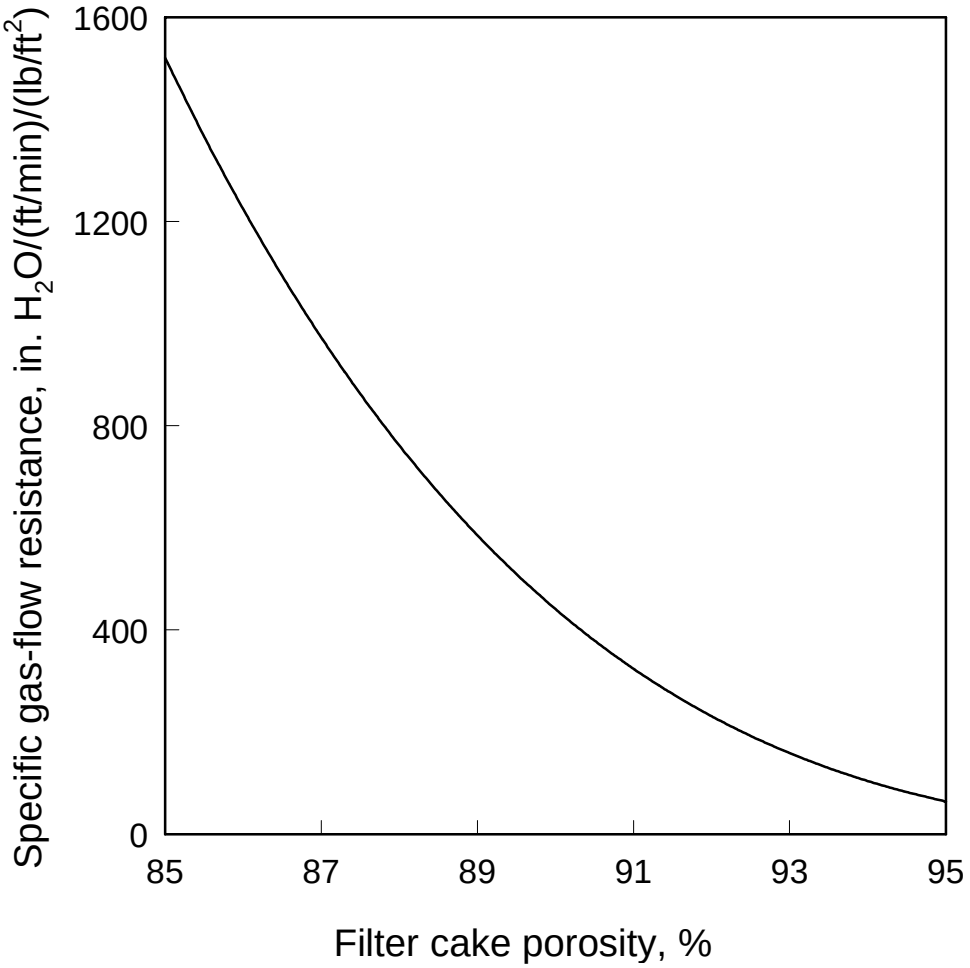

Figure 4-47. Data calculated with the permeability model for the DOE/FETC MGCR gasification char (ID # 4170) showing the strong dependence of specific gas-flow resistance on filter cake porosity.

During a visit to FETC in late 1995, there was an opportunity to examine the filter cake that remained on the candles used during the run performed at the DOE/FETC Advanced Gasification and Hot Gas Cleanup Facility in October 1995. This filter cake should correspond to sample # 4170. Although the cake remaining on the candle surface was patchy and thin, it was possible to make a rough measurement of its porosity. The value obtained (86 %) must be interpreted as a lower bound for the actual porosity of the filter cake during operation, because handling and storage of the used candles appeared to have possibly compressed much of the cake on the candles after they were removed from the filter vessel. Based on the calculations presented in Figure 4-47, a filter cake porosity of 86 % would probably present severe pressure drop penalties for this gasifier residue.

As discussed in the section of this report describing the site visit in October 1996 to the DOE/FETC MGCR, measurements of the porosity of MGCR filter cakes gave values from 91 to 95 %. Even this magnitude of reduction in filter cake porosity below uncompacted bulk porosity values causes a large increase in gas-flow resistance. (Data presented later in this

report for Piñon Pine filter cake char material indicate that the filter cakes formed at that facility apparently have compacted, probably as a result of the filtering pressure drop across the cake.)

The response of sample ID # 4170 to mechanically applied compacting forces was also determined in the laboratory. The compaction data shown in Figure 4-48, which were measured at room temperature, show that a filtering pressure drop of 3.4 psi (94 in. H_2O) may be sufficient to reduce the porosity of a filter cake formed from this sample down to about 90 %. Although the sample # 4170 showed an apparent increase in strength as it was compacted, the cake compacted with a pressure of 3.4 psi still had comparatively low strength.

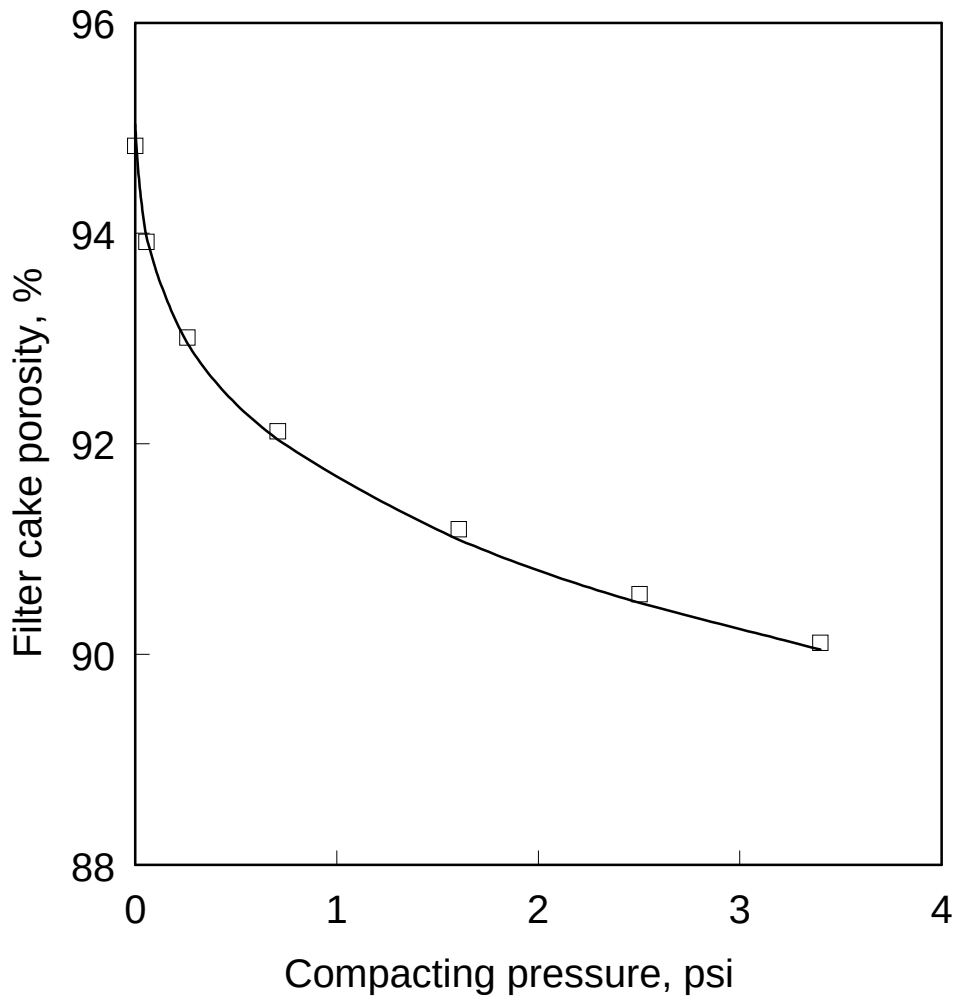

Figure 4-48. Response of sample ID # 4170 to mechanically applied compacting forces.

4.5 POWER SYSTEMS DEVELOPMENT FACILITY

The PSDF ash samples analyzed and discussed in this section are identified in Table 4-18. These samples were collected during site visits to the facility. (The hopper ash listed below, ID # 4295, was provided for analysis by PSDF personnel.) Because the PSDF ran under a variety of process conditions as these ashes were generated, conclusions based on direct comparisons of samples collected on different sampling dates must be carefully interpreted.

Table 4-18
Identification of PSDF Ash Samples Analyzed and Discussed in this Section

ID #	date sample obtained	location / description
4231	4/9/97	filter cake
4232	7/29/97	bottom plenum filter cake
4233	7/29/97	top plenum filter cake
4239	7/29/97	filter cake (upper region of outer candle)
4245	7/29/97	filter cake (upper region of inner candle)
4257	7/29/97	cleanable filter cake with nodules
4258	7/29/97	cleanable filter cake with nodules
4262	11/5/97	bottom plenum filter cake
4294	1/20/98	bottom plenum filter cake
4295	12/8/97	filter hopper
4303	5/18/98	bottom plenum filter cake
4347	1/26/99	top plenum filter cake
4348	1/26/99	top plenum filter cake

The majority of the results of physical analyses performed on these samples are summarized in Table 4-19. The average filter cake porosity values measured during PSDF site visits are summarized in Table 4-20. (These porosity values are used to calculate some of the specific gas-flow resistance values shown in Table 4-19.) The results of chemical analyses performed on these samples are presented in Table 4-21.

Table 4-19
Physical Characteristics of PSDF Ash Samples

sampling date	4/97	4/97	7/97	7/97	11/97	1/98	12/97	5/98	1/99
quantity ID #	4231	4232	4233	4258	4262	4294	4295	4303	4347
specific surface area, m^2/g	3.80	2.9	--	5.0	5.3	--	--	--	3.8
Stokes' MMD, µm	4.7	9.9	8.1	4.6	3.8	8.6	18	--	14.7
uncompacted bulk porosity, %	85	75	82	--	87	84	77	78	82
drag-equivalent diameter, µm	2.05	4.79	3.04	--	1.49	2.31	3.47	3.59	2.21
specific gas flow resistance, in H_2O·min·ft/lb*	2.6	2.2	1.9	--	2.9	2.6	3.7	2.9	3.6
specific gas flow resistance, in H_2O·min·ft/lb**	--	--	1.0	--	--	9.7	--	2.5	6.5
tensile strength, N/m^2	--	--	--	--	> 16	--	--	--	--
true particle density, g/cm^3	2.61	2.90	2.92	--	2.78	2.50	--	2.55	2.62

* calculated for an assumed filter cake porosity equal to the uncompacted bulk porosity
** calculated for an filter cake porosity measured on the same sampling date (see Table 4-20)

Table 4-20
Average Filter Cake Porosity Values Measured during PSDF Site Visits

date of site visit	average filter cake porosity, %
April 9, 1997	could not be determined
July 29, 1997	85
November 5, 1997	could not be determined
January 20, 1998	76
May 18, 1998	79
January 26, 1999	79

Table 4-21
Chemical Composition of PSDF Ashes, % wt.

ID # location date	4231 filter cake 4/9/97	4262 filter cake 11/5/97	4294 filter cake 1/20/98	4295 hopper 12/8/97	4347 filter cake 1/26/99	4348 filter cake 1/26/99
Li_2O	0.027	--	0.054	0.036	0.08	0.08
Na_2O	0.52	0.06	0.110	0.088	0.27	0.27
K_2O	1.73	1.76	0.695	0.844	1.9	2
MgO	2.12	8.00	4.49	8.08	2.6	2.2
CaO	4.49	9.98	5.91	9.05	12.2	11.1
Fe_2O_3	5.10	4.78	3.47	2.69	5.6	5.6
Al_2O_3	21.89	21.93	11.1	6.82	19.4	20.7
SiO_2	57.25	43.37	39.6	38.5	42.2	42.8
TiO_2	1.15	1.13	1.07	0.944	1	1.2
P_2O_5	0.32	0.51	0.303	0.307	0.42	0.42
SO_3	2.53	6.34	11.9	9.86	10.7	10.6
SrO	--	0.19	--	--	--	--
BaO	--	0.09	--	--	--	--
LOI	7.80	1.94	5.82	0.812	1.4	1.1
soluble $SO_4^=$	--	11.6	11.3	9.8	12.90	12.80
Equilibrium pH*	--	7.3	--	--	--	--
silica ratio*	83	66	74	66	67	69
$R_{b/a}$*	0.17	0.37	0.28	0.45	0.36	0.33

* dimensionless

Size distribution measurements were performed on ashes collected in July, 1997 to determine if filter cakes formed in different places in the plenum assemblies comprised significantly different particle size distributions. These measurements compared the particle size distribution of filter cake ash from the upper region of a candle from the outer ring of candles in the top plenum (ID # 4239) with the particle size distribution of filter cake ash from the upper region of a candle from one of the innermost candles in the bottom plenum (ID # 4245). The size distribution data measured for these two samples (see Figures 4-49 and 4-50) do not demonstrate any significant stratification of particle sizes throughout the filter cakes formed at various locations in the filter vessel. Additional size distribution measurements of PSDF filter cake ashes (ID #'s 4231, 4232, 4233, 4258, and 4262) are presented in Figures 4-51 through 4-55.

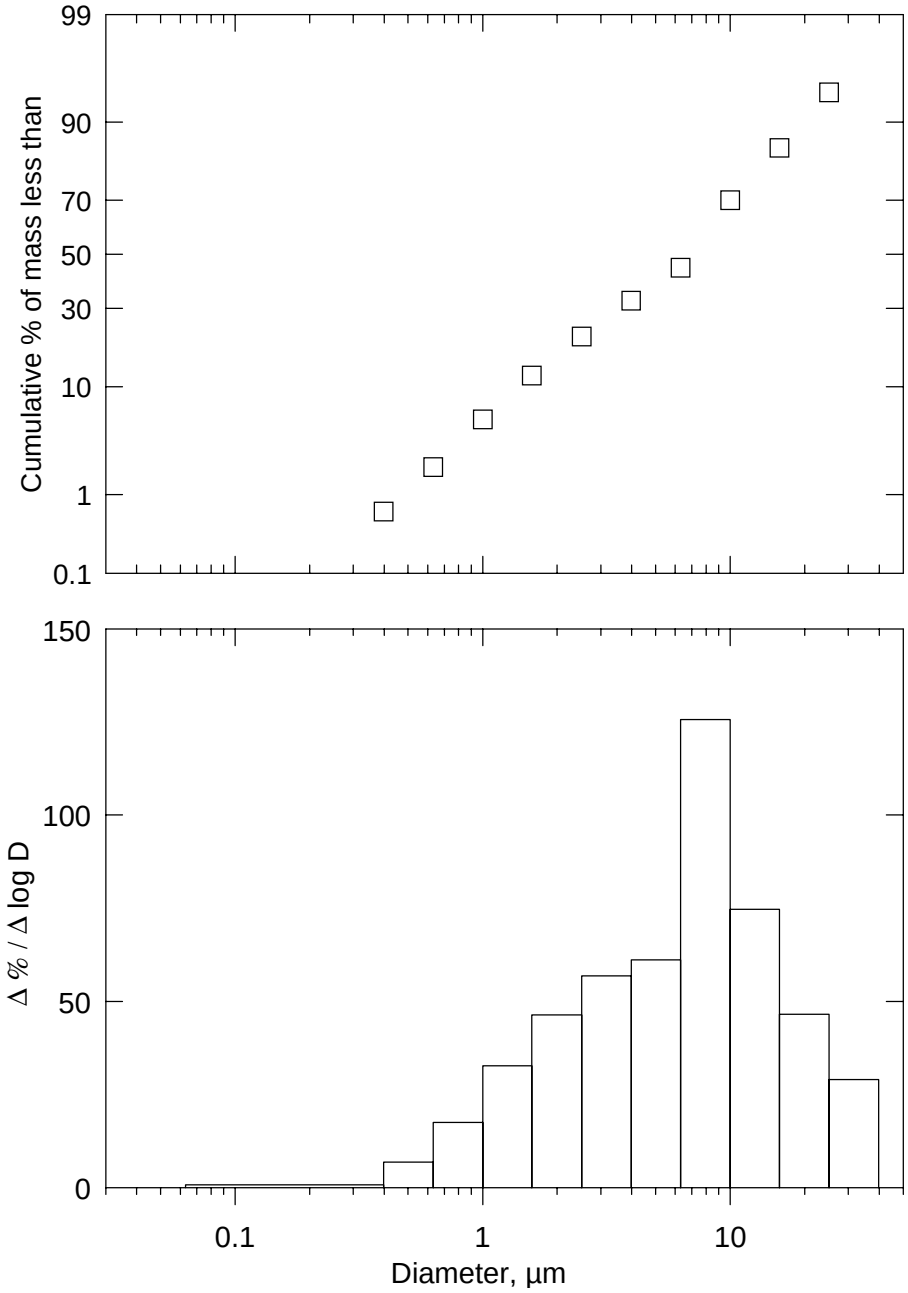

Figure 4-49. Cumulative and differential size distribution data measured for PSDF filter cake ash (ID # 4239) measured with a Shimadzu SA-CP4 Centrifugal Particle Size Analyzer. The MMD of this distribution is 6.9 µm, and its geometric standard deviation is 2.8. The D_{16} of this distribution is 1.9 µm, and its D_{84} is 15 µm. (This size distribution data includes the assumption that the sample contains no particles smaller than 0.063 µm.)

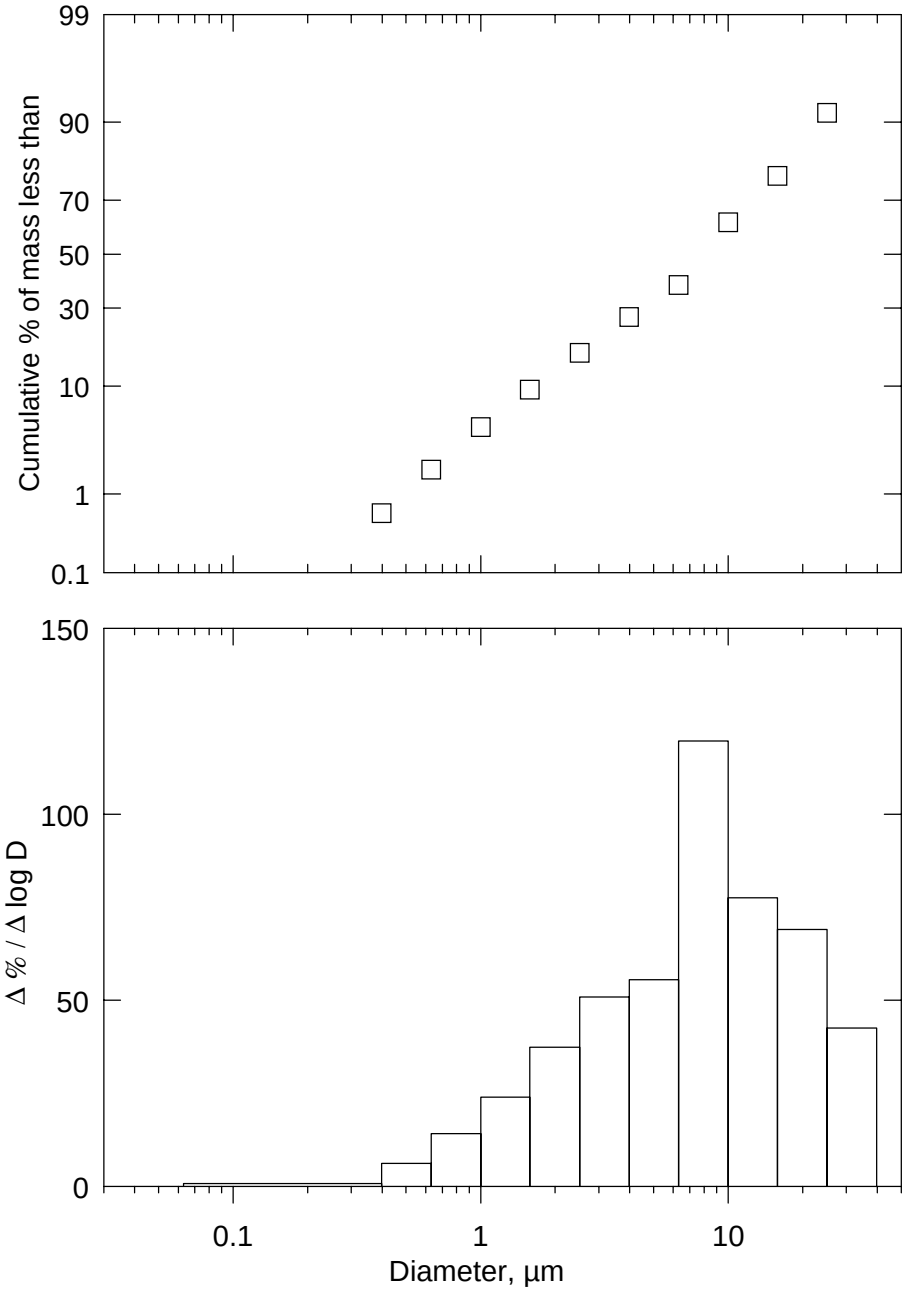

Figure 4-50. Cumulative and differential size distribution data measured for PSDF filter cake ash (ID # 4245) measured with a Shimadzu SA-CP4 Centrifugal Particle Size Analyzer. The MMD of this distribution is 7.9 µm, and its geometric standard deviation is 2.9. The D_{16} of this distribution is 2.4 µm, and its D_{84} is 20 µm. (This size distribution data includes the assumption that the sample contains no particles smaller than 0.063 µm.)

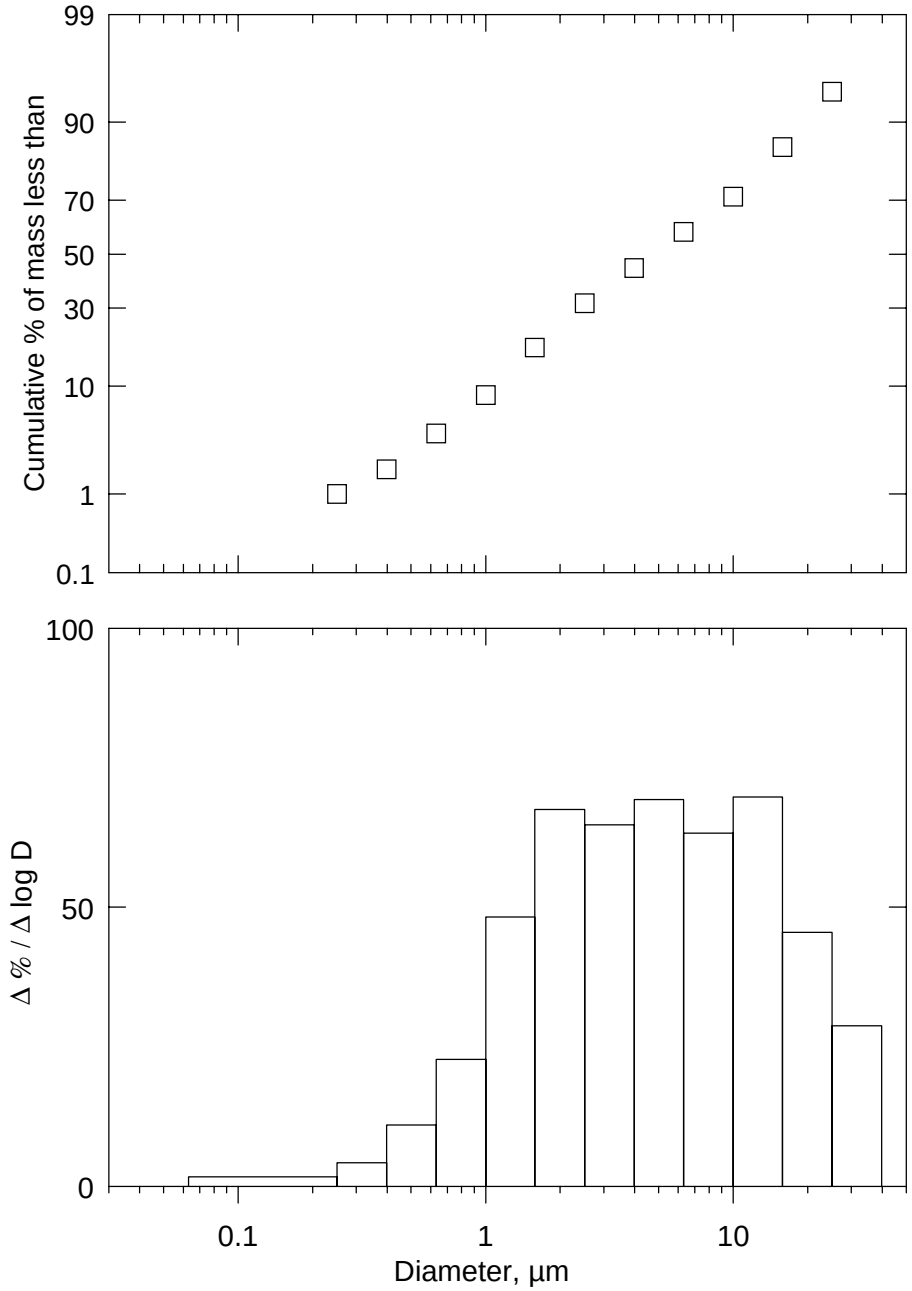

Figure 4-51. Cumulative and differential size distribution data measured for PSDF filter cake ash (ID # 4231) measured with a Shimadzu SA-CP4 Centrifugal Particle Size Analyzer. The MMD of this distribution is 4.7 µm, and its geometric standard deviation is 3.3. The D_{16} of this distribution is 1.4 µm, and its D_{84} is 15 µm. (This size distribution data includes the assumption that the sample contains no particles smaller than 0.063 µm.)

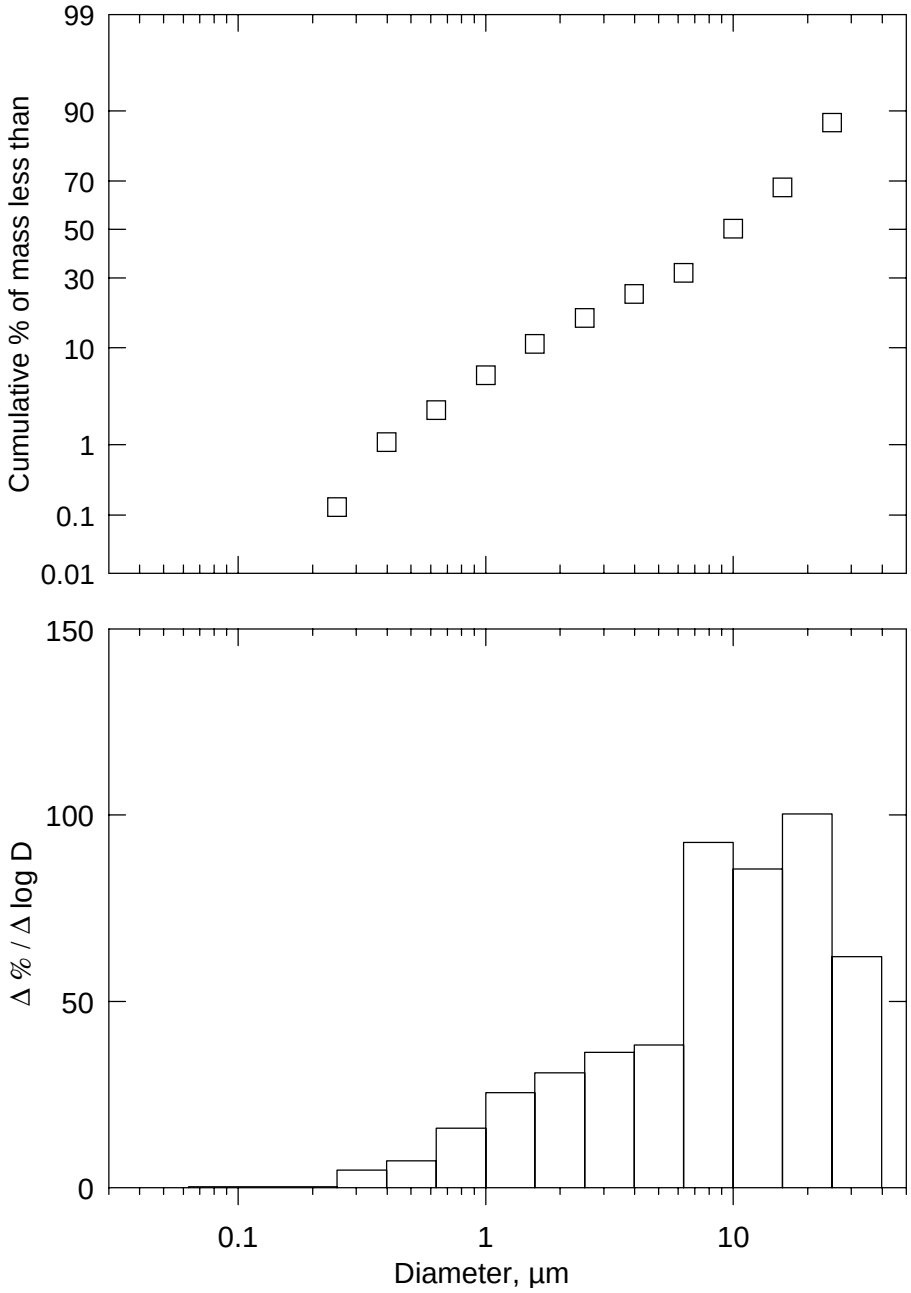

Figure 4-52. Cumulative and differential size distribution data measured for PSDF filter cake ash (ID # 4232) measured with a Shimadzu SA-CP4 Centrifugal Particle Size Analyzer. The MMD of this distribution is 9.9 µm, and its geometric standard deviation is 3.2. The D_{16} of this distribution is 2.3 µm, and its D_{84} is 23 µm. (This size distribution data includes the assumption that the sample contains no particles smaller than 0.063 µm.)

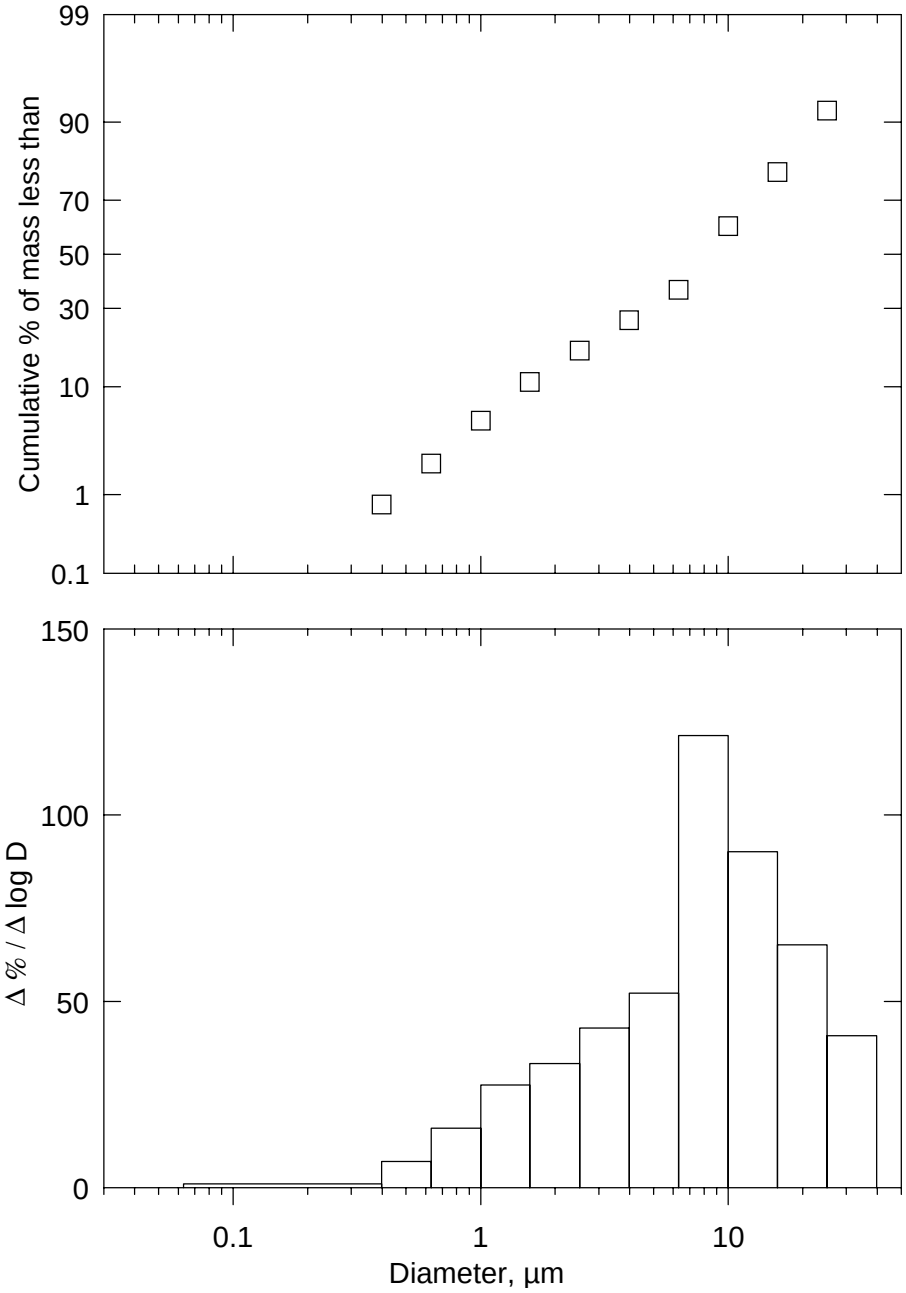

Figure 4-53. Cumulative and differential size distribution data measured for PSDF filter cake ash (ID # 4233) measured with a Shimadzu SA-CP4 Centrifugal Particle Size Analyzer. The MMD of this distribution is 8.1 µm, and its geometric standard deviation is 2.9. The D_{16} of this distribution is 2.3 µm, and its D_{84} is 19 µm. (This size distribution data includes the assumption that the sample contains no particles smaller than 0.063 µm.)

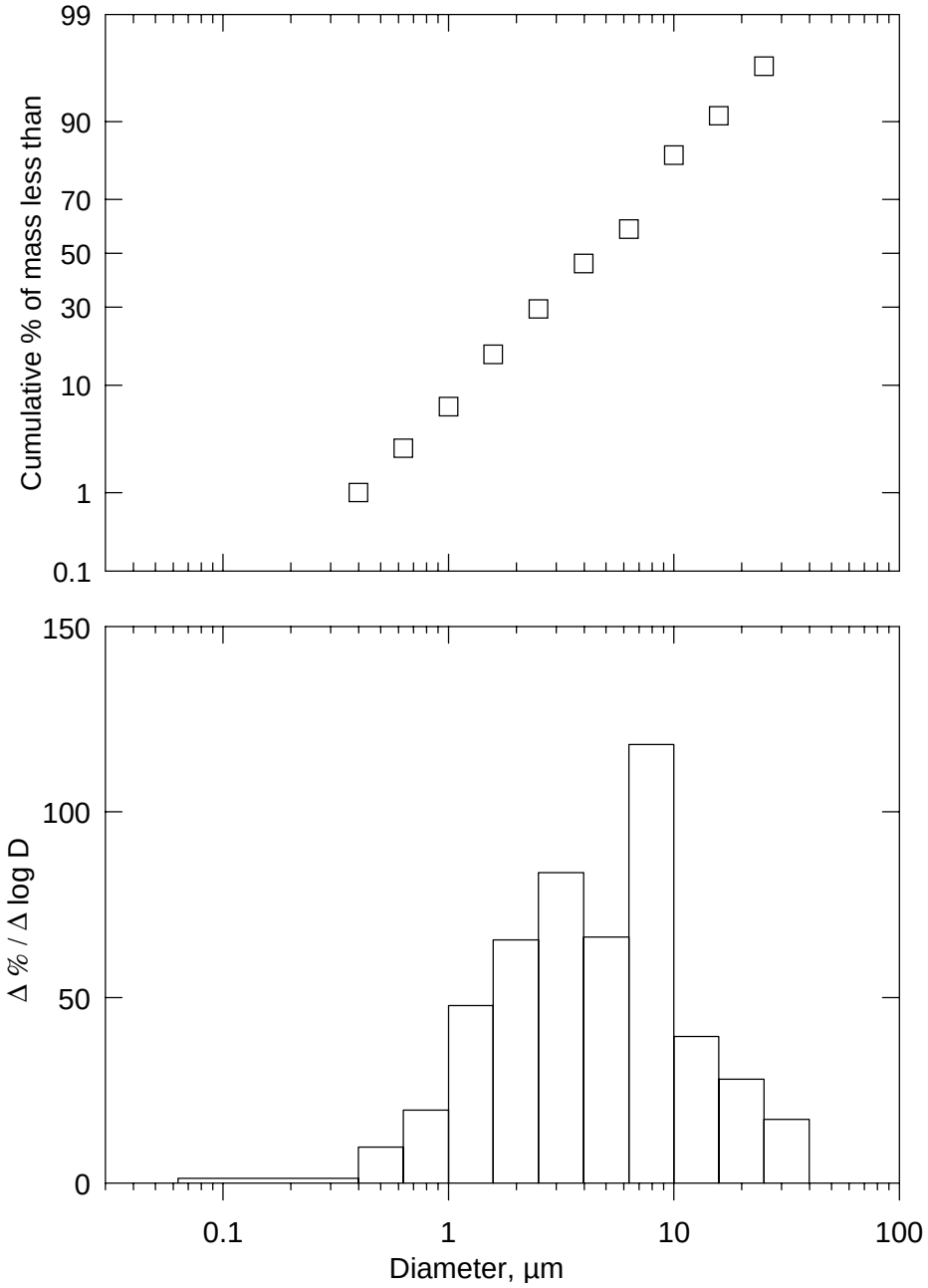

Figure 4-54. Cumulative and differential size distribution data measured for PSDF filter cake ash (ID # 4258) measured with a Shimadzu SA-CP4 Centrifugal Particle Size Analyzer. The MMD of this distribution is 4.6 µm, and its geometric standard deviation is 2.6. The D_{16} of this distribution is 1.6 µm, and its D_{84} is 11 µm. (This size distribution data includes the assumption that the sample contains no particles smaller than 0.063 µm.)

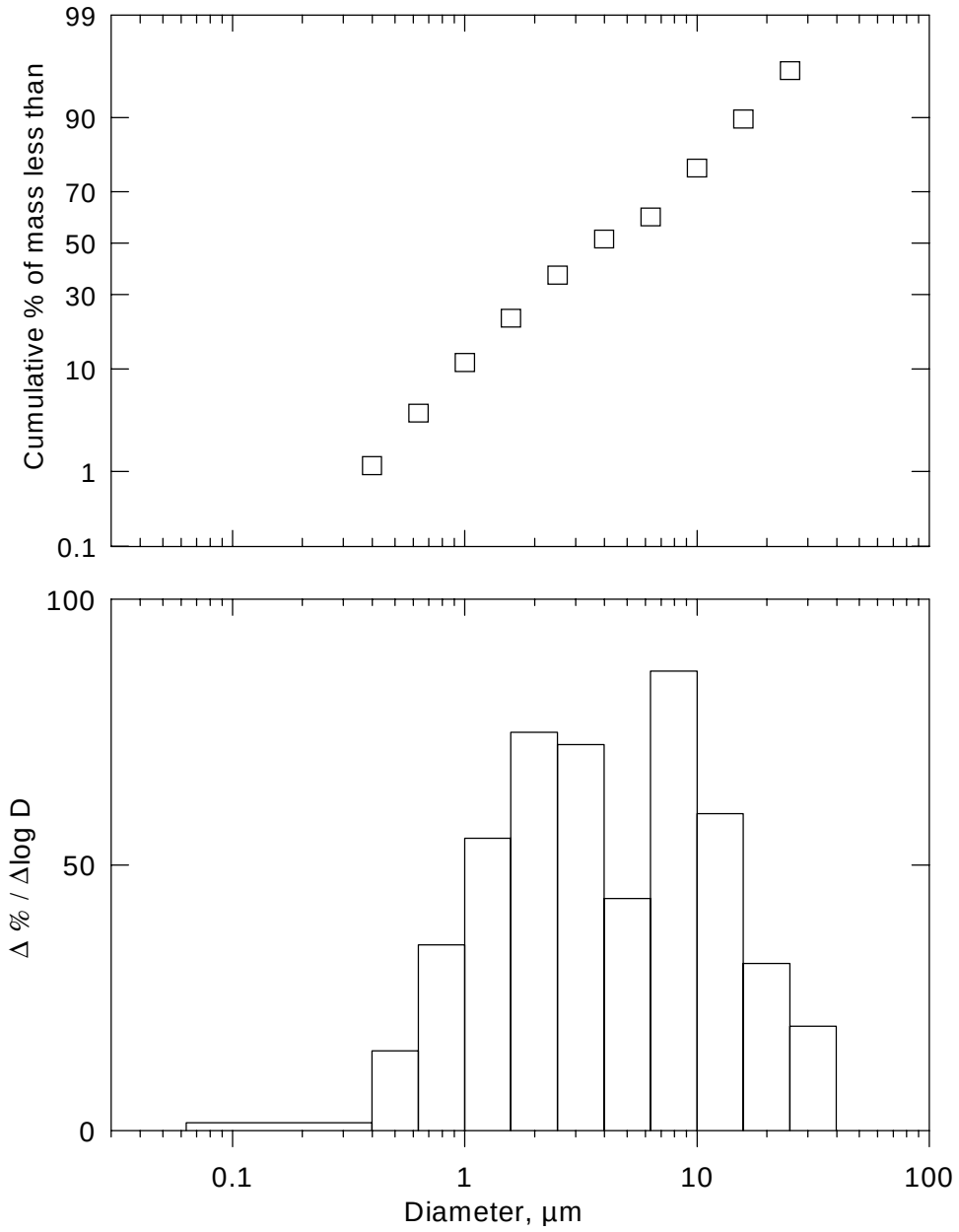

Figure 4-55. Cumulative and differential size distribution data measured for PSDF filter cake ash (ID # 4262) measured with a Shimadzu SA-CP4 Centrifugal Particle Size Analyzer. The D_{16} of this distribution is 1.2 µm, its D_{50} is 3.8 µm, its D_{84} is 13 µm, and its geometric standard deviation is 3.8. (These size distribution data include the assumption that the sample contains no particles smaller than 0.063 µm.)

During examination of the filter cakes on July 29, 1997 (following run CCT6), two small regions of filter cake (each with an area < 10 cm^2 and a thickness of about 3 mm) were observed that appeared to lie on top of the relatively uniform layer of filter cake covering almost all of the other filtering surfaces. (The appearance of these two regions suggests that prior to the multiple cleaning pulses that were applied to the filter assembly during shutdown, most, if not all, of the filter surface was covered with cake like these two small regions. Therefore, these two samples, # 4257 and # 4258, have been described as cleanable filter cake in Table 4-18. In fact, it is not possible to state definitively that these nodules represent filter cake normally removed during pulse cleanings; however, the term cleanable filter cake is applied to these samples to facilitate the discussion of their characteristics.) These regions were able to be removed intact as filter cake nodules. (The rest of the filter cake was not strong enough for any portions of it to be removed with its structure intact.) One of these nodules (from sample # 4257) was large enough and strong enough for a porosity determination to be performed on it using the ethanol impregnation method. The resultant value (78 %) is somewhat lower than the values measured with the core sampler and traversing transverse laser gauge for the regions of filter cake nearer to the candle surface. This discrepancy may be caused by differences in the methods used to measure porosity, or it may represent actual differences in the porosities of these two regions of filter cake. (Past experience with the impregnation of nodules with ethanol has shown that this method usually returns very consistent and accurate results.) The median diameter of ash from one of these two cleanable filter cake samples was measured to be 4.6 µm, which is significantly less than the value of 8.1 µm measured for sample # 4233 obtained from the filter vessel during this site visit. Scanning electron micrographs that were produced of sample # 4233 and sample # 4257 (Figures 4-56 and 4-57) do not show any major differences in the particle morphologies between the cleanable portion and the presumably older portion of the PSDF filter cakes. Because the operation of the PSDF regularly involves the variance of process parameters, the two cleanable regions of the cake discussed above may have been formed under significantly different operating conditions than the rest of the ash present on the filter elements.

Micrographs of filter cake ash sample # 4262 are shown in Figure 4-58. Because the PSDF samples that were obtained on January 20, 1998 following run TC01I included filter cake ashes and a corresponding hopper ash, analyses were performed to determine specific physical and chemical differences between samples obtained from these two locations. (These comparisons are subject to the limitations inherent in comparing hopper and filter cake ashes. The hopper ash is probably most representative of a brief operating period on, or just before, December 8, 1997. The filter cake ash, in addition to residing in the filter vessel when it was off line between December 9, 1997 and January 20, 1998, may also represent a variety of operating conditions in the period leading up to the shutdown of the transport reactor on December 9, 1997. Therefore, like the comparisons of ashes collected on different site visits, the discussion of the relative chemical and physical characteristics of these two ashes should be carefully interpreted.) Measurements of size distribution, uncompacted bulk porosity, and specific gas-flow resistance (with associated drag-equivalent diameter) all indicate that these two ashes (ID # 4294 and ID # 4295) have significantly different physical characteristics (Table 4-19). The specific gas-flow resistance of the PSDF filter cake ash (# 4294) calculated at a porosity of 76 % (9.7 in $H_2O \cdot min \cdot ft/lb$) indicates that collection of this ash should not cause unusually high filtering pressure losses.

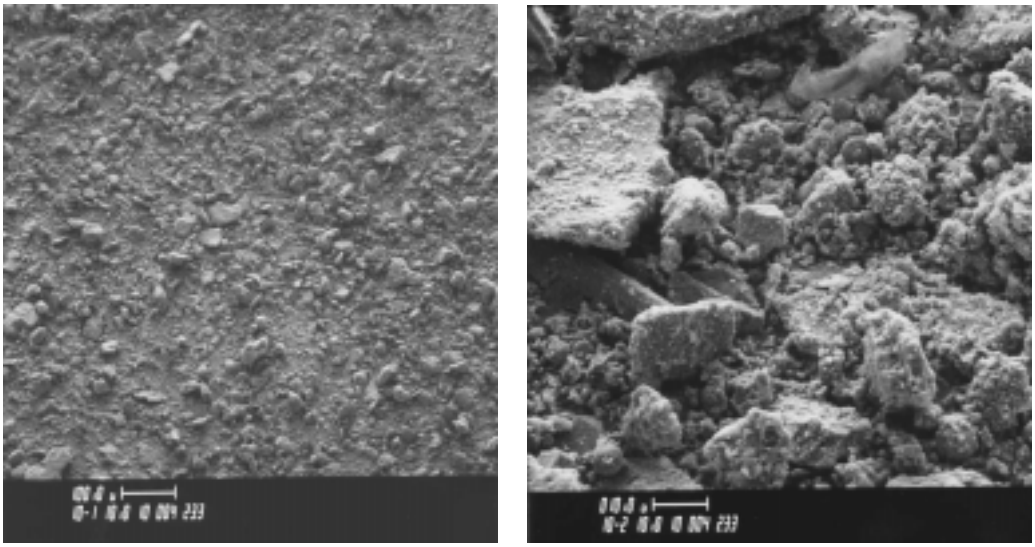

a b

c

Figure 4-56. Representative scanning electron micrographs of PSDF filter cake ash (ID # 4233) taken at a) 100X, b) 1000X, and c) 5000X.

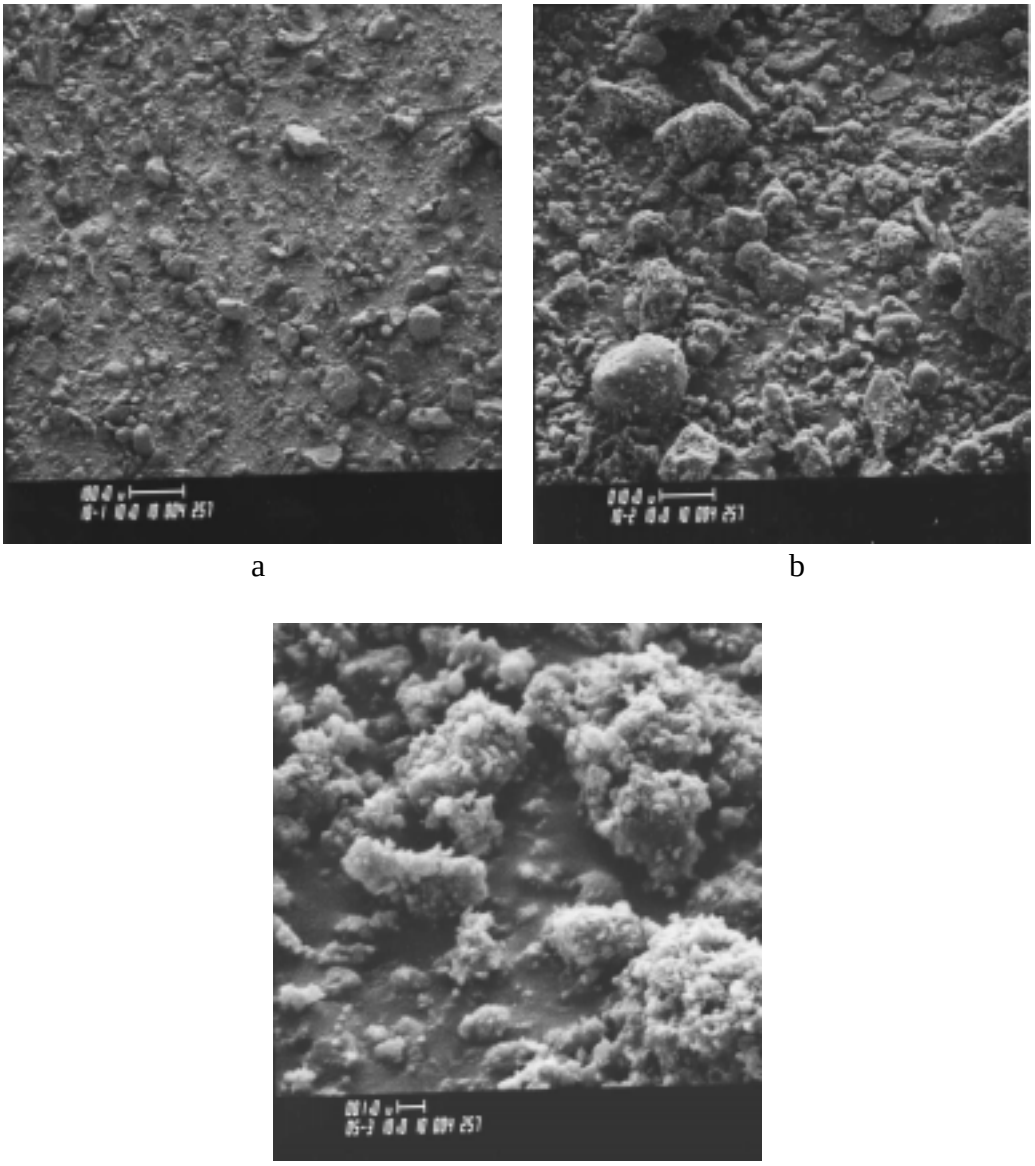

a b

c

Figure 4-57. Representative scanning electron micrographs of PSDF filter cake ash (ID # 4257) taken at a) 100X, b) 1000X, and c) 5000X.

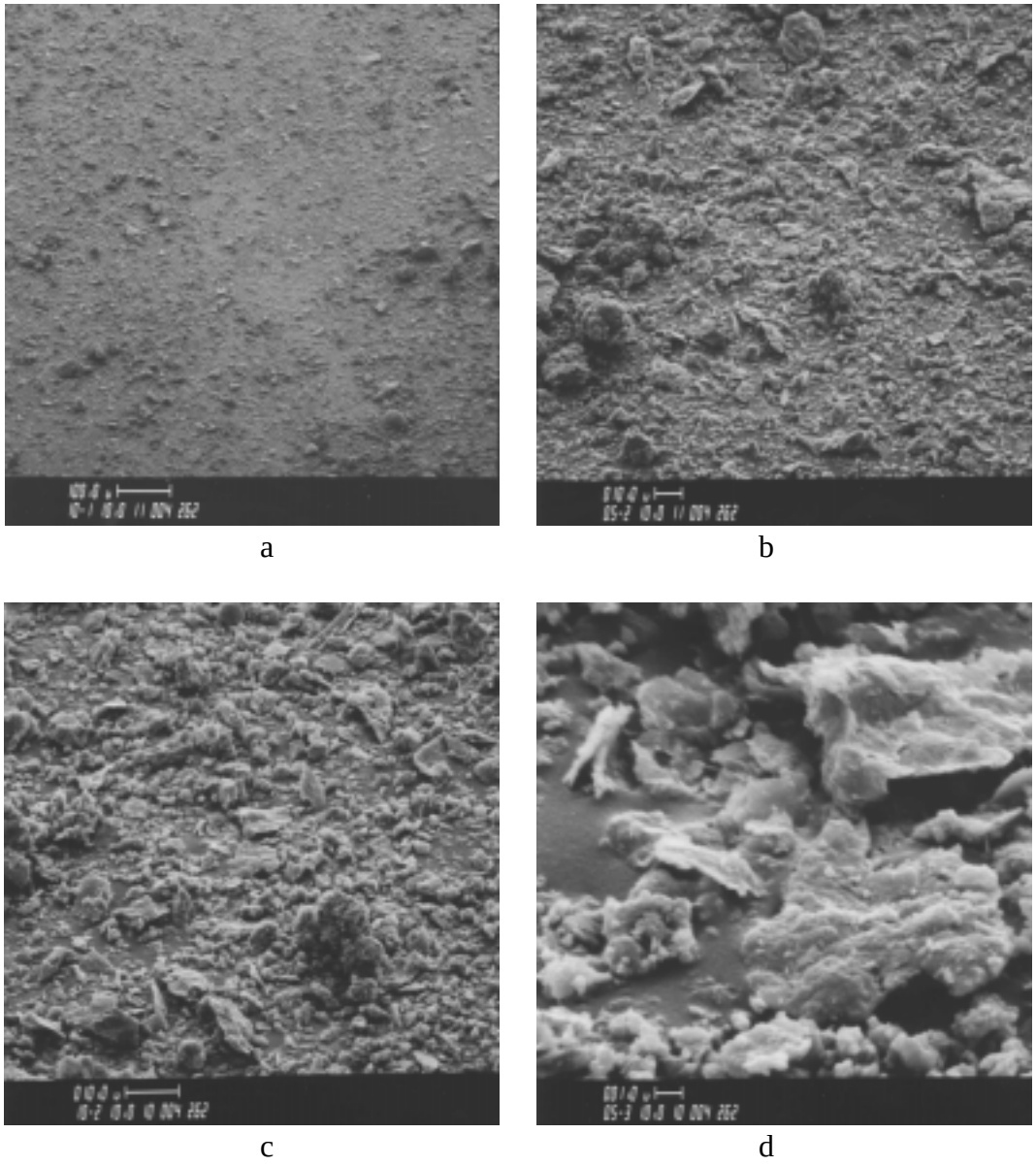

Figure 4-58. Representative scanning electron micrographs of PSDF filter cake ash (ID # 4262) taken at a) 100X, b) 500X, c) 1000X, and d) 5000X.

The chemical analyses performed on these two PSDF ash samples (Table 4-21) indicate enrichment of calcium and magnesium in the coarser hopper ash particles, and enrichment of alumina and iron compounds in the finer filter cake ash particles. The higher calcium and magnesium concentrations in the hopper ash reflect the coarseness of the sorbent in comparison to the fly ash particles exiting the transport reactor. There also is some enrichment of sulfur in the filter cake ash sample, presumably because of additional scrubbing of SO_2 from the flue gas by unreacted sorbent material in the filter cake. The increased LOI values measured for the filter cake ash (ID # 4294) over the hopper ash (ID # 4295) are most probably the result of water adsorption by the filter cake ashes during the period of time between shutdown of the transport reactor and the opening of the filter vessel for sample collection. Sample # 4294 had a long period of time of exposure to relatively cool, moist air prior to its collection from the surface of filter elements in the bottom plenum. In contrast, the hopper ash sample analyzed (ID # 4295) was collected from the ash discharge system during system operation on December 8, 1997, and was immediately placed in a sealed container. As with all samples after their collection, this hopper ash sample was kept sealed until it was analyzed.

The filter cake ash samples analyzed from the site visits in May 1998 - following run TC02 (ID # 4303) and January 1999 - following run TC05B (ID # 4307) have physical characteristics that are similar to the other PSDF filter cake ashes from periods of relatively stable operation. The chemical analysis of two filter cake ashes from January 1999 that are included in Table 4-21 are typical of other PSDF transport reactor ashes that have been analyzed.

The silica ratio and $R_{b/a}$ values presented for the PSDF ashes in Table 4-21 indicate that these ashes, unlike those from Tidd and Karhula, could be interpreted as not having a high probability of slagging (silica ratio > 65; $R_{b/a} < 0.5$) if present in a PC boiler.[12] (These quantities are defined in section *4.1 Laboratory Methods used to Characterize Samples*.) The slagging propensity for these PSDF ashes, as indicated by the silica ratio and $R_{b/a}$ values, is less than that of the Tidd or Karhula ashes. This correlates with the fact that ash bridging and the formation of strong ash deposits have not been a problem at the PSDF for the periods of operation covered in this report, and may also support the use of these quantities as a means of predicting the development of high-strength PFBC ash deposits in HGCU filters. (The lack of bridging at the PSDF may also be related to the operating temperature of the FL0301 filter vessel, which was maintained below the temperatures at which the filter vessels at Tidd and Karhula were periodically operated.)

4.6 PIÑON PINE POWER PROJECT

In the Piñon Pine IGCC Power Project, the Sierra Pacific Power Company is operating a KRW fluidized bed gasifier on low sulfur coal from southern Utah.[14] The net power output of the plant is 99.7 MWe. Hot gas cleanup is provided by a Siemens Westinghouse barrier filtration system.[8] The filtration vessel is 10 ft. in diameter, and contains 748 candle filter elements on sixteen plenum assemblies. The filter design departs from earlier, smaller-scale Siemens Westinghouse designs in that all maintenance on the filter elements (initial installation, inspection, and element replacement) is performed inside the filter vessel by

specially trained personnel. The Piñon Pine gasifier is started up on coke breeze before switching to coal.

The Piñon Pine gasifier was operated for about seven hours on June 2, 1998 at a pressure of 100 psig and over a temperature range of 1600 to 1800 °F. Problems not directly related to filter operation caused the gasifier to be shut down after this short run. Sample # 4316 was collected following this brief period of operation from the system of hoppers attached to the Siemens Westinghouse filter vessel. Because of the brevity of this run, it is not known to what extent this sample represents nominal gasifier operation. Two additional char samples were collected following another brief run that occurred in January, 1999. These three Piñon Pine samples which were analyzed under this task are identified in Table 4-22. A range of measured physical and chemical characteristics of the three Piñon Pine samples are summarized in Tables 4-23 and 4-24.

Table 4-22
Identification of Piñon Pine Samples Received for Analysis

ID #	date	sample location
4316	June 2, 1998	hopper
4349	January 1999	hopper
4350	January 26, 1999	filter cake

Table 4-23
Physical Analyses of Piñon Pine Char Samples

quantity ID #	4316	4349	4350
mass median diameter, µm (Microtrac Analyzer)	19	12	7.4
mass median diameter, µm (Bahco Classifier)	12	--	--
specific surface area, m^2/g	107	35.1	28.2
filter cake nodule porosity, %	--	--	63 to 68
uncompacted bulk porosity, %	80	78	85
drag-equivalent diameter, µm	1.96	1.58	--
true particle density, g/cm^3	2.38	2.19	--
tensile strength, N/m^2	2.3	--	--
specific gas-flow resistance, in H_2O·min·ft/lb (at cake porosity of 80 %)	7.7	--	--
specific gas-flow resistance, in H_2O·min·ft/lb (at cake porosity of 78 %)	--	18	--
specific gas-flow resistance, in H_2O·min·ft/lb (at cake porosity of 68 %)	--	64	--
specific gas-flow resistance, in H_2O·min·ft/lb (at cake porosity of 63 %)	--	106	--

Table 4-24
Measured Chemical Characteristics of Piñon Pine Char Samples, % wt.

Constituent	4316	4349	4350
Li_2O	0.01	0.02	0.02
Na_2O	2.1	1.2	1.2
K_2O	0.27	0.38	0.39
MgO	1.2	1.3	1.3
CaO	50.4	46.2	47.5
Fe_2O_3	4.2	4.8	4.9
Al_2O_3	9.2	11	10.6
SiO_2	19.9	20.4	20.1
TiO_2	1.8	1.9	1.8
P_2O_5	0.43	0.2	0.2
SO_3	8.0	8.9	7.7
LOI	53.0	63	59.6
soluble $SO_4^=$	3.2	3.2	2.7
Equilibrium pH*	11.53	--	--

* dimensionless

The tensile strength of sample # 4316 is relatively low. This low tensile strength may increase the likelihood of particle reentrainment following cleaning pulses. Even though sample # 4316 has a relatively high specific surface area, its drag-equivalent diameter and uncompacted bulk porosity are high enough to keep the specific gas-flow resistance from being excessively high. (The strong effect that decreasing values of assumed cake porosity have on specific gas-flow resistance can be observed in the data presented in Table 4-23 for sample # 4349.)

Figures 4-59 and 4-60 present scanning electron micrographs of sample # 4316. Because of the high calcium-to-sulfur ratio in this sample, further tests were conducted to determine the relative amounts of these two constituents as a function of particle size. The size distribution of sample # 4316 was measured with the Leeds and Northrup Microtrac Particle Size Analyzer (Figure 4-61) and also with the Bahco Aerodynamic Classifier. The latter procedure yielded the size distribution data shown in Figure 4-62 and Table 4-25, as well as size-fractionated particulate samples for chemical analysis. Six of the size fractions produced in the classification of this sample were submitted for determination of loss-on-ignition (LOI), and calcium and sulfur contents. The results of these chemical analyses are presented in Table 4-26, along with corresponding values for the source material. All nine size fractions and the source sample were also submitted for C-H-N analyses, which are summarized in Table 4-27 and Figure 4-63. Both types of chemical analyses indicate that in general, the sorbent material is concentrated in the larger particles that are collected in the filter hopper, while the finer particles presumably contain a higher proportion of char. The coarsest size fraction (diameter > 26.7 μm) deviated from this trend, suggesting a bimodal size distribution of the char particles.

Table 4-25
Size Distribution Data Measured for Piñon Pine Filter Fines (ID # 4316)
with a Bahco Aerodynamic Classifier

particle size range	% of mass in size range	cumulative % of mass smaller than upper size limit
diameter < 1.6 µm	6.9	6.9
1.6 µm < diameter < 2.5 µm	5.9	12.8
2.5 µm < diameter < 4.7 µm	13.8	26.7
4.7 µm < diameter < 8.2 µm	10.7	37.4
8.2 µm < diameter < 11.5 µm	9.6	47.0
11.5 µm < diameter < 18.9 µm	16.7	63.7
18.9 µm < diameter < 23.9 µm	5.9	69.6
23.9 µm < diameter < 26.7 µm	2.5	72.1
diameter > 26.7 µm	27.9	100.0

Table 4-26
Selected Chemical Constituents Measured for Piñon Pine Filter Fines (ID # 4316)
and Six Selected Size Fractions

particle size range	LOI, % wt.	CaO, % wt.	SO_3, % wt.
source sample (all diameters)	53.0	50.4	8.0
diameter < 1.6 µm	69.5	41.9	8.5
1.6 µm < diameter < 2.5 µm	68.3	45.2	7.9
2.5 µm < diameter < 4.7 µm	65.3	47.9	7.0
4.7 µm < diameter < 8.2 µm	60.2	49.3	7.2
11.5 µm < diameter < 18.9 µm	43.2	54.8	7.8
diameter > 26.7 µm	44.4	55.2	6.8

Table 4-27
C-H-N Analyses of Six Selected Size Fractions of Piñon Pine Filter Fines (ID # 4316)

particle size range	carbon, % wt.	hydrogen, % wt.	nitrogen, % wt.
source sample (all diameters)	46.59	0.74	1.04
diameter < 1.6 µm	62.90	1.22	1.00
1.6 µm < diameter < 2.5 µm	62.26	1.16	0.67
2.5 µm < diameter < 4.7 µm	59.03	1.09	0.44
4.7 µm < diameter < 8.2 µm	54.20	0.99	0.39
8.2 µm < diameter < 11.5 µm	48.24	0.80	0.61
11.5 µm < diameter < 18.9 µm	36.65	0.62	0.49
18.9 µm < diameter < 23.9 µm	35.26	0.58	0.88
23.9 µm < diameter < 26.7 µm	36.11	0.64	0.94
diameter > 26.7 µm	50.72	0.74	0.62

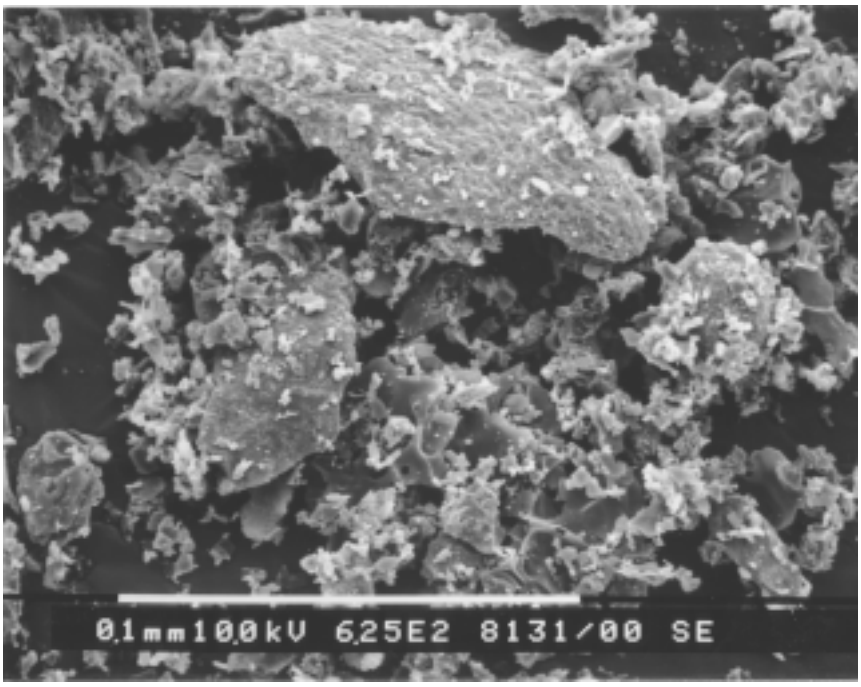

Figure 4-59. Scanning electron micrograph of Piñon Pine IGCC Power Project filter fines particulate sample (ID # 4316). The white bar at the bottom of the micrograph represents a length of 100 µm.

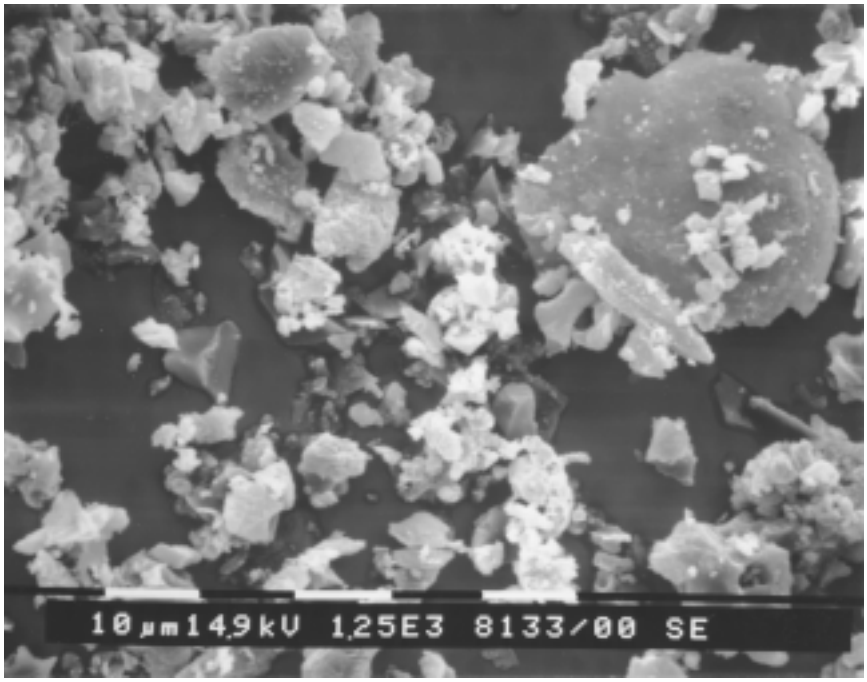

Figure 4-60. Scanning electron micrograph of Piñon Pine IGCC Power Project filter fines particulate sample (ID # 4316). The white bars at the bottom of the micrograph represent lengths of 10 µm.

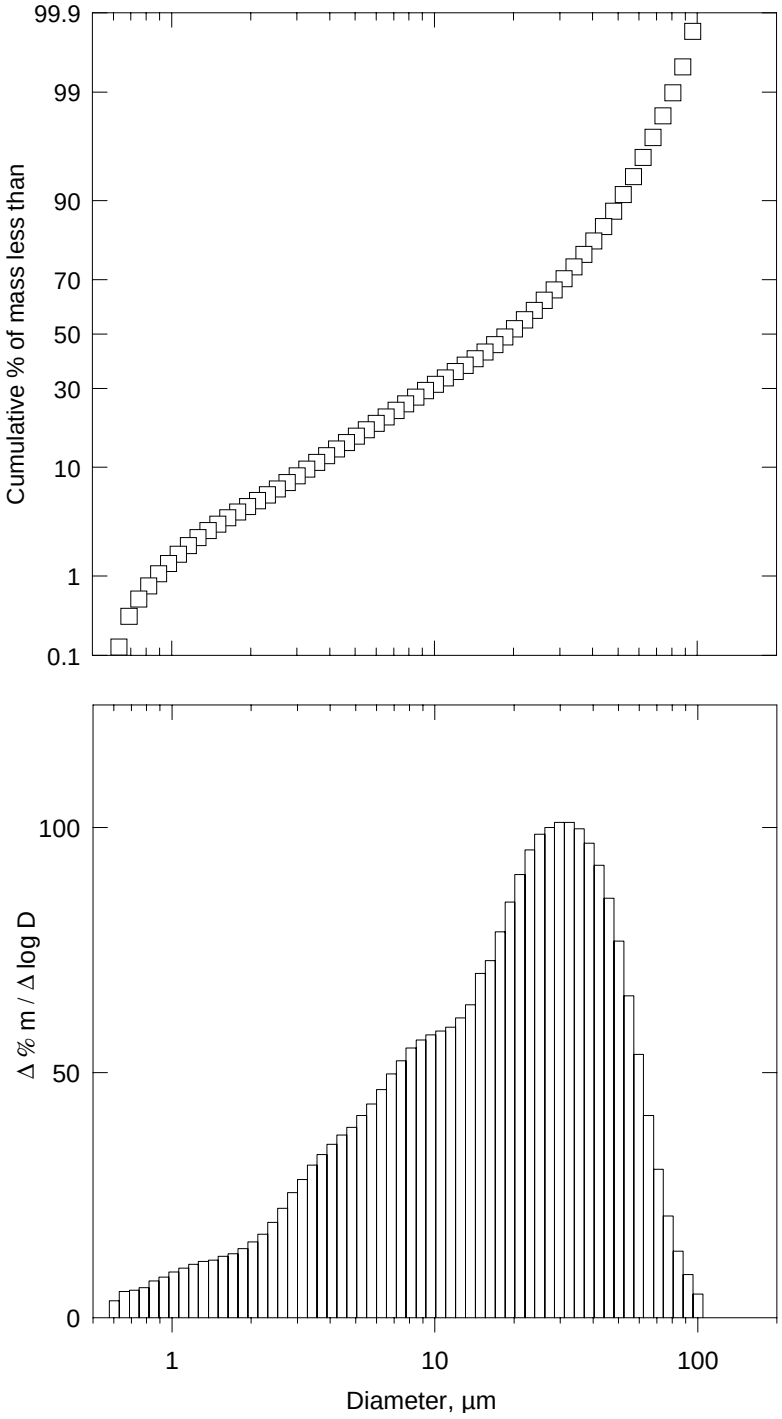

Figure 4-61. Differential and cumulative size distribution data measured for Piñon Pine filter fines (ID # 4316) with a Leeds and Northrup Microtrac Particle Size Analyzer. The MMD of this distribution is 19 µm.

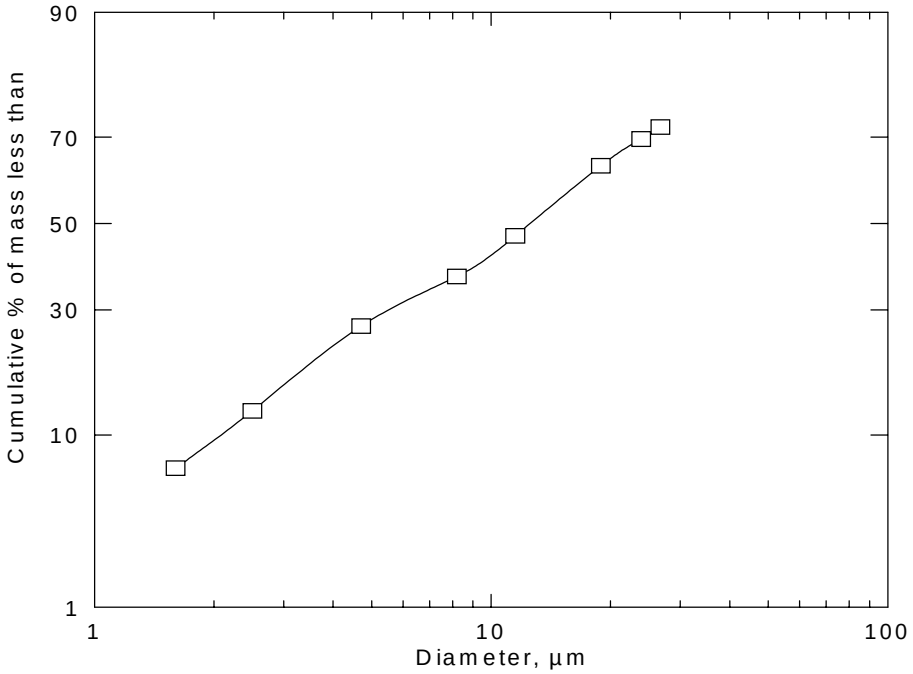

Figure 4-62. Cumulative particle size of the Piñon Pine filter fines (ID # 4316) measured with a Bahco Aerodynamic Classifier.

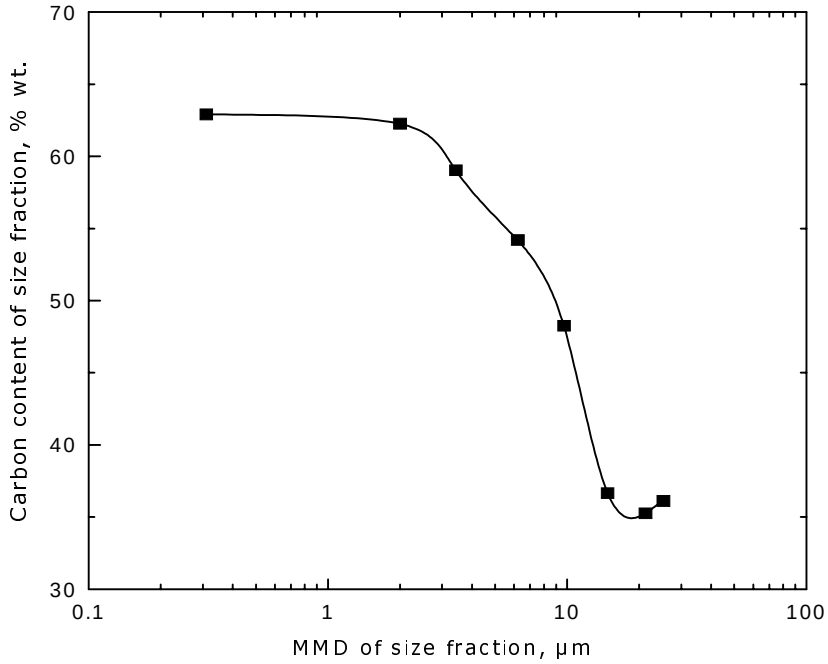

Figure 4-63. Carbon contents of the various size fractions of Piñon Pine filter fines (ID # 4316). The carbon content (50.7 %) of the size fraction of particles larger than 26.7 µm is not represented on this plot.

Leo Leighton of Sierra Pacific Power Company provided two particulate samples collected from a run made at the Piñon Pine facility in January, 1999. The first sample, ID# 4349, was collected from the system of hoppers that receive the particulate matter collected in the Siemens Westinghouse filter vessel. The second sample, ID# 4350, was collected from the surface of the filter elements during a filter inspection on January 26, 1999.

Figures 4-64 through 4-71 present representative micrographs of these two samples. Each sample comprises a wide size distribution of irregularly-shaped particles. The measured size distributions of these two samples are compared in Figure 4-72, and this comparison is the basis for calculation of the degree of inertial collection (settling) of relatively coarse particles in the Siemens Westinghouse filter vessel at Piñon Pine (Figure 4-73). The degree of assumed settling in the filter vessel was calculated by comparing the measured size distribution of filter cake particulate (ID # 4350) with the size distribution data measured for Piñon Pine particulate collected in the filter hopper (ID # 4349). In this calculation, a scaling factor of 0.80 was applied to the filter cake particulate size distribution to cause the finest portion of the two distributions shown in Figure 4-72 to coincide. Consequently, this analysis assumes 20 % of the entrained mass entering the vessel settles into the hopper without ever reaching the filter cake.

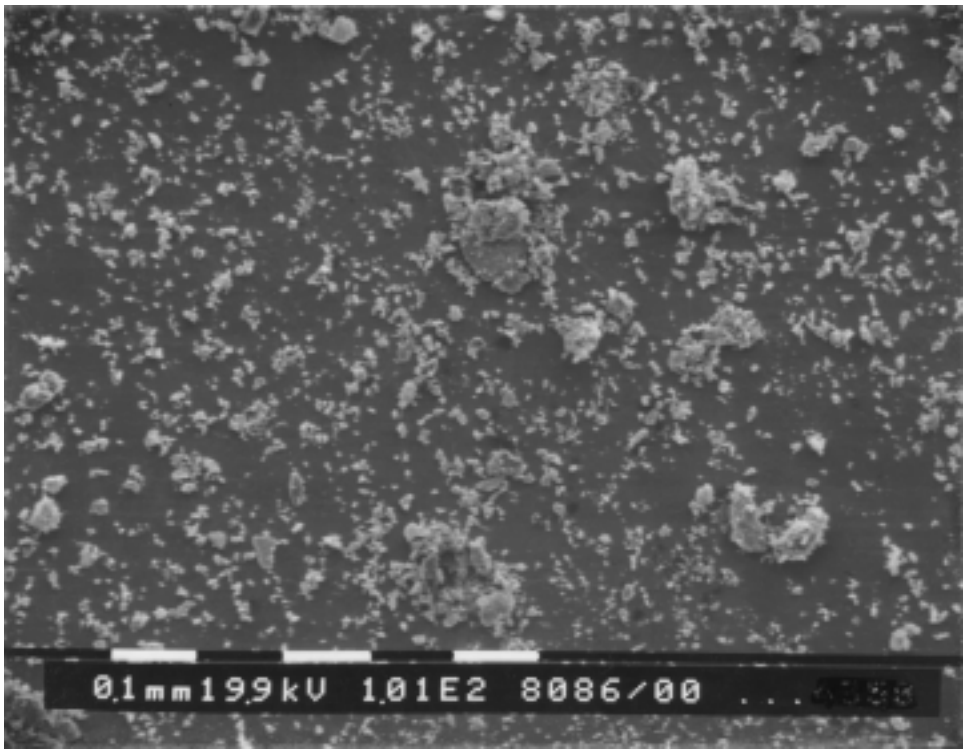

Figure 4-64. Representative scanning electron micrograph of Piñon Pine gasifier char (ID # 4349) collected in January 1999 from the filter hopper. The black and white bars at the bottom of the micrograph represent lengths of 100 µm.

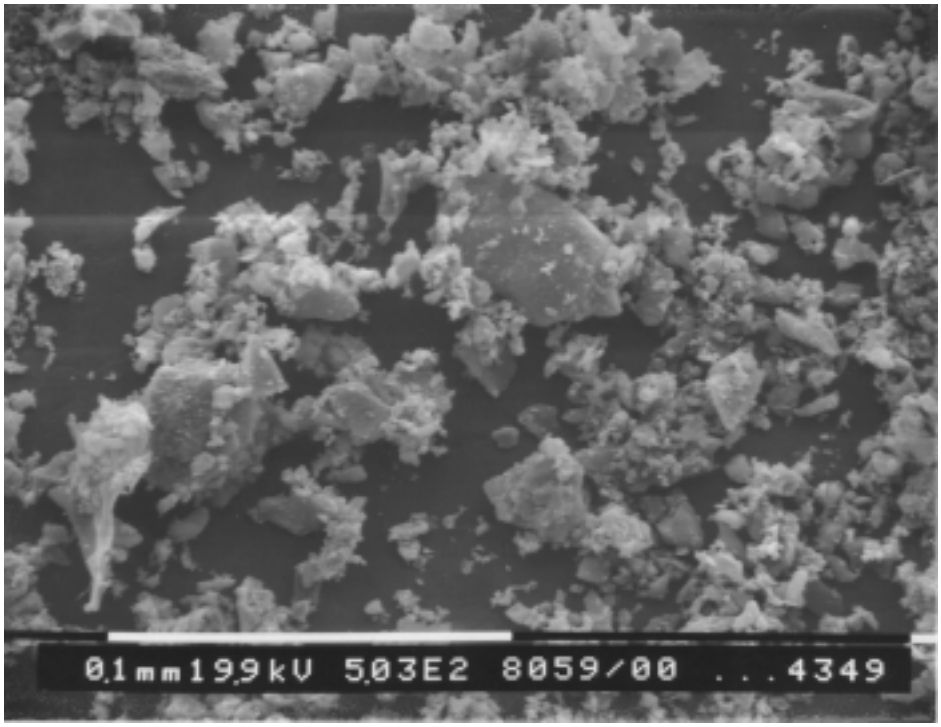

Figure 4-65. Representative scanning electron micrograph of Piñon Pine gasifier char (ID # 4349) collected in January 1999 from the filter hopper. The white bar at the bottom of the micrograph represents a length of 100 µm.

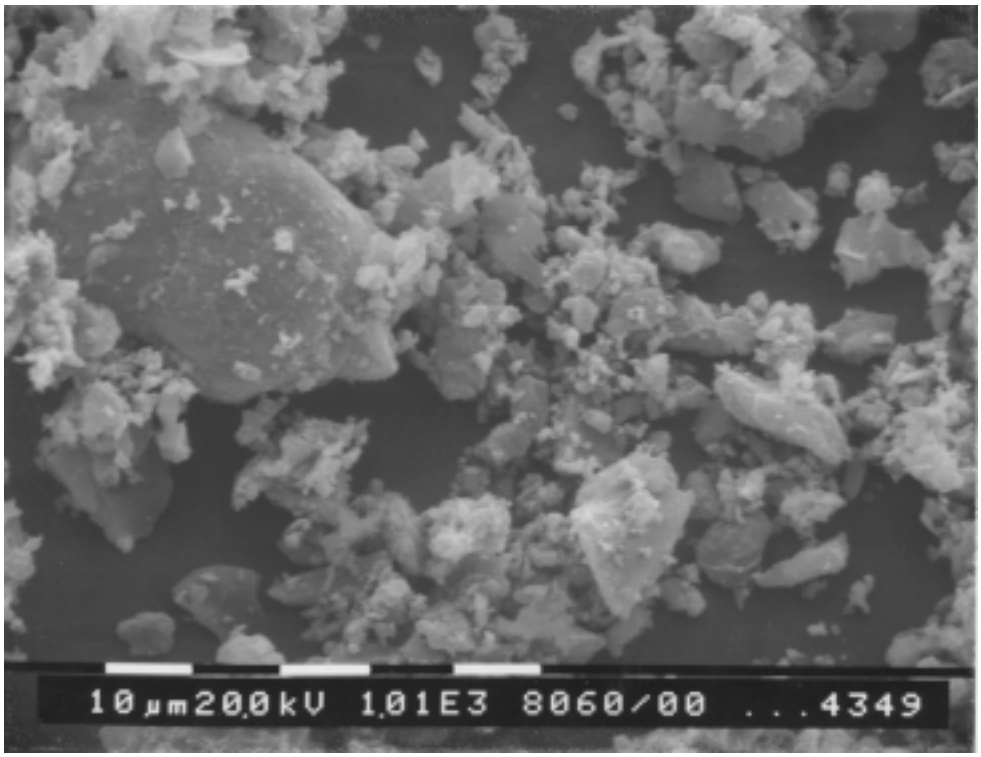

Figure 4-66. Representative scanning electron micrograph of Piñon Pine gasifier char (ID # 4349) collected in January 1999 from the filter hopper. The black and white bars at the bottom of the micrograph represent lengths of 10 µm.

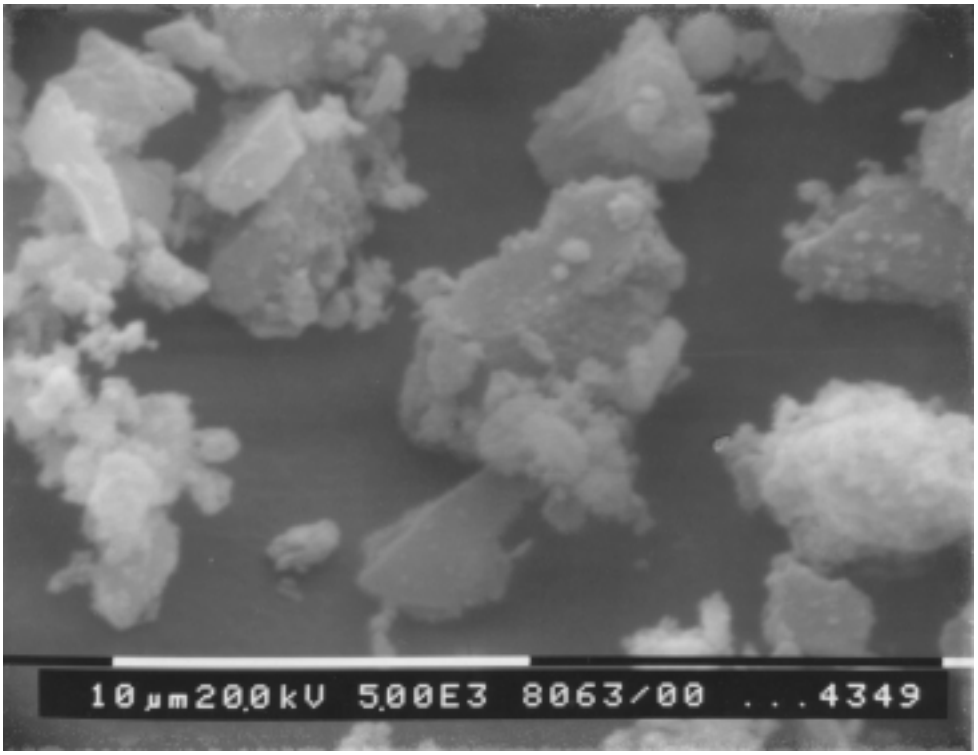

Figure 4-67. Representative scanning electron micrograph of Piñon Pine gasifier char (ID # 4349) collected in January 1999 from the filter hopper. The white bar at the bottom of the micrograph represents a length of 10 µm.

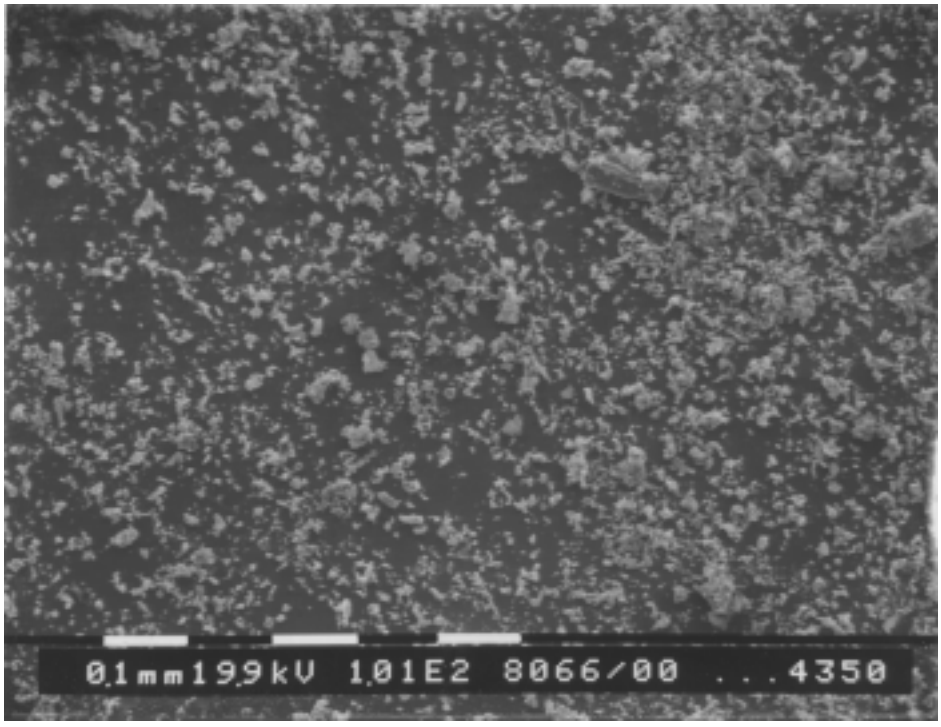

Figure 4-68. Representative scanning electron micrograph of Piñon Pine gasifier char (ID # 4350) collected in January 1999 as part of the filter cake. The black and white bars at the bottom of the micrograph represent lengths of 100 µm.

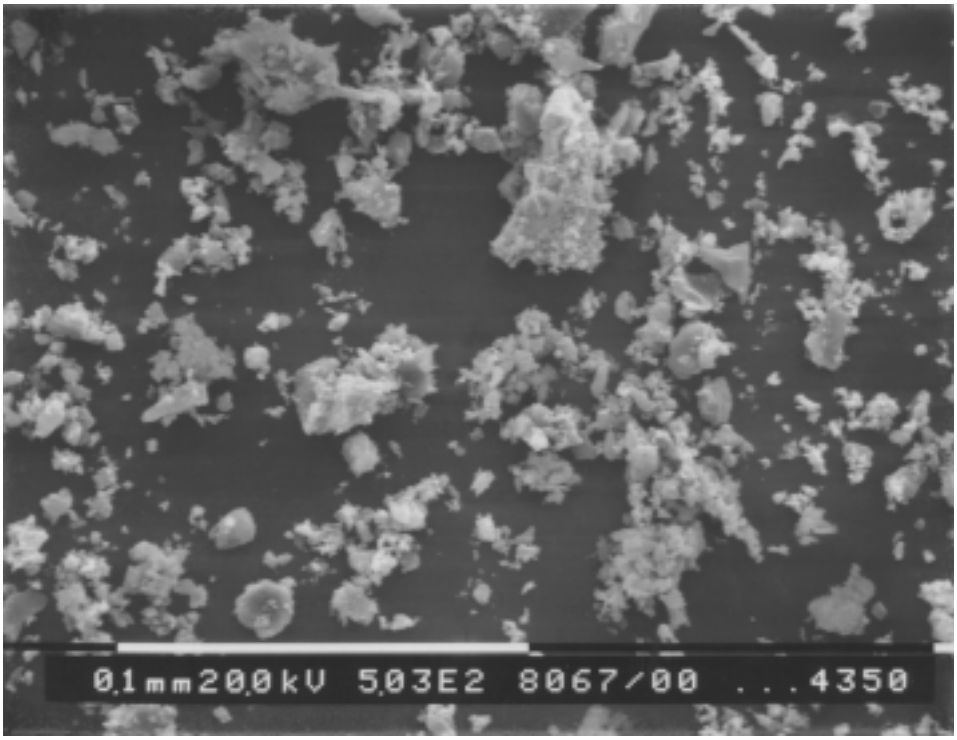

Figure 4-69. Representative scanning electron micrograph of Piñon Pine gasifier char (ID # 4350) collected in January 1999 as part of the filter cake. The white bar at the bottom of the micrograph represents a length of 100 µm.

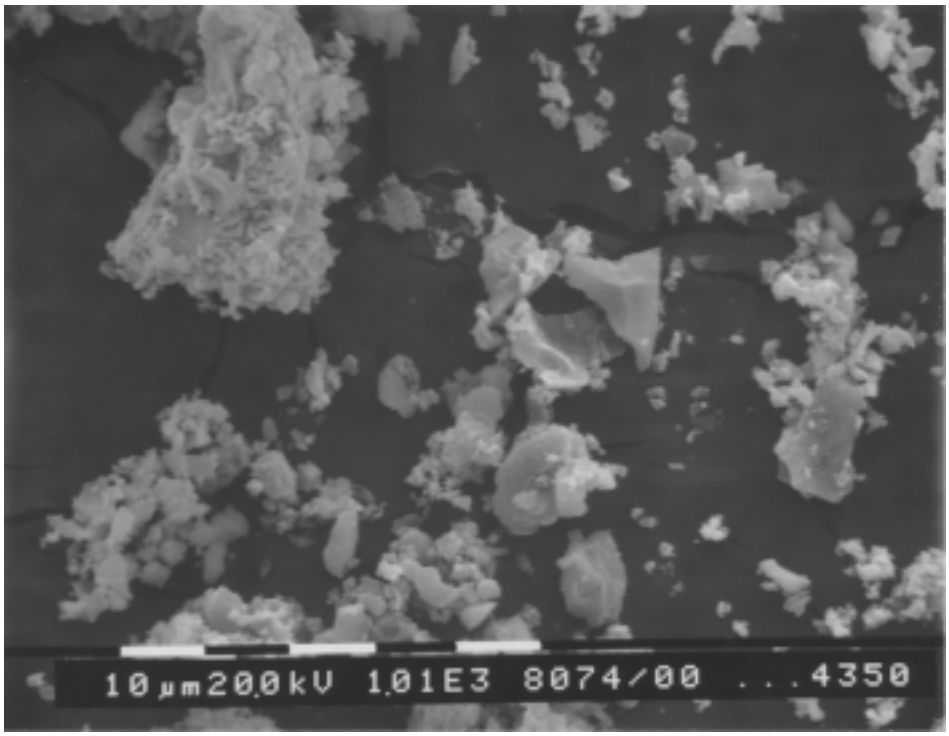

Figure 4-70. Representative scanning electron micrograph of Piñon Pine gasifier char (ID # 4350) collected in January 1999 as part of the filter cake. The black and white bars at the bottom of the micrograph represent lengths of 10 µm.

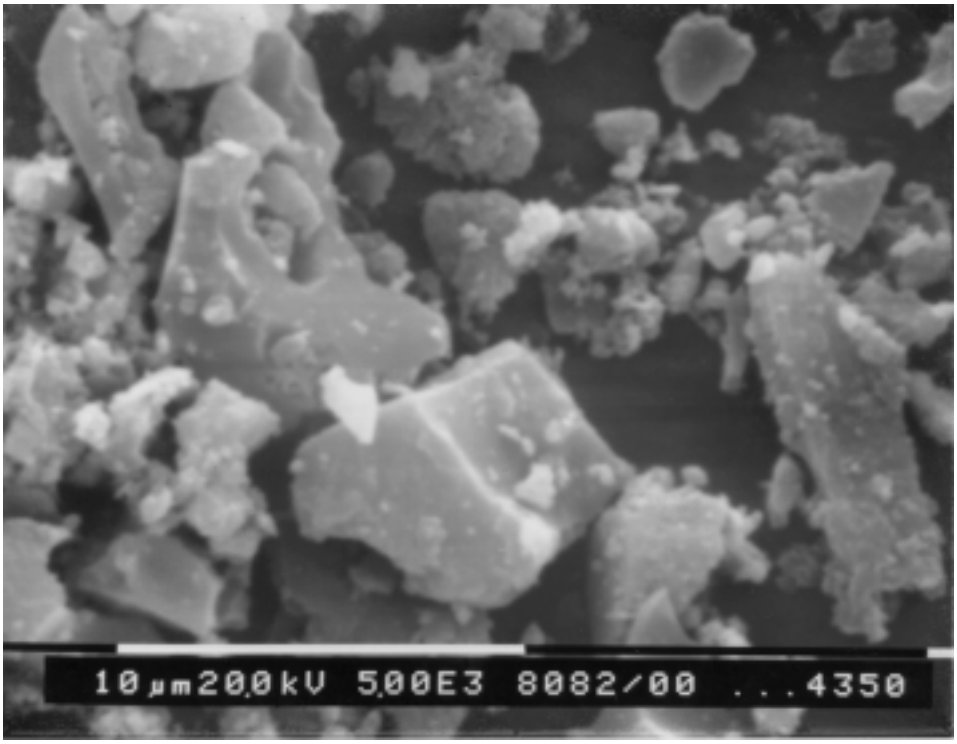

Figure 4-71. Representative scanning electron micrograph of Piñon Pine gasifier char (ID # 4350) collected in Jnauary 1999 as part of the filter cake. The white bar at the bottom of the micrograph represents a length of 10 µm.

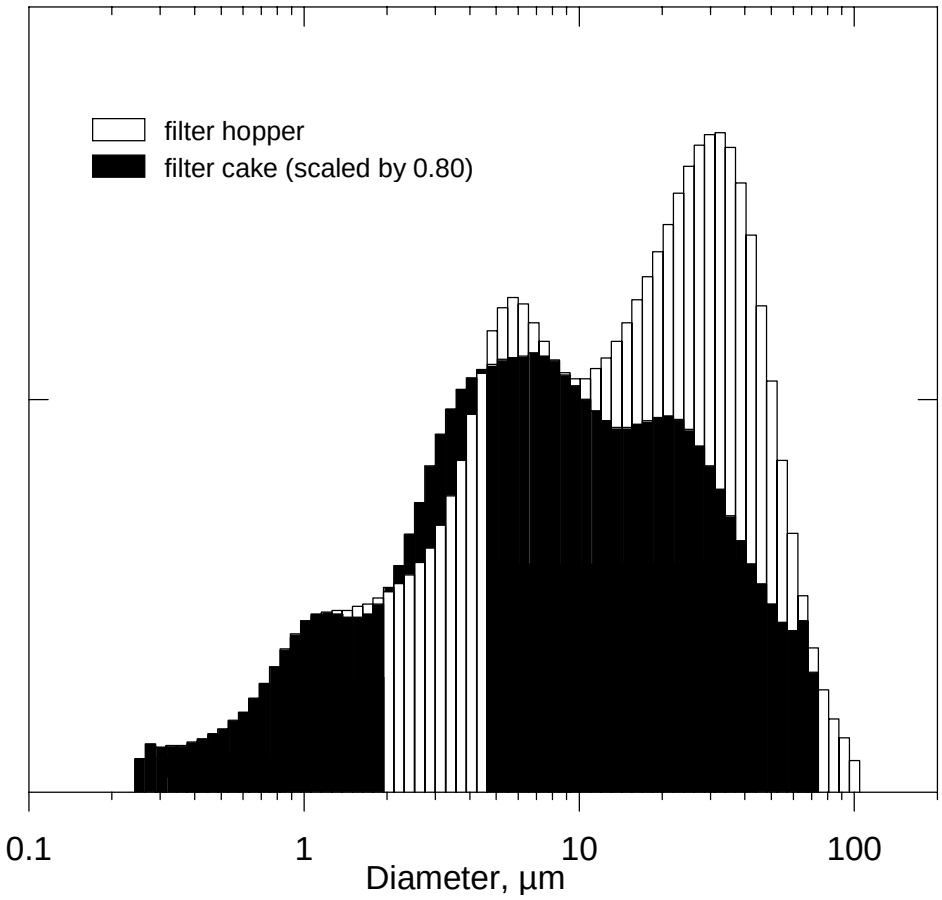

Figure 4-72. Differential size distribution data measured for Piñon Pine particulate matter collected in January 1999. The size distribution of the material collected in the filter hopper (ID # 4349) is overlaid with the size distribution of particulate matter collected as part of the filter cake (ID# 4350). A scaling factor of 0.80 was applied to the filter cake particulate size distribution to cause the finest portion of these two distributions to coincide.

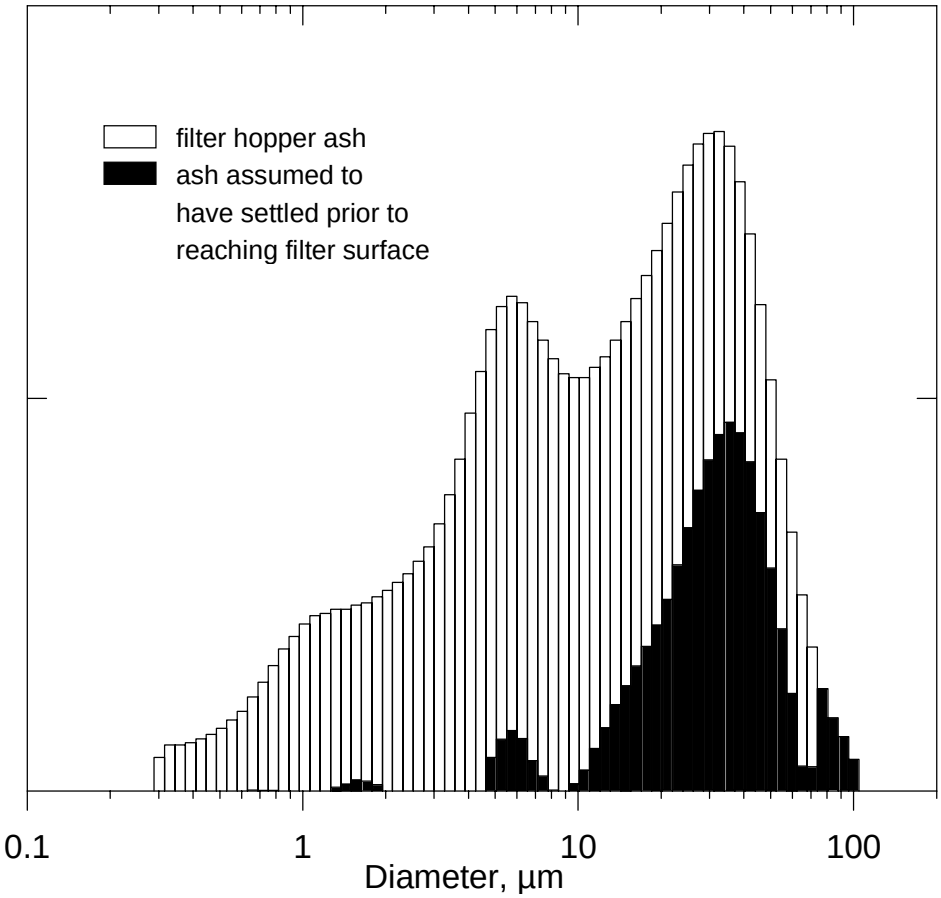

Figure 4-73. Differential size distribution data measured for Piñon Pine particulate matter collected in January 1999. The size distribution of the filter hopper char is overlaid with the size distribution of particulate matter assumed to have settled into the hopper without ever reaching the surface of the filter cake.

Mr. Leighton described the filter cake sample as containing nodules prior to shipment. Although most of the nodules were apparently broken up during shipping to the Southern Research Institute laboratory, the filter cake sample still contained some small, thin nodules (0.01 to 0.02 g, about 1 mm thick) that were characterized with porosity and SEM analyses.

It is important to note the measured porosity of the filter cake nodules from sample # 4350 that are presented in Table 4-23. These values (63 to 68 %) are significantly lower than the uncompacted bulk porosity value of 85 %. Because it is believed that filter cakes initially form with a porosity near the uncompacted bulk porosity value, it must be assumed that the portion of the filter cake represented by these small nodules has been compacted during filtration. The most likely mechanism for this compaction is the force of the cumulative filtering pressure applied across the filter cake. Although it may only be a small, thin (1 mm) portion of the cake that is compressed to this degree, the effect of this compression on overall filtering pressure drop is quite significant. Filter cake compaction from an assumed initial value of 85 % to a final value of 63 % would cause the filtering pressure drop to increase by a factor of more than 20. Although the values for specific gas-flow resistance shown in Table 4-23 were measured for the hopper char, the magnitude of pressure drop increase would be the same for filter cake char. There was insufficient sample to perform the measurement of specific gas-flow resistance on the filter cake char sample, but it is reasonable to assume that it would be about the same as the value measured for the hopper char sample (at an equivalent cake porosity). This assumption is based on the fact that although the median diameter of the filter cake char sample is somewhat smaller than that of the hopper char sample, the specific surface areas of these two samples are similar. The drag-equivalent diameter of the hopper char sample is not so small as to indicate excessive pressure drop for uncompacted filter cakes. However, at a cake porosity equal to that of the filter cake nodules that were analyzed, pressure drops would become excessive.

Example calculations of the effect that filter cake collapse to a value of 65 % might have at Piñon Pine are given in the following discussion. For the purposes of these calculations, several parameters must be assumed. The filter vessel, operating at 1000 °F, is assumed to receive 5634 lb/hr (or 2.64 lb for each square foot of active filter surface area/hr) of entrained material [14], 80 % of which is estimated to accumulate in the filter cake. The actual face velocity of the gas through the filter cake is assumed to be 5 ft/min. The flue gas is assumed to have a viscosity of 365 µpoise at 1000 °F. The filter cake is assumed to comprise material with the characteristics of sample # 4349 (drag-equivalent diameter = 1.58 µm, true particle density = 2.19 g/cm^3) and is further assumed to have a porosity of 65 %. (These char characteristics equate to a specific gas-flow resistance of 87 in H_2O·min·ft/lb.) Based on these input parameters and assumptions, the pressure drop across the filter cake would increase at a rate of about 30 in H_2O per minute between cleaning cycles. It is important to note that the key input parameter that causes this rate of pressure drop accumulation to be so high is the assumed filter cake porosity of 65 %. It is unlikely that the entire filter cake will have a porosity this low. Because the pressure drop incurred through the depth of the filter cake provides the compacting force that would tend to drive the filter cake structure to a porosity of around 65 % , it is more likely that only the portion of the cake closest to the surface of the candle filter would collapse to this extent. However, these calculations illustrate that as the proportion of the filter cake that collapses to this low porosity increases, the accumulated pressure loss through the cake will increase very rapidly.

The chemical compositions of the two samples from January 1999 demonstrate the similarity between these samples. Each sample has a high LOI value, with a large proportion of calcium, silicon, sulfur, aluminum, and iron in the ignited sample residue. In both samples, the sulfur has apparently been converted from its reduced state to sulfate. This conversion is to be expected because of the nearly inevitable exposure of the char samples to air as they are collected from the gasifier facility, and as they are subsequently handled during analysis. (The values of SO_3 measured in the ignited samples are comparable with the soluble $SO_4^=$ values in the as-received samples. When the SO_3 values are corrected for LOI, the sulfur content of hopper char is 3.3 %, and the sulfur content of the filter cake char is 3.1 %. These values agree with the sulfate values presented in Table 4-24.)

SEM analyses were performed on a fresh fracture surface of one of the filter cake nodules included in sample # 4350. Micrographs of the fracture surface are shown in Figures 4-74 through 4-76. These micrographs show irregularly-shaped particles with a wide range of sizes. A large proportion of these appear to be submicron in size. The apparent packing density of the particles in the nodule qualitatively agrees with the measured porosity of the nodule. EDX spectra produced for locations labeled P1 through P7 in Figure 4-76 are presented in Figures 4-77 through 4-83. Because of the nature of EDX measurements, the locations of these measurements do not guarantee that the elemental distributions shown in Figures 4-77 through 4-83 represent the single particle under the labels. The elemental composition of nearby or attached particle structures are likely to influence the overall EDX spectra. The EDX spectra indicate that the larger particles (locations P3 and P4 in Figure 4-76) in the filter cake char sample are predominately carbon (Figures 4-79 and 4-80). The one particle in Figure 4-76 that appeared spherical (location P1) exhibited a high proportion of silicon, aluminum, and calcium (Figure 4-77). Calcium and carbon were concentrated (Figures 4-82 and 4-83) in two other relatively small particles (locations P6 and P7). At locations P2 and P5, the spectra in Figures 4-78 and 4-81 indicate that the particles at these locations are high in zinc and titanium, presumably as a result of carryover of sorbent material from the absorber. None of the larger particles that were examined contained a high proportion of either zinc or titanium.

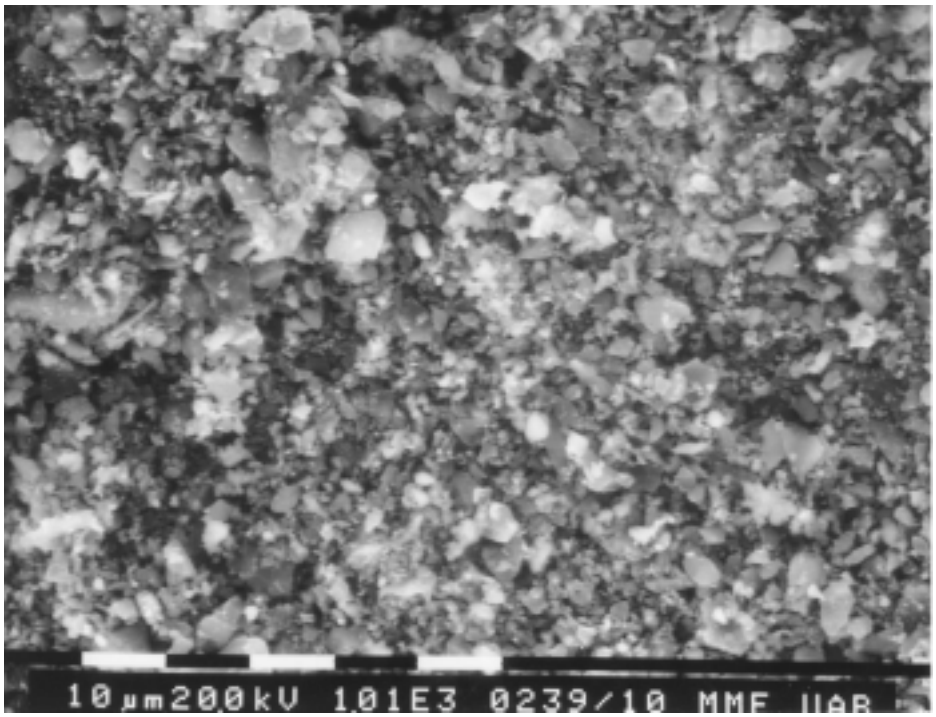

Figure 4-74. Representative scanning electron micrograph of a fresh fracture surface of a Piñon Pine gasifier char filter cake nodule (ID # 4350) collected in January 1999. The black and white bars at the bottom of the micrograph represent lengths of 10 µm.

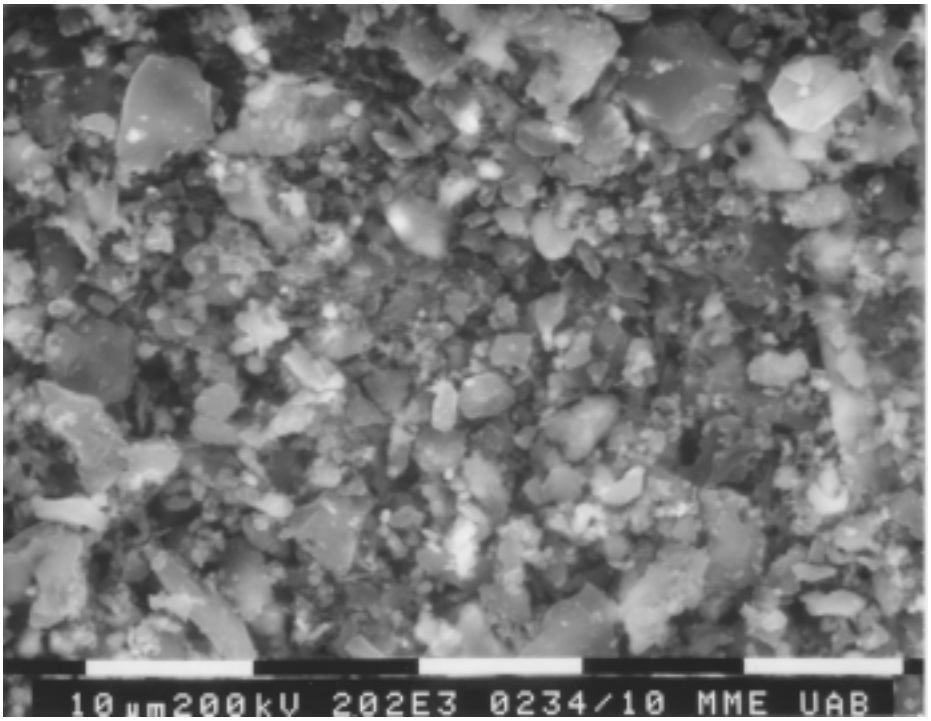

Figure 4-75. Representative scanning electron micrograph of a fresh fracture surface of a Piñon Pine gasifier char filter cake nodule (ID # 4350) collected in January 1999. The black and white bars at the bottom of the micrograph represent lengths of 10 µm.

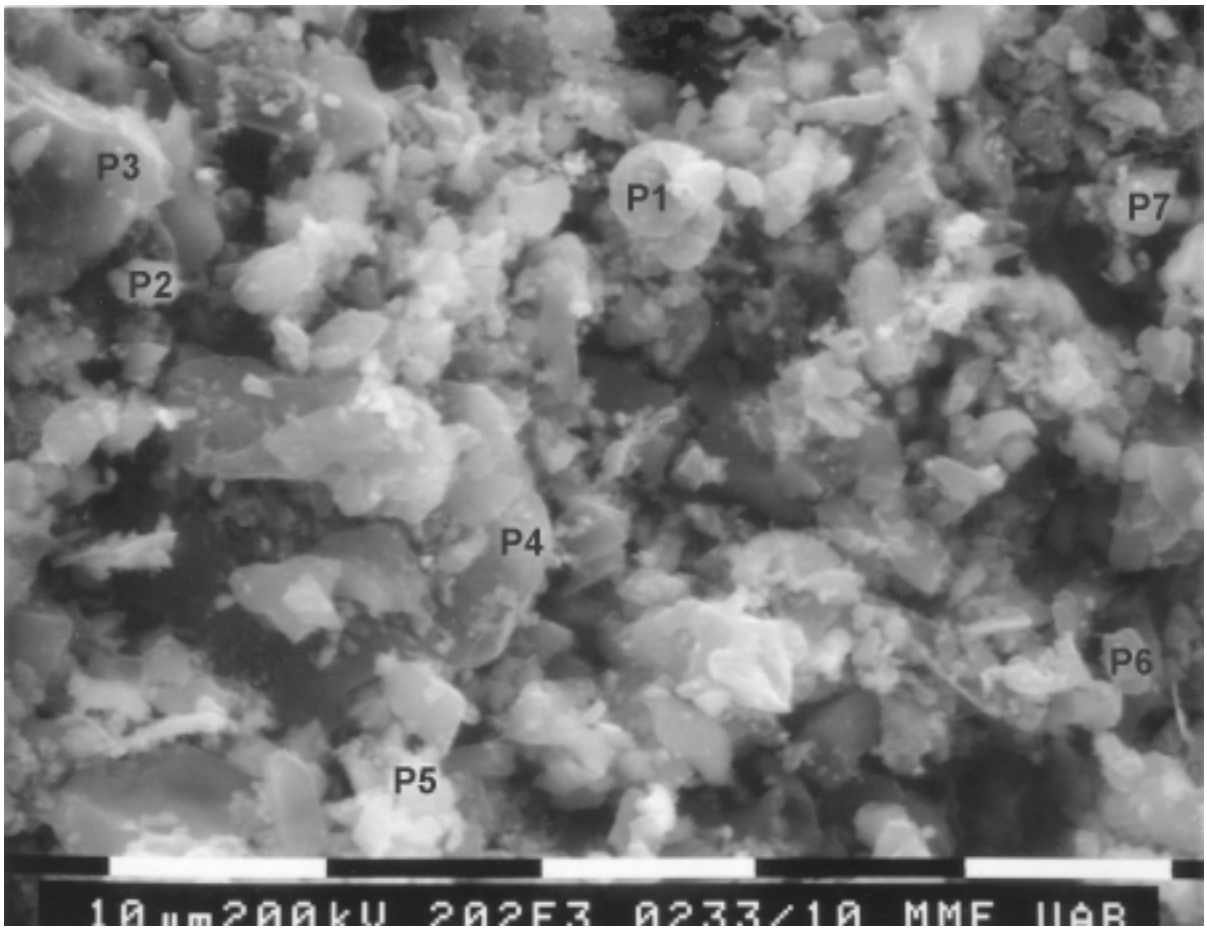

Figure 4-76. Representative scanning electron micrograph of a fresh fracture surface of a Piñon Pine gasifier char filter cake nodule (ID # 4350) collected in January 1999. The black and white bars at the bottom of the micrograph represent lengths of 10 µm. The locations where EDX spectra (Figures 4-77 through 4-83) were measured are labeled P1 through P7.

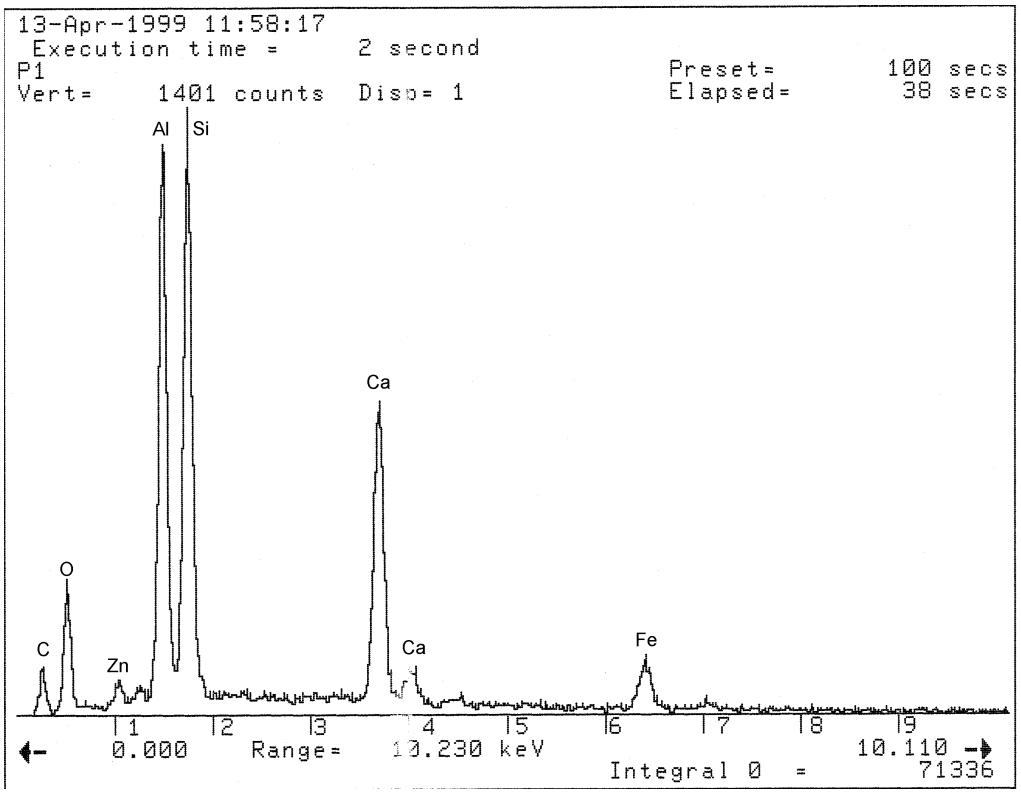

Figure 4-77. EDX spectrum taken at location P1 in the Piñon Pine filter cake nodule shown in Figure 4-76.

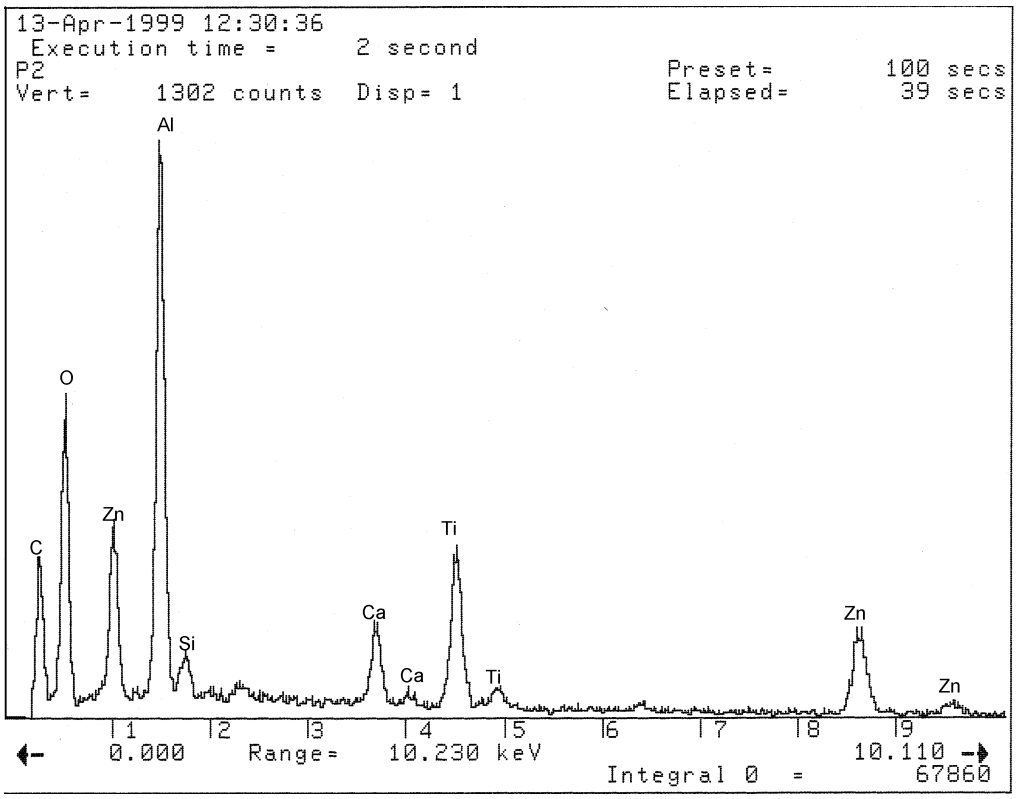

Figure 4-78. EDX spectrum taken at location P2 in the Piñon Pine filter cake nodule shown in Figure 4-76.

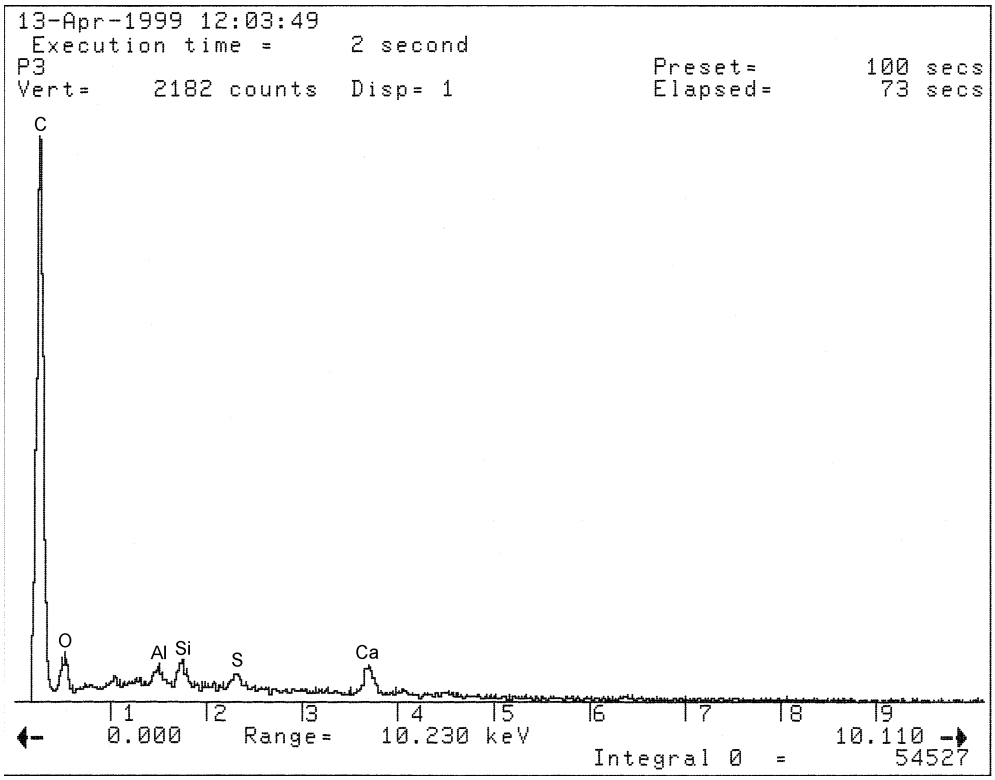

Figure 4-79. EDX spectrum taken at location P3 in the Piñon Pine filter cake nodule shown in Figure 4-76.

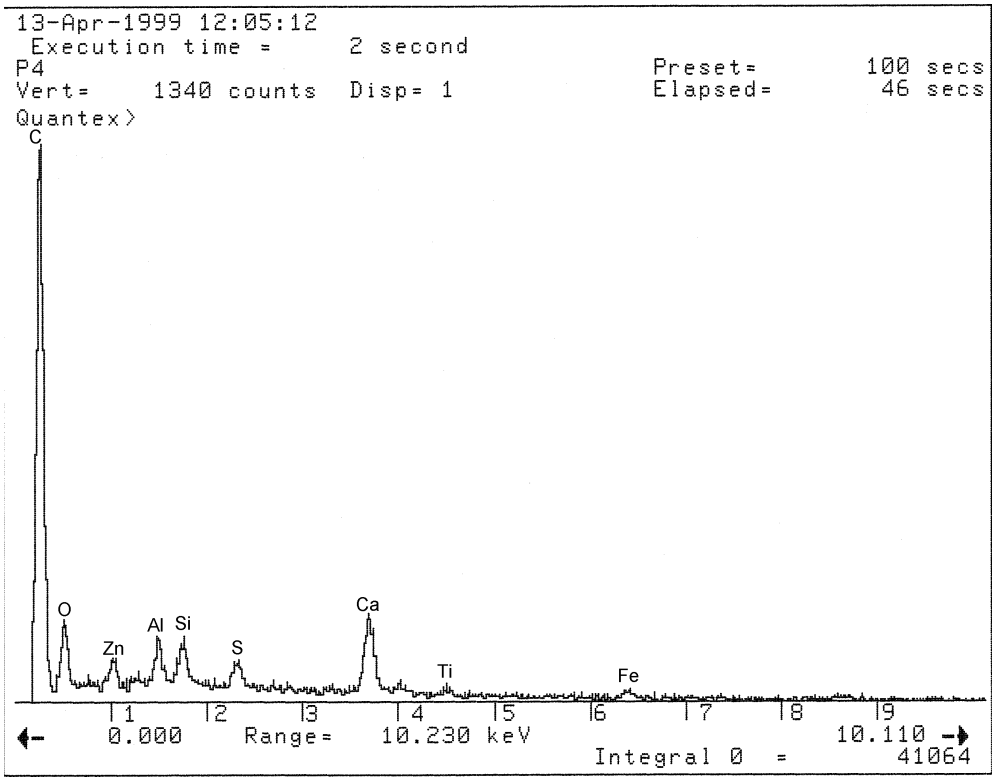

Figure 4-80. EDX spectrum taken at location P4 in the Piñon Pine filter cake nodule shown in Figure 4-76.

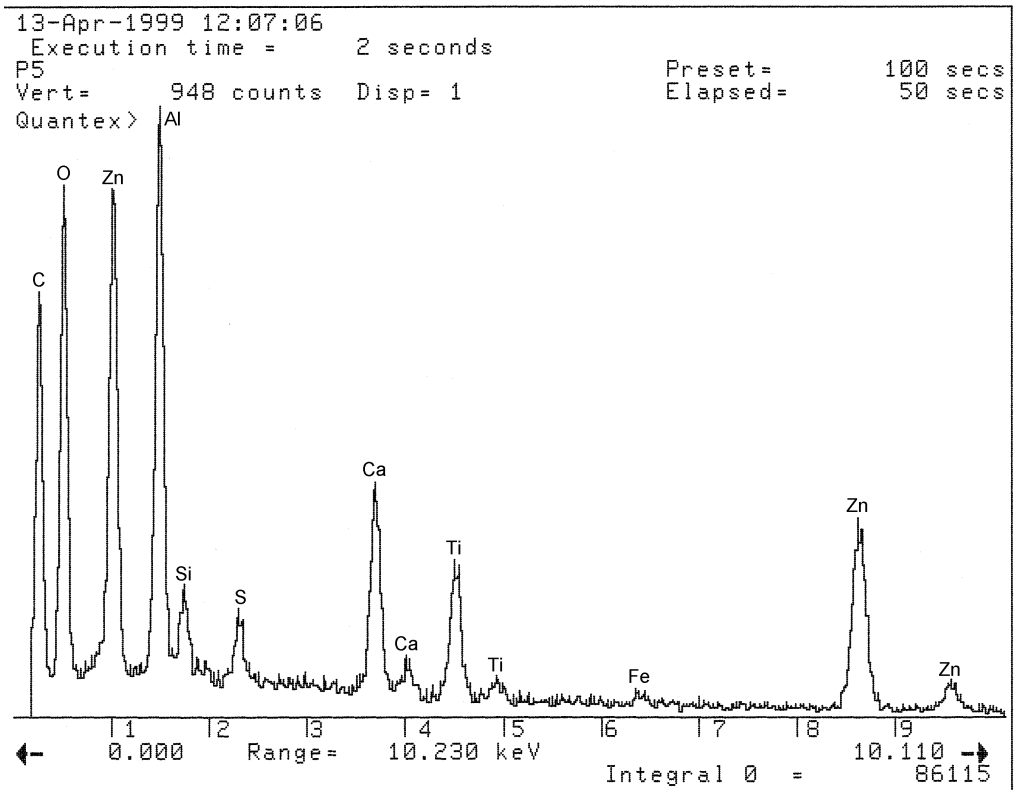

Figure 4-81. EDX spectrum taken at location P5 in the Piñon Pine filter cake nodule shown in Figure 4-76.

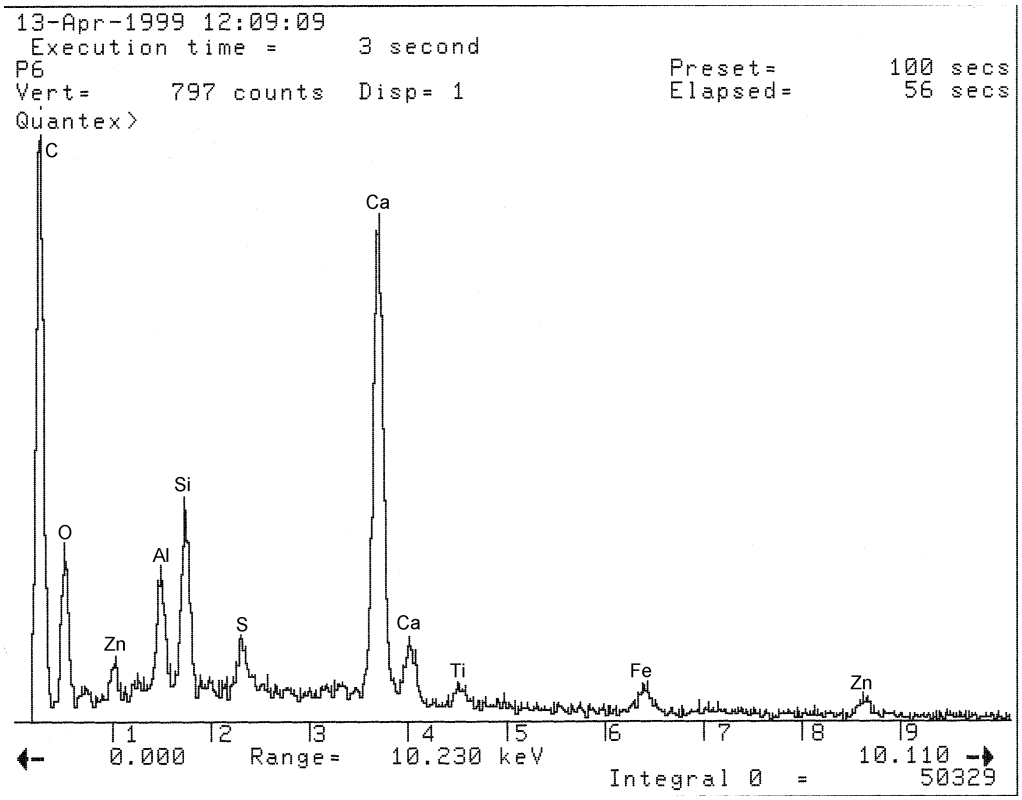

Figure 4-82. EDX spectrum taken at location P6 in the Piñon Pine filter cake nodule shown in Figure 4-76.